Metal-Organic Complexes at Surfaces

Isvoranu, Cristina

2010

Metal-Organic Complexes at Surfaces

Cristina Isvoranu

Division of Synchrotron Radiation Research
Lund University

2010

THESIS FOR DEGREE OF DOCTOR OF PHILOSOPHY

To be presented with the permission of the Faculty of Science of Lund University, for public criticism in Lecture Hall B at the Department of Physics, September 17, 2010, at 10:15

Doctoral Thesis
Division of Synchrotron Radiation Research
Department of Physics
Lund University

ISBN 978-91-7473-012-8
Printed by Media-Tryck
Lund, Sweden, August 2010

List of Papers

The present thesis is based on the following papers, which are referred to in the text by Roman numerals. Reprints were made with kind permission from the publishers.

I. **Electron spectroscopy study of the initial stages of iron phthalocyanine growth on highly oriented pyrolitic graphite**
Cristina Isvoranu, John Åhlund, Bin Wang, Evren Ataman, Nils Mårtensson, Carla Puglia, Jesper N. Andersen, Marie-Laure Bocquet, and Joachim Schnadt
Journal of Chemical Physics, 131 (2009) 214709.

II. **Tuning the spin state of iron phthalocyanine by ligand adsorption**
Cristina Isvoranu, Bin Wang, Karina Schulte, Evren Ataman, Jan Knudsen, Jesper N. Andersen, Marie-Laure Bocquet, and Joachim Schnadt
Submitted to Journal of the American Chemical Society.

III. **Ammonia adsorption on iron phthalocyanine on Au(111): Influence on adsorbate-substrate coupling and molecular spin**
Cristina Isvoranu, Bin Wang, Evren Ataman, Karina Schulte, Jan Knudsen, Jesper N. Andersen, Marie-Laure Bocquet, and Joachim Schnadt
Submitted to Physical Chemistry Chemical Physics.

IV. **Pyridine adsorption on single-layer iron phthalocyanine on Au(111)**
Cristina Isvoranu, Bin Wang, Evren Ataman, Karina Schulte, Jan Knudsen, Jesper N. Andersen, Marie-Laure Bocquet, and Joachim Schnadt
In manuscript.

V. **Comparison of the carbonyl and nitrosyl complexes formed by adsorption of CO and NO on monolayers of iron phthalocyanine on a Au(111) support**
Cristina Isvoranu, Evren Ataman, Bin Wang, Jan Knudsen, Karina Schulte, Marie-Laure Bocquet, Jesper N. Andersen, and Joachim Schnadt
In manuscript.

VI. **Adsorption of ammonia on multilayer iron phthalocyanine**
Cristina Isvoranu, Jan Knudsen, Evren Ataman, Karina Schulte, Bin Wang, Marie-Laure Bocquet, Jesper N. Andersen, and Joachim Schnadt
In manuscript.

VII. Formation of phthalocyanine-nitrosyl complexes in multilayers of iron phthalocyanine

Cristina Isvoranu, Evren Ataman, Jan Knudsen, Karina Schulte, Bin Wang, Marie-Laure Bocquet, Jesper N. Andersen, and Joachim Schnadt

In manuscript.

VIII. Surface-assisted assembly of 2D oxalate-based coordination networks: a route towards organic-based single magnetic layers

Marta Trelka, Carlos Martí-Gastaldo, Cristina Isvoranu, David Écija, Christian Urban, Evren Ataman, José María Gallego, Rodolfo Miranda, Joachim Schnadt, Roberto Otero, and Eugenio Coronado

Submitted to Journal of the American Chemical Society.

IX. Adsorption and charge transfer dynamics of bi-isonicotinic acid on Au(111)

J. Ben Taylor, Louise C. Mayor, Janine C. Swarbrick, James N. O'Shea, Cristina Isvoranu, and Joachim Schnadt

Journal of Chemical Physics, 127 (2007) 134707.

Papers not included in the thesis:

Formation of trioctylamine from octylamine on Au(111)

Sigrid Weigelt, Joachim Schnadt, Anders K. Tuxen, Federico Masini, Christian Bombis, Carsten Busse, Cristina Isvoranu, Evren Ataman, Erik Lægsgaard, Flemming Besenbacher, and Trolle R. Linderoth

Journal of the American Chemical Society, 130 (2008) 5388-5389.

Dissociation of water on oxygen-covered Rh(111)

Andrey Shavorskiy, Tuğçe Eralp, Evren Ataman, Cristina Isvoranu, Joachim Schnadt, Jesper N. Andersen, and Georg Held

Journal of Chemical Physics, 131 (2009) 214707.

Adsorption of L-cysteine on rutile TiO_2(110)

Evren Ataman, Cristina Isvoranu, Jan Knudsen, Karina Schulte, Jesper N. Andersen, and Joachim Schnadt,

Submitted to Surface Science.

Comments on my own contribution to the papers

It has to be mentioned that synchrotron radiation experiments represent most often the result of a team work and such is the case of the present work. My contribution to the papers is mostly mirrored by the position of my name in the author list. In Paper I, I took part in the experiments and I was main responsible for analysing the data and writing the manuscript. Concerning the work involved in Paper II, I was main responsible for the experimental part and the data analysis, and I participated in writing the manuscript. In Papers III, IV, V, VI, and VII, I was main responsible for performing the experiments, analysing the data and writing the manuscripts. In paper VIII, I took part in performing the spectroscopy experiments and analysing the spectroscopic data. In Paper IX, I took part in the experiments.

Contents

CHAPTER 1

Introduction

General Overview and Motivation of the Research

The research work presented in this thesis focuses on different aspects: adsorption of phthalocyanines on surfaces, adsorption of molecular ligands on phthalocyanines, formation of coordination networks based on carboxylate ligands and iron, and charge transfer characteristics of bi-isonicotinic acid on Au(111).

In general, the interest in phthalocyanines stems from the fact that they are similar to the naturally occurring porphyrins, involved in the photosynthesis in plants and oxygen transport within the red blood cells [1]. This is a reason why phthalocyanines are important model-compounds for biological systems. However, the application range of phthalocyanines is much broader than that. Apart from the conventional use as dyes and pigments [1,2], phthalocyanines have attracted interest in connection with applications for catalysis [3-7] and fuel cells [8-16], sensors [17-34], dye sensitized solar cells [35-38], organic light emitting devices [39-42], organic thin-film transistors [43,38], and photodynamic cancer therapy [44,45], among others. In particular, the metallorganic macrocycles iron phthalocyanines are attractive compounds, because of the magnetic properties of the iron atom. For the present work, iron phthalocyanines are extremely interesting molecules because as will be shown, their spin state can be significantly changed by adsorption of molecular ligands.

Paper I and part of Paper II present a detailed description of the adsorption of iron phthalocyanine on highly oriented pyrolitic graphite and Au(111) surfaces, which is first of all important as an initial step to studying the adsorption of gases. Also, it is particularly interesting to compare the adsorption on these two substrates, because the adsorbate-substrate coupling is different in the two cases, the coupling is weak on graphite whereas it has covalent character on Au(111).

Papers II-VII are concerned with the adsorption of electron donor species ammonia and pyridine and electron acceptor species carbon monoxide and nitric oxide on iron phthalocyanine and their influence on the spin state of the molecular network. The valence electronic structure of the *d* levels of iron phthalocyanine consists of states lying close in energy. Their energetic distribution and in consequence the spin state of the molecule can be

affected by adsorption of ligands. More than that, different ligands can have different impact on the spin state, which paves a way towards a controlled manipulation of the spin state by ligand attachment. Controlling the properties of devices is crucial when considering any applications. Such findings can have potential impact on the emerging field of molecular spintronics. The binding of small gas molecules to the metal centre of the phthalocyanine can also be exploited for possible applications in gas sensing devices, catalysis, and from a fundamental point of view. Adsorption of gases on iron phthalocyanine constitutes the key part of the research work in this thesis.

The oxalic acid study (Paper VIII) is part of the young field of coordination chemistry at solid surfaces. Its importance stems from the fact that it shows the formation of 2D coordination networks containing organic ligands connected through iron metallic centres, with the shortest metal-metal distance reported so far for a 2D coordination network at surfaces. The study has potential impact for fundamental understanding of organic magnetic materials and for engineering of new magnetic plastics.

The bi-isonicotinic acid study (Paper IX) is related to the so-called dye-sensitised solar cells (DSSCs). The study deals with the adsorption and charge transfer dynamics of bi-isonicotinic acid on Au(111). The ultra-fast charge transfer from the dye molecules to the substrate represents a central aspect related to the DSSC. Understanding the charge transfer process is crucial in selecting the optimal substrate-dye combination. The interest in bi-isonicotinic acid is due to the fact that it is a major component of the to-date most efficient dye used in the DSSCs, the so-called N_3 molecule ($[(dcb)_2Ru(NCS)_2]$) [46,47]; more precisely it is the ligand through which the dye binds to the surface. It is sometimes difficult to characterise the charge transfer dynamics of dye molecules by spectroscopic techniques in ultrahigh vacuum, due to the complexity of the molecules and because they can be rather difficult to sublimate. However, studies of the individual ligands are also of central interest. The motivation for investigating the bi-isonicotinic acid on gold comes from the study of McFarland and Tang [48] which deals with a cell consisting of $Ti/TiO_2/Au$/dye. In relation to the above-mentioned study and because the bi-isonicotinic acid/TiO_2 system has been studied quite intensively [49-58], investigating the Au(111)/bi-isonicotinic acid interface is a logical continuation towards gaining a more complex understanding of such devices.

For characterisation, surface sensitive techniques x-ray photoelectron spectroscopy (XPS), x-ray absorption spectroscopy (XAS), resonant photoemission spectroscopy (RPES), and scanning tunneling microscopy (STM) are used. Combining the information available from these techniques makes it possible to obtain unique atomic scale information regarding the electronic and geometric structure of the systems in study, their chemical composition, the molecule-substrate and intermolecular interactions, the ultrafast charge transfer dynamics at the adsorbate-substrate interface, and what constitutes a key aspect of the research work here presented, valuable information on the spin state of the systems.

The summary part of the thesis is composed of five chapters. The first chapter is the present introduction, followed by Chapter 2 describing the spectroscopic methods and the experimental equipment and Chapter 3 presenting the scanning tunnelling microscopy technique. Chapter 4 focuses on description of the substrates, adsorbates, and of the intermolecular interactions involved in the studied systems. The last chapter, Chapter 5 gives a short overview of some relevant experimental results.

CHAPTER 2

Spectroscopy Methods

2.1. X-ray Photoemission Spectroscopy

2.1.1. Principle

Photoemission spectroscopy is a technique that provides information about the occupied electronic states of molecules or solids. It is based on the photoelectric effect, first discovered by Heinrich Hertz in 1887 [59] and later explained theoretically by Albert Einstein [60], which "for his services to Theoretical Physics, and especially for his discovery of the law of the photoelectric effect" [61] was awarded the Nobel Prize in 1921. A schematic view of the photoemission process is shown in Figure 2.1.

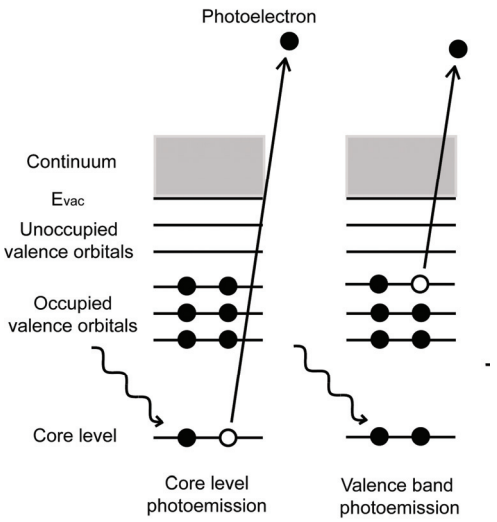

Figure 2.1. Schematic picture of the photoemission process. In core level photoemission, a core electron is promoted into the vacuum if the sample is irradiated by photons of sufficient energy. In a similar manner, valence band photoemission promotes an electron from the valence levels into the vacuum.

Absorption of photons of well-defined energy $h\nu$ by an atom, molecule or solid induces the emission of electrons (called photoelectrons), whose kinetic energy (KE) can be measured by an electron energy analyzer (also called electron spectrometer). The binding energy (BE) can be further determined based on energy conservation rules: $BE = h\nu - KE - \phi$, where ϕ represents the work function of the sample. The technique was developed by Prof. Kai Siegbahn from Uppsala and his collaborators. In 1981 Siegbahn was awarded the Nobel Prize for his contribution to the development of electron spectroscopy [61].

An x-ray photoelectron spectrum displays the number of collected electrons as a function of binding energy (Figure 2.2). The electron binding energies are element-specific and also specific for each particular level inside an atom, and more than that, they can be used to distinguish between different chemically inequivalent states of the same atom. Despite the localised nature of the core levels and of the fact that core electrons do not participate in chemical bonds, any change in the electron distribution of the valence levels in either the initial[1] or final[2] state will affect the core level binding energies giving so-called chemical shifts[3] in the photoemission spectra.

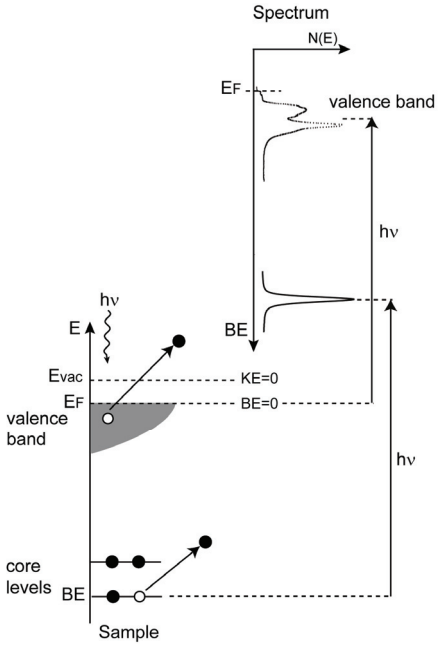

Figure 2.2. Relation between the energetic levels in a metallic sample and the photoemission spectrum. Absorption of monochromatic photons by the sample leads to core and valence electrons excitation into the vacuum, with the binding energy $BE = h\nu - KE - \phi$. The photoemission spectrum displays the number of collected electrons as a function of binding energy of the photoelectrons. Core levels give narrow peaks because of their localised nature, while the valence band region shows up as broad features due to the delocalised nature of the valence electrons.

[1] Initial state effects are related to the ground state of the system.
[2] Final state effects appear in the core excited state of a particular system.
[3] The binding energy is strongly dependent on the chemical state of the atom from which the photoemission takes place (oxidation state, electron density). Any change in the chemical environment in either the initial or final state results in a binding energy shift in the photoemission spectrum, called chemical shift. Typical values for the chemical shifts range from 0.1 eV to a couple of eV.

2.1.2. Binding Energy Definition

In a total energy picture, the initial state of a system containing N electrons is characterised by the total energy of the ground state $E_i(N)$, and the final state is characterised by the total energy of the sample after the ejection of the photoelectron $E_f(N-1)$ and the photoelectron with kinetic energy KE. According to energy conservation [62], the following holds:

$$E_i(N) + h\nu = E_f(N-1) + KE. \qquad \text{(eq. 2.1)}$$

From the equation above, the quantity $E_f(N-1) - E_i(N)$ can be identified as the ionisation potential (*IP*) of the system:

$$IP = h\nu - KE = E_f(N-1) - E_i(N). \qquad \text{(eq. 2.2)}$$

The ionisation potential is referred to the vacuum level. For the particular case of a metallic sample, it is more convenient to use the Fermi level as energy reference point instead of the vacuum level, because the Fermi levels of the sample and spectrometer are aligned during the measurement when the sample and spectrometer and in electrical contact, which is not the case for the vacuum levels (Figure 2.3). In measurements with respect to the Fermi level the quantity determined is the binding energy. Equation 2.2 then becomes:

$$BE = h\nu - KE - \phi = E_f(N-1) - E_i(N). \qquad \text{(eq. 2.3)}$$

In the equation above, ϕ represents the value of the sample work function (ϕ_{sample}). In reality, the experimentally measured kinetic energy is the kinetic energy relative to the vacuum level of the analyzer (Figure 2.3) and in this case ϕ represents the spectrometer work function ($\phi_{\text{spectrometer}}$) and the kinetic energy as measured by the spectrometer is (KE') is different from the photoelectron kinetic energy by the amount of $\phi_{\text{spectrometer}}$-$\phi_{\text{sample}}$. Because of this, a calibration procedure is always necessary in order to determine the correct binding energy of the sample levels. For the measurements presented in this thesis the calibration was always done by measuring the Femi level of the sample. This procedure eliminates the differences in kinetic energy caused by work function difference between the sample and analyzer, because the energy will be measured with respect to the Fermi level.

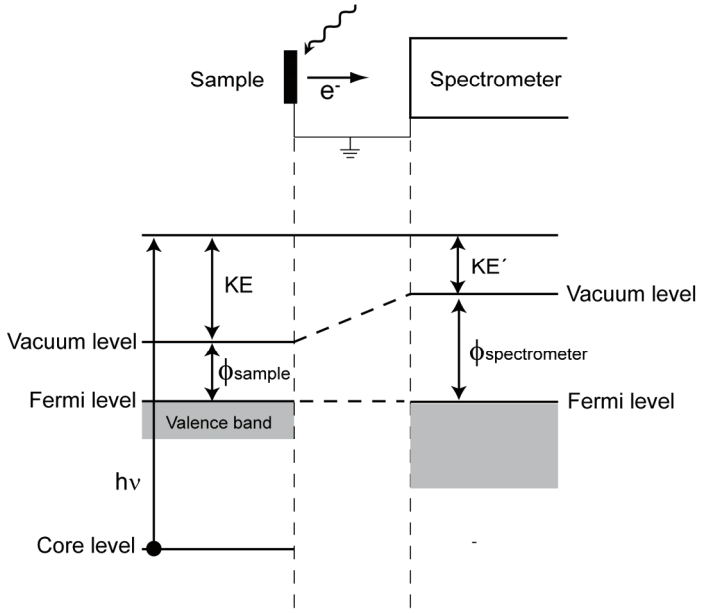

Figure 2.3. Energy levels alignment for a metallic sample/spectrometer system. The energy levels of relevance for the binding energy measurement are illustrated. The sample and spectrometer are in electrical contact and grounded, thus the Fermi levels are aligned. The kinetic energy KE´ as measured by the spectrometer is different from the kinetic energy KE relative to the vacuum level of the sample. ϕ_{sample} and $\phi_{\text{spectrometer}}$ represent the work functions of the sample and spectrometer, respectively [63].

2.1.3. Photoionisation Cross Section

The transition probability per unit time between an initial state $\Psi_i(N)$ of a system containing N electrons and a final state $\Psi_f(N)$ can be calculated based on Fermi's golden rule and also making use of the electric dipole approximation [62,64]. The electric dipole approximation is useful in estimating the interaction Hamiltonian which describes the coupling between the electron and the incoming electromagnetic radiation. Within the dipole approximation, which assumes that the wavelength of the exciting electromagnetic radiation is much larger than the atomic dimensions, the interaction Hamiltonian is given by the dipole operator D. The transition probability from the initial state to the final state can then be written as:

$$T_{i\to f}^{PES} \propto \frac{2\pi}{\hbar}\left|\left\langle \Psi_f(N)\middle|D\middle|\Psi_i(N)\right\rangle\right|^2 \delta\left(E_f(N-1)+KE-E_i(N)-h\nu\right). \quad \text{(eq. 2.4)}$$

In eq. 2.4, as mentioned, $\Psi_f(N)$ and $\Psi_i(N)$ represent the final and initial state wave functions of the system containing N electrons and D is the dipole operator. The final state wave function $\Psi_f(N)$ is composed of the wave function of the ionic system after photoemission $\Psi_f(N-1)$ and the excited electron $\varphi_{f,KE}$ characterised by the wave-vector k and kinetic energy KE ($\Psi_f(N)=C\varphi_{f,KE}\Psi_f(N-1)$, where C represents the

antisymmetrisation operator). The δ function ensures the energy conservation, meaning that the photon energy needs to be equal to the difference between the final state ($E_f(N-1)+KE$) and initial state energy $E_i(N)$ for the excitation to take place. Total or partial cross-sections may be considered. In experimental photoemission spectroscopy, partial cross-sections are needed, which refer to the transition probability from a particular atomic level of interest, while the total cross-sections represent the sum over all possible transitions at a given photon energy.

2.1.4. Approximations in Photoemission Spectroscopy

The binding energy definition, as discussed in Chapter 2.1.2 is very exact, but the total energies are not easy to calculate, so one needs approximations in order to calculate and estimate the binding energy values.

Koopmans' theorem and the frozen orbital approximation [62,65] together provide a first approximation for calculating the binding energy, without taking any final state effects into account. In this approximation, the orbitals are considered to be unaffected by the photoionisation process. The wave function of the remaining *N-1* electrons after photoemission is regarded as being the same as the initial state wave function minus the one-electron orbital of the excited electron ($\Psi_f(N-1)_{frozen} = \Psi_i(N-1)$). A first step towards estimating the binding energy according to Koopmans' theorem is expressing the transition matrix element $\langle \Psi_f(N)|D|\Psi_i(N)\rangle$ in terms of one-electron wave functions. In this case,

$$\Psi_i(N) = C\varphi_{i,k}(1)\Psi_i(N-1). \qquad \text{(eq. 2.5)}$$

$$\Psi_f(N) = C\varphi_{f,KE}\Psi_f(N-1). \qquad \text{(eq. 2.6)}$$

$$\left|\langle \Psi_f(N)|D|\Psi_i(N)\rangle = \langle \varphi_{f,KE}|D|\varphi_{i,k}\rangle\langle \Psi_f(N-1)|\Psi_i(N-1)\rangle\right. . \qquad \text{(eq. 2.7)}$$

In the equations above, C is the antisymmetrisation operator as already mentioned, $\varphi_{i,k}(1)$ is the one electron wave function of the orbital from which the emission takes place, and $\varphi_{f,KE}$ is the wave function of the photoemitted electron. In the frozen orbital approximation, the overlap integral becomes unity and the transition matrix element depends on one-electron wave functions only. The binding energy according to Koopmans' approximation [62], also called Koopmans' binding energy is then obtained from the Hartree-Fock energies and is equal to the one-electron ground state energy of the orbital (*k*) from which the photoelectron was emitted (eq. 2.8). In accordance with Koopmans' theorem the photoemission spectra would always consist of single lines (Figure 2.4).

$$BE(k) = \varepsilon_k . \qquad \text{(eq. 2.8)}$$

In reality the orbitals are not frozen. Once the photoelectron is removed, the system reacts to the new core hole potential in order to minimise the total energy, and **final state**

effects must also be taken into account for a more accurate estimation of the binding energy. For this purpose it is important to consider additional final state contributions, such as relaxation and correlation effects (eq. 2.9).

$$BE(k) = \varepsilon_k + E_{relaxation} + E_{correlation}\,. \qquad \text{(eq. 2.9)}$$

Relaxation [65,66] includes atomic orbitals contraction around the core hole site and charge transfer or polarisation screening. In adsorbate/substrate systems, such as the systems presented in this thesis, charge transfer screening involves a reorganization of the valence electrons as a result of the core hole creation, causing electron flow of valence electrons from the substrate to the molecular site where the core hole is localised. If the adsorbate/substrate coupling is weak or if the substrate is semiconducting, the time required for the charge transfer screening is expected to be too long to have any relevance, so relaxation process occurs by polarization screening (image charge screening), which implies charge redistribution in the substrate such that an opposite charge is build in the substrate surface. Correlation effects refer to electron-electron interactions in the system, which go beyond a mean field description theory such as Hartee Fock. In most cases, the correlation effects are neglected, but they might become significant in some cases.

Going back to the relaxation process, this depends on the kinetic energy of the photoelectrons. When x-rays are used for excitation, the photoemission process takes places instantaneous (x-ray excitations normally occur in attoseconds) and the valence electrons do not have the time to react to the new core hole potential. Only processes that happen in the same time-scale as the photoemission will be observed. This leaves the place for the **Sudden approximation.** which allows multiple excited final states [62,65,67] having the same core hole. Within the Sudden approximation, the wave function of the remaining N-1 electrons after photoemission $\Psi_f(N-1)$ is not anymore an eigenstate of the Hamiltonian, but can rather be described as a combination of eigenstates, with corresponding eigenvalues and the transition matrix element in consequence includes a sum over overlap integrals for all possible final states (eq. 2.10). Each non vanishing overlap will give a contribution to the spectrum.

$$\left\langle \Psi_f(N)\middle|D\middle|\Psi(N)_i\right\rangle = \left\langle \varphi_{f,KE}\middle|D\middle|\varphi_{i,k}\right\rangle \sum_s \left\langle \Psi_{f,s}(N-1)\middle|\Psi_i(N-1)\right\rangle \qquad \text{(eq. 2.10)}$$

Sudden approximation explains the existence of the shake-up features in the photoemission spectra. The shake-up satellites are excitations from occupied to unoccupied valence levels resulting in kinetic energy losses. According to eq. 2.10, the photoemission spectrum consists of several lines (Figure 2.4), a main line corresponding to the fully screened core hole (most relaxed state) and higher binding energy satellite lines, the intensity of each line being determined by the overlap integral between the initial and final state wave functions.

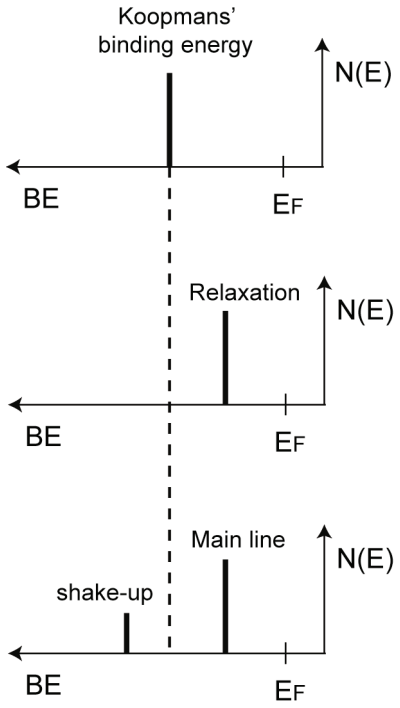

Figure 2.4. Schematic picture of the photoemission spectra as resulted from the approximations discussed above. Upper panel represents the position of the photoemission line in the frozen orbital approximation, the middle panel introduces the relaxation effects on the binding energy, and the bottom panel illustrates the Sudden approximation and shows a spectrum composed of a low binding energy main line (corresponding to the most relaxed state) and one high binding energy shake-up satellite. The Koopmans' binding energy is always at the centre of gravity of all lines in the photoemission spectrum.

2.1.5. Line Shapes and Additional Features in Photoemission Spectra

In the ideal case the photoemission spectra would consist of sharp peaks, broadened only as a result of their limited lifetime, but this is not the case in reality. There are several sources of broadening that can affect the line shape of the main photoemission peaks and, as seen in section 2.1.4, additional features associated to the main photoemission line can also be present as a result of multiple excited final states. The two omnipresent factors contributing to the photoemission line shapes are the instrumental limitations and the core hole lifetime. In some situations, satellites, vibrations, but also multiplet splitting, spin-orbit coupling, and chemical effects may play an important role. The multiplet splitting and spin-orbit coupling effects will be later dealt with in section 2.1.6.

Instrumental limitations, such as the energy width of the x-ray source (monochromator resolution) and the analyzer resolution have essential contributions to the photoemission line width. The instrumental broadening is characterised by a Gaussian distribution [68]. Typical values for monochromator energy resolution in the soft x-ray regime are in the 10-1000 meV range [69] and the values used for the recording of the photoemission and x-ray absorption spectra presented in this thesis vary in between 50-200 meV. Typical values that were used for the analyzer resolution are in the range 40-400 meV for the XPS experiments.

The other source of broadening is the natural line width which is due to the finite lifetime of the core-excited system. The natural line width is given by a Lorentzian distribution [70]. According to Heisenberg's uncertainty principle (eq. 2.11), since the core

hole lifetime is very short (10^{-14}-10^{-17} sec) [71], there will always be a degree of broadening in the energetic levels. In the case of low-Z atoms, the lifetime contribution is usually small (within of tenths of eV) [72] compared to other sources of broadening. For example in the case of N 1*s*, C 1*s* and O 1*s* core levels the lifetime widths are close to 0.1 eV [71].

$$\Delta E \times \Delta t \geq \hbar \qquad \text{(eq. 2.11)}$$

The main photoemission line is normally approximated as a convolution between instrumental (Gaussian) and lifetime (Lorentzian) factors, which gives a symmetric, so-called Voigt distribution profile. When needed, an asymmetry can also be added. This is the case for metallic samples, where the main line contains an asymmetric tail on the high binding energy side [62] (see discussion below).

The core level line shape carries valuable information about the way the valence electrons react to the core hole creation. The main photoemission peak (lowest binding energy peak) correspond to the most efficiently screened core-hole [65] According to the Sudden approximation, multiple excited states are also allowed. As a response to the sudden creation of the core hole, quantized excitations from occupied to unoccupied valence levels can occur and such excitations appear in the spectrum on the high binding energy side of the main line as shake-up peaks (normally 1-10 eV shifted with respect to the main photoemission line [65,72]). In a similar picture with the shake-up excitations, shake-off satellites may be described, with the difference that in the case of shake-off peaks the valence electron is emitted into the vacuum, creating wider peaks and higher in binding energy with respect to the shake-ups [62]. In the case of metallic samples, the high binding energy asymmetric tail characteristic for the main peaks is due to the fact that there is no energy gap between the valence and conduction band, so that unfilled electron levels are found at the Fermi level and only infinitesimal amounts of energy [68,73] are needed to produce excitations just above the Fermi level. In the case of shake-up satellites the excitation takes place between energy bands, while the asymmetry is due to excitations within the same band. Additional satellite structures may appear in the spectra due to plasma oscillations, when the photoelectron creates collective quantized excitations of the free electron gas at the Fermi level, so called plasmons [74]. Plasmon excitations are normally 10-30 eV shifted with respect to the main line [75]. Up to now, only the way the electrons react to the core hole creation was considered. If one also takes nuclei into account, the core hole creation in a solid sample can also induce lattice vibrations, called phonons [65,72]. This can induce further Gaussian broadening. During the photoionisation process, molecular vibration modes may also be excited, resulting in an asymmetry or additional peaks [66,72] with respect to the main line. Phonon and vibrational excitations normally require 10-500 meV.

The photoemission spectra always contain an inelastic background, created by protoelectrons originating from larger depths in the crystal than the elastic peaks and that have suffered inelastic energy losses (see also discussion in Section 2.1.6) [62].

2.1.6. Some Useful Concepts in Photoemission Spectroscopy

Attenuation Length and Surface Sensitivity

XPS is a surface sensitive technique. Even if x-rays can penetrate deep into the solids (μm range), the photoelectrons detected in the photoemission experiments originate from the topmost atomic layers only, because the electrons interact much more strongly with matter. The photoemitted electrons suffer elastic and inelastic energy losses, but only those electrons that reach the analyzer without loosing energy (elastically scattered electrons) will be detected in the main photoemission peak. An electron travelling through a solid has a characteristic "mean free path" [75], which is a measure of the distance it can travel through the solid before suffering inelastic energy losses. Actually the term "attenuation length" is more appropriate, because it also includes the effects of elastic scattering processes, meaning that even if the electrons do not loose energy by being elastically scattered - the average distance they travel will decrease as a result of the elastic scattering processes, leading thus to increased probability of suffering inelastic losses. The mean free path of an electron through a solid is strongly dependent on the electron kinetic energy. The so-called "universal curve" (Figure 2.5) gives the mean free path as a function of the electron's kinetic energy [76,77]. It shows that there is an energy range where the surface sensitivity is maximum, which corresponds to the minimum of the universal curve (approximately 50-100 eV). In this energy range the depth probed is less than 10 Å, meaning that the vast majority of the signal originates from the very first 2-3 atomic layers inside the sample. For electron energies below or above this range, the depths probed are larger.

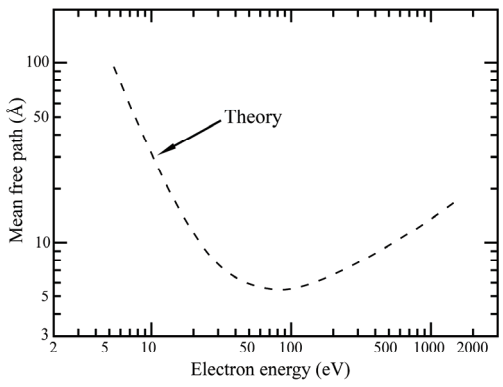

Figure 2.5. Universal curve (theoretical) representing the electron mean free path as a function of the electron's kinetic energy. The curve has a minimum in the region of around 50-100 eV (redrawn from Ref. [77]).

Apart from the electron kinetic energy, there is one more aspect to consider when trying to increase the surface sensitivity of a particular experiment, namely the emission angle (Figure 2.6). The more grazing the geometry, the more enhanced the surface sensitivity.

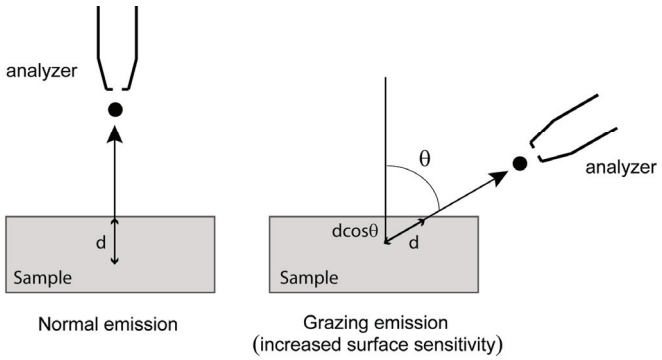

Figure 2.6. Illustration of increasing the surface sensitivity in a photoemission experiment by going from normal emission to grazing emission angles (angle θ between the surface normal and the analyzer). The mean free path (d) is the same in the two cases (assuming that no other parameter than the emission angle is changed), so the effective sample depth probed in grazing emission is smaller (dcosθ), meaning increased surface sensitivity

Spin-Orbit Coupling

Spin-orbit coupling, also called spin-orbit interaction is an interaction between the electron spin and its motion (angular momentum) [78,79]. This effect appears in the photoemission spectra as a splitting of the photoemission lines for a particular level (Figure 2.7). Once a core electron is photoemitted from an orbital with non zero angular momentum containing two paired electrons, the remaining electron can be in either spin-up or spin-down state. It is the magnetic interaction between the two possible spin states and the angular momentum of the electron that gives two different electronic states with different energy characterised by the total angular momentum quantum number j ($j=l+s$, where l is the angular momentum quantum number and s is the electron spin). For example, the final state in the photoemission from the Au 4*f* level is characterised by $j=7/2$ and $j=5/2$, which gives the two photoemission lines shown in Figure 2.1.7. The closer the atomic shell to the nucleus, the stronger the spin-orbit coupling, so the larger the energy splitting of the photoemission lines. The energy splitting for the Au 4*f* levels is ~4 eV and for Fe 2*p* is ~13 eV [80]. Each spin orbit component contains contributions from different degenerate levels characterised by quantum numbers m_j. The intensity ratio between the spin-orbit peaks is given by the degeneracy of each state, $(2j+1)$.

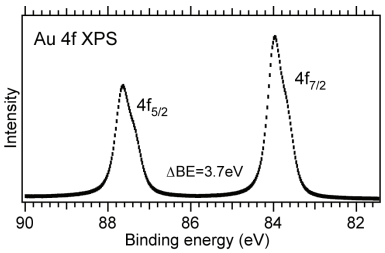

Figure 2.7. An example of spin-orbit splitting of the photoemission signal of the Au 4*f* level from a bare Au(111) crystal. The experimentally measured spin-orbit splitting in this case is 3.7 eV.

Multiplet Splitting

The m_j sublevels characteristic for each spin-orbit component discussed above may, in some cases, become non degenerate as a consequence of coupling between the core hole and the spin of partly filled valence levels, giving rise to unusual broad photoemission lines (Figure 2.8). The m_j sublevels split in energy under the influence of the effective spin field of the valence electrons [85,86]. The higher the spin in the valence band, the larger the energy splitting between the different m_j levels and the broader the overall photoemission lineshape. Such final state effects, common for the 3*d* transition metal series are called multiplet splitting [81-84]. Actually, the multiplet splitting affects the *s* levels also, which do not show spin-orbit coupling.

Two theoretical models are most frequently used for describing the multiplet splitting, the so-called *jj* and *jK* coupling schemes [87,88]. In the *jj* coupling scheme, the spin (s_c) and the orbital angular momentum (l_c) of the core hole couple to give the total angular momentum of the core hole j_c, which then couples to the total angular momentum of the valence electrons J_v and gives the total angular momentum J_f. The *jj* model normally holds when the spin-orbit interaction in the valence band is stronger than the Coulomb interaction between the core hole and the valence electrons. In the *jK* coupling model, the j_c total angular momentum of the core hole couples with the orbital angular momentum of the valence electrons L_v resulting in the total angular momentum K, which then couples to the total spin S_v of the valence electrons to give the total angular momentum J_f. The *jK* coupling scheme holds when the spin-orbit interactions in the valence band are weaker than the Coulomb interaction between the core hole and the valence electrons.

The multiplet splitting is several times exemplified in this thesis by the Fe $2p_{3/2}$ photoemission line (Papers II-VI). For the particular case of the Fe $2p_{3/2}$ photoemission line of FePc (Figure 2.8) the multiplet splitting arises as a consequence of coupling the 2*p* core hole with the spin of the two unpaired valence 3*d* electrons (total valence spin S=1).

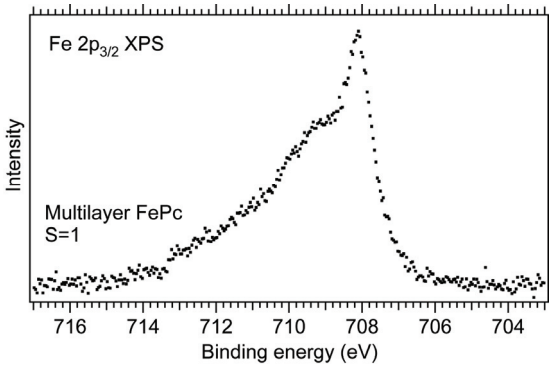

Figure 2.8. The Fe $2p_{3/2}$ photoemission line for an FePc multilayer on a Au(111) support. The line shows a broad, multiplet structure, due to the splitting of the m_j levels characteristic for the j=3/2 spin-orbit component in the effective spin field of the valence electrons.

Ligand Field Splitting

Ligand field splitting is not necessarily a subject related to the photoemission process, but it becomes of great importance in the context of the research work presented here. The ligand field splitting refers to the fact that in transition metal complexes the metal *d* orbitals are not degenerate anymore, but become split in energy [79,89,90]. The splitting is caused by the specific bonding interaction between the metal *d* orbitals and the ligand orbitals. The molecular orbital theory is useful for describing the effect. Figure 2.1.9(a) is an example of molecular orbital diagram for an octahedral complex. For the formation of the complex, valence *d* orbitals from the metal combine with the ligand orbitals. The metal *d* orbitals involved in the bonding with the ligands, together with the ligand orbitals give bonding and antibonding combinations. The antibonding combination is formed by the metal *d* contribution. The rest of the metal *d* orbitals, the ones that do not participate in the bonding have non bonding character [79,89]. More precisely, the *d* orbitals pointing along the *x*, *y* and *z* axes (dz^2 and dx^2-y^2) will give stronger overlap with the ligands, meaning that their antibonding part will be the highest in energy with respect to the *dxy*, *dyz* and *dxz* orbitals that remain non bonding (due to symmetry considerations). This is actually what gives the dominant contribution to ligand field splitting. The separation between the lower and higher energy *d* states is called ligand field splitting parameter or Δ parameter. The size of the Δ parameter determines how the electron distribution inside the *d* levels will take place (Figure 2.9(b)). More precisely if Δ is high enough, electrons will first fill the low lying *d* states before any population of the higher *d* states takes place.

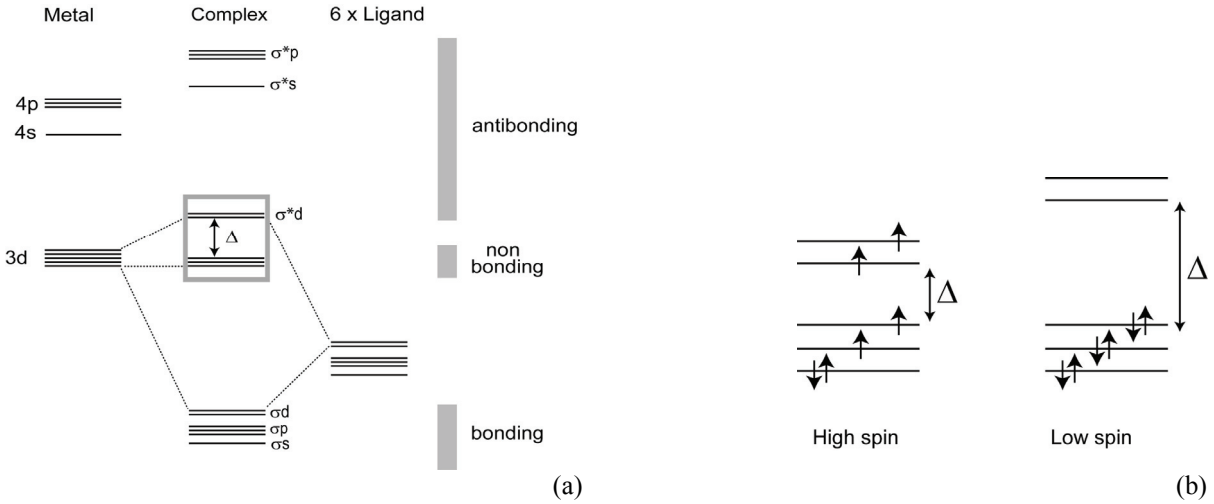

Figure 2.9. (a) Schematics of the molecular orbital diagram for an octahedral ML_6 complex. The orbitals marked with the box have mainly metal *d* character (the non-bonding orbitals are the *dxy*, *dyz* and *dxz* orbitals and the antibonding orbitals are the dz^2 and dx^2-y^2 orbitals); (b) an example of how the ligand field splitting parameter Δ affects the electronic distribution inside the d^6 level of the metal. Small Δ values (weak field ligands) result in a high spin configuration, while large Δ values (strong field ligands) lead to a low spin configuration.

The electron distribution inside the *d* levels can significantly affect the spin state of the system. In the following, an illustrative example from Paper VI on how the coordination of NH_3 to the Fe sites of the FePc multilayer molecules can affect the energetic distribution of the iron 3*d* levels (and in consequence the electron distribution inside the *d* levels) is shown (Figure 2.10). The bottom spectrum characteristic for an FePc multilayer shows a broad structure due to the two unpaired spins in the FePc 3*d* band (S=1). When NH_3 comes into play, the interaction between its lone pair orbital and the dz^2 state on the Fe increases the splitting between the dz^2 and *dxy*, *dyz*, *dxz* levels compared to FePc, resulting in a low spin FePc(NH_3) complex (S=0).

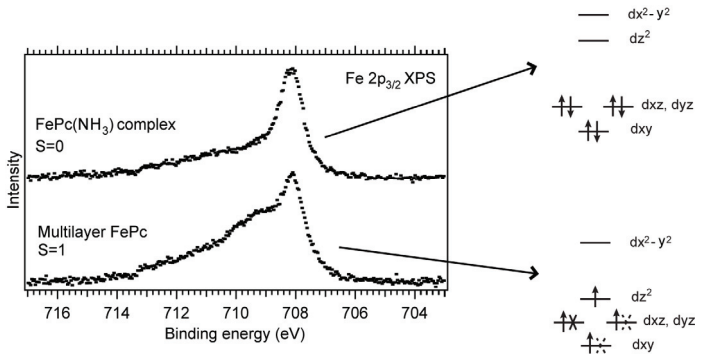

Figure 2.10. An example of how the electron distribution of the iron *d* states can influence the splitting of the m_j components in the Fe $2p_{3/2}$ spectra. The ligand field splitting produced by ammonia is strong and it raises the energy of the dz^2 orbital compared to multilayer FePc, resulting in the formation of a low spin compound. As a consequence, the Fe $2p_{3/2}$ photoemission signal shows no multiplet structure for the FePc(NH_3) complex (upper spectrum), as opposed to the multilayer FePc spectrum (bottom spectrum). The high binding energy tail of the spectra is given by satellite structures [86,91].

2.2. X-Ray Absorption Spectroscopy

2.2.1. Principle

X--ray absorption spectroscopy (XAS), also known as near edge x-ray absorption fine structure (NEXAFS), is a technique that maps the unoccupied states of a sample. XAS refers to the absorption structure up to around 30 eV from the absorption edge. It is an element-specific technique since the absorption edge has a different energy for each element. It is also chemically-specific, being able to distinguish between chemically distinct environments of the same atom.

In XAS, the photon energy is scanned across an absorption edge. If the energy is sufficient, a core level electron is promoted into an unoccupied state of the sample. As a result a core hole is created and the system is left in an unstable state. The filling of the core hole takes place within femto- or attoseconds [71] (depending on the location of the core hole), either radiatively by fluorescence or non-radiatively by Auger decays. By varying the photon energy, the absorption into different unoccupied levels is probed. A schematic view of the absorption process is presented in Figure 2.11.

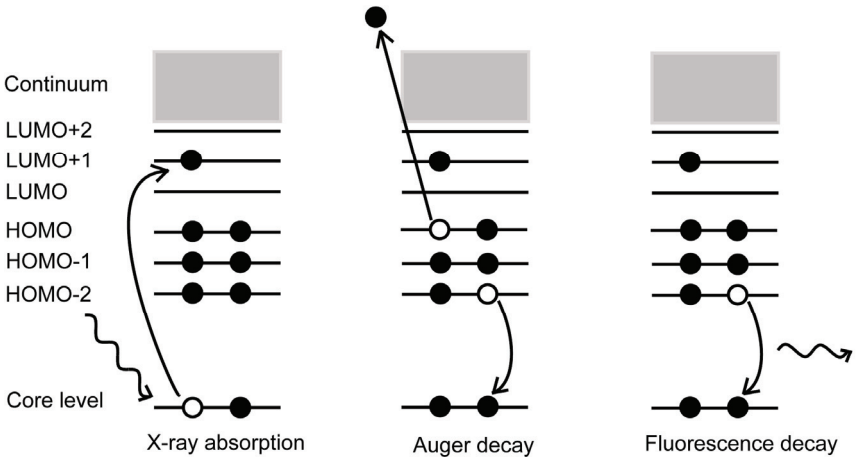

Figure 2.11. Schematic representation of the x-ray absorption processe and excited-state decay.

2.2.2. Resonance Shape, Position and Intensity

The XAS spectrum typically consists of sharp π^* and broad σ^* resonances (Figure 2.12) (for a discussion on the origin of the π^* and σ^* states see section 4.1.2). Resonances due to bonding to hydrogen atoms or due to multielectron excitations (shake-up, shake-off satellites) can also be present in some cases [92]. Only dipole transitions are allowed ($\Delta l=\pm 1$). This implies that for an initial state of *s* symmetry the excitation will take place into an unnocupied

final state of at least partial *p* character. The resonances in XAS correspond to a perturbed system: the creation of the core hole affects the position of unoccupied states, which for the ground state system are normally situated just below and above the vacuum level. For the core-excited molecule the π^* states can be shifted below the Fermi level by the Coulomb electron-hole potential. The π^* resonances appear in the absorption spectrum as sharp, well-defined resonances. On the other hand, the σ^* states normally lie in the continuum above the vacuum level, which makes them appear as broad features in the absorption spectrum [92,93].

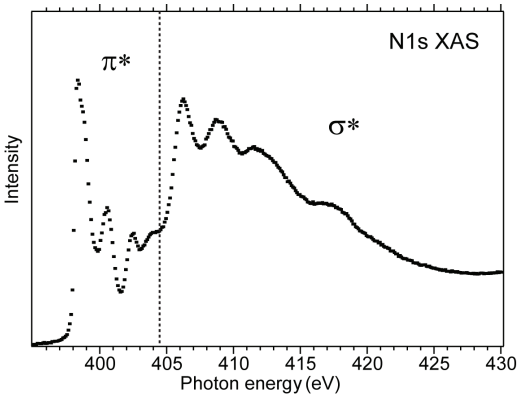

Figure 2.12. An example of N 1s XAS spectrum taken on a multilayer of FePc on HOPG. The spectrum shows sharp π^* resonances below ~405 eV and broad σ^* resonances between ~405-420 eV (the spectrum was taken in 40° incidence geometry of the photon beam with respect to the sample normal).

The intensity of the XAS signal is directly proportional to the x-ray absorption cross section (eq. 2.12). The absorption cross section can be calculated according to Fermi's golden rule and can be written as:

$$T_{i\to f}^{XAS} = \frac{4\pi^2 e^2}{m^2 c\omega}\left|\frac{\mathbf{E}}{|\mathbf{E}|}\langle f|\mathbf{p}|i\rangle\right|^2 \rho_f(E)\delta(h\nu + E_i - E_f), \qquad \text{(eq. 2.12)}$$

where *e* and *m* represent the charge and the mass of the particle, ω is the frequency of the perturbing electric field, $\mathbf{E}$ is the electric field of the light, $\mathbf{p}$ is the linear momentum operator, $\langle f|\mathbf{p}|i\rangle$ is the transition matrix element with f and i the final and the initial state, $\rho_f(E)$ is the energy density of final states, and δ is the Dirac delta function which ensures energy conservation. The cross section depends then on the density-of-final states in the presence of the core hole, which can be different from the density-of-states in the ground state. It also depends on the scalar product between the electric field vector and the linear momentum operator, which as will be shown later gives the angular dependence of the XAS resonances. Also, the matrix element indicates that an overlap between the core level and the probed unoccupied orbitals is necessary.

2.2.3. Monitoring XAS

The recording of an XAS experiment can be performed in different ways. In principle, the transmission, fluorescence yield, total electron yield, partial electron yield or Auger

electron yield methods [93] can be used. The transmission method involves the measurement of the transmitted x-ray intensity through the sample. The drawback is that it requires very thin foils to be used as samples, because the intensity decays exponential with the thickness of the sample. In some situations fluorescence decays are measured by using a fluorescence detector. It is convenient to measure the energy of electrons and it also happens that for the K edge excitations of low-atomic number elements such as C, O, N which are the main focus of the work presented in this thesis, the decays are dominated by electronic Auger transitions. The cross section for the electronic Auger decays is more than two orders of magnitude higher than that of the fluorescence [94] for these low Z elements. The Total Electron Yield (TEY) is based on the detection of electrons of all energies created by the x-ray absorption process (both elastically and inelastically scattered electrons are detected). Normally, during the x-ray absorption experiments both Auger processes and photoemission processes take place. The signal in TEY is dominated by low kinetic energy electrons. The Auger peaks can be distinguished by the fact that they are constant in kinetic energy. Most of the information comes from the inelastic processes which also include inelastically scattered Auger electrons of interest whose intensity is also proportional to the number of decays and thus to the cross-section. The TEY is mostly a bulk sensitive method because the inelastically scattered electrons carry information from deeper inside the sample. The Partial Yield Mode (PYM) uses a retarding voltage for eliminating part of the inelastic electrons. The signal is given by the elastic and part of the inelastic Auger processes. Since part of the inelastic electrons is omitted, the PEY mode renders the measurement more surface sensitive. Another possibility for detection is the so-called Auger Electron Yield (AEY). The measurements related to the present work were all carried out in AEY. The AEY requires the use of the electron energy analyzer as a detector. In AEY only the Auger peak of interest is measured, which in the present case is connected to the N 1*s* or O 1*s* excitation. The experiment is carried out by choosing a kinetic energy window around the kinetic energy of the Auger peak of interest and monitoring Auger spectra over a range of photon energies with a chosen photon energy step size. Normally the photon energy region is chosen around the absorption edge. The number of Auger decays is proportional to the number of excited electrons and thus to the absorption cross-section. AEY is the most surface sensitive mode, since the information comes from the elastic Auger process only.

2.2.4. Data Treatment

The raw result of the XAS measurement in AEY is a 3D data set (Figure 2.13(a)), where the dimensions are represented by the photon energy (left axis), the kinetic energy of the Auger electrons (bottom axis), and the absorption intensity (the colour scale). The actual

XAS spectrum (Figure 2.13(b)) is obtained by integrating the data over the kinetic energy window and displaying the so-derived absorption intensity as a function of the photon energy.

The photon energy is calibrated by recording photoemission spectra of the same core level excited by first and second order light (small fractions of higher order photons are also transmitted by the monochromator). The real photon energy is given by the difference in kinetic energy of the first and second order excitations. The intensity of the absorption spectrum strongly depends on the x-ray intensity, which changes as a function of photon energy. Each absorption spectrum is therefore corrected for intensity variations by dividing with the energy dependent photon flux. The flux is recorded by using a gold mesh (beamline I511) or a photodiode (beamline I311) placed between the monochromator and the sample. After removal of a constant background measured below the first resonance, the spectra are normalised to the intensity of the step edge at about 30 eV above the adsorption threshold, which corresponds to the continuum of states above the vacuum level (vacuum step edge) [57].

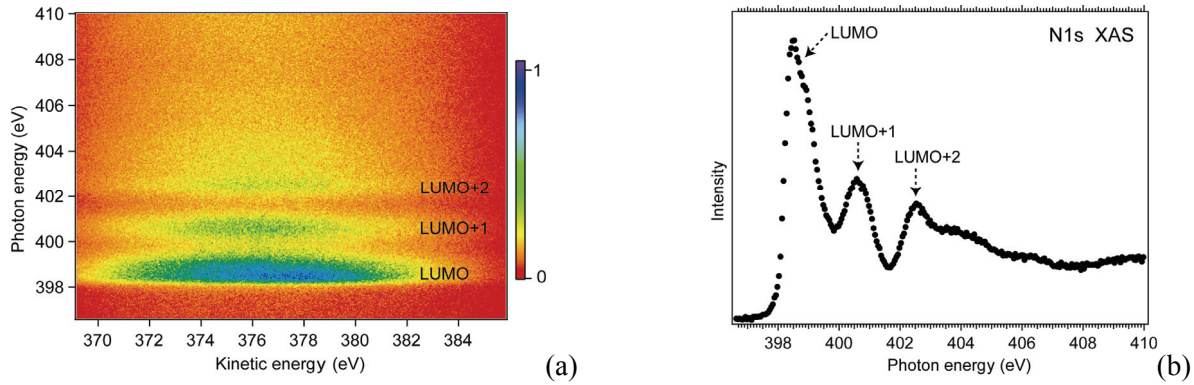

Figure 2.13. The results of an N 1*s* XAS experiment performed on a multilayer of FePc molecules on HOPG in grazing incidence of the photon beam with respect to the surface. The π^* LUMO, LUMO+1 and LUMO+2 resonances position is indicated in each graph. Each resonance represents an excitation from a 1*s* orbital to an orbital with *p* character or partial *p* character and weight on the nitrogen atoms. (a) The raw data, as obtained from the experiment displaying the Auger spectra taken for each of the photon energies of interest (the photon energies around the N 1*s* absorption edge), and (b) the actual XAS spectrum, obtained by integrating the raw data over the entire kinetic energy range.

Direct photoemission peaks arising either from the substrate or the adsorbate levels may interfere with the process and be present in the measurement window. The kinetic energy of the direct photoemission features (Figure 2.14) shifts with photon energy, while the Auger features appear at fixed kinetic energies, irrespective of the photon energy. If the photoemission features appear in the measurement window and especially if they are present for certain photon energies only, they normally create an unwanted slope in the XAS background. If such features originate from the substrate levels, the unwanted effect they create can be removed if instead of dividing by the photon flux one measures and subtracts the XAS signal of the clean sample from the spectrum of the sample/adsorbate system. An

example of a set of experimental data where direct photoemission features from the Au(111) substrate are present in the XAS experiment is shown in Figure 2.14.

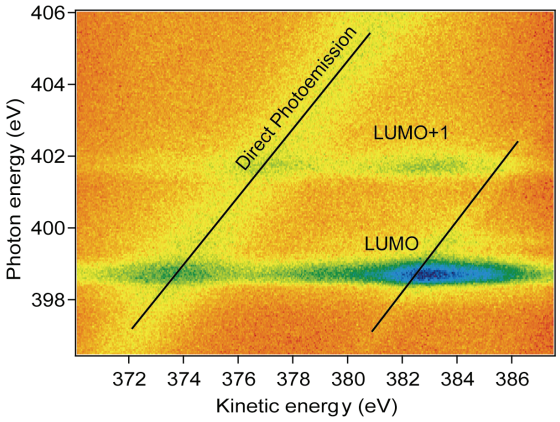

Figure 2.14. An example of direct photoemission features interfering in the XAS experiment window.

2.2.5. Angle Dependence of the Resonances. Determination of Molecular Orientation

One of the most important aspects related to the XAS technique is that it can be used as a tool for determining the orientation of adsorbed molecules with respect to the substrate, as the intensity of the resonances in the XAS spectrum changes with the angle between the electrical field vector of the light and the orientation of the molecular orbitals of the adsorbed molecule (for the measurements presented in this thesis, the electric field vector **E** was always parallel to the plane of the electron orbit in the storage ring - linearly polarised light).

This is based on the fact that the resonances intensities in XAS are proportional with the absorption cross-section (eq. 11), which has a strong angular dependence through the matrix element. More precisely it is the scalar product of the electrical field vector **E** and the linear momentum operator ***p*** that gives the angular dependence. The cross-section is then maximal when the dipole matrix element is oriented along the final state orbital (π^*, σ^* orbital). Figure 2.15 shows the XAS resonances intensity for two different orientations of the **E** vector with respect to the surface for monolayers of FePc molecules on a HOPG surface. When the **E** vector is perpendicular to the surface, the π^* resonances show maximum intensity and the σ^* are not visible in the spectrum. The opposite is observed when the **E** vector is parallel to the surface. Because the π^* and σ^* orbitals of FePc are oriented perpendicular to and in the plane of the molecule respectively, the angular dependence of the resonances is a clear proof that the monolayer FePc molecules lie flat on the HOPG surface.

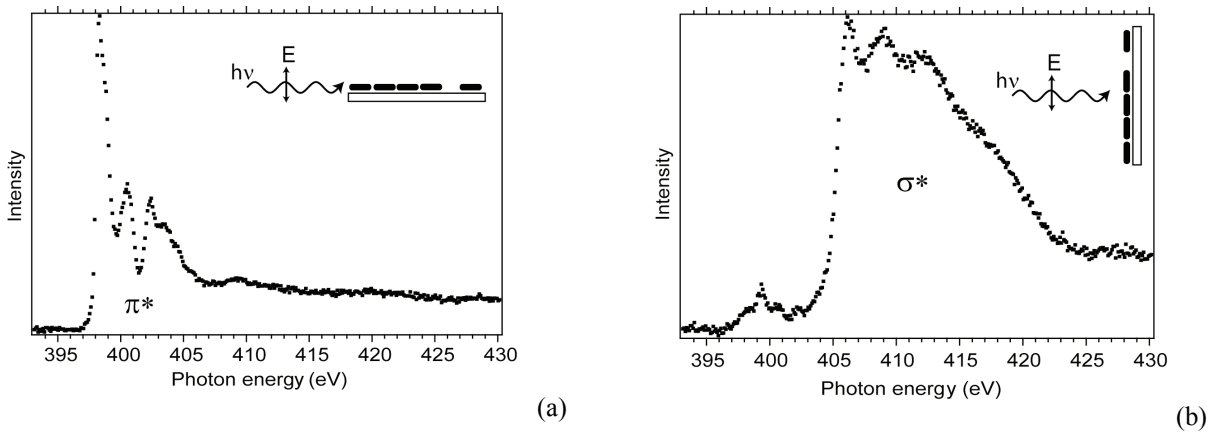

Figure 2.15. Angular dependence of the N 1*s* XAS resonances for a monolayer of FePc on HOPG. Two geometries are considered, with the electrical field **E** vector perpendicular (a) and parallel (b) to the HOPG surface. The π^* resonances are mapped when the **E** vector is perpendicular to the surface, while when the **E** vector is parallel to the surface only the σ^* states are mapped.

It is possible to make an accurate determination of the angle between the π^* or σ^* resonances and the surface. As will be discussed in the following, an experiment for the determination of the molecular tilt angle involves measuring intensity changes of a particular resonance as a function of the x-ray incidence angle θ (see Figure 2.16 for a schematic representation of the relevant angles for the XAS experiment).

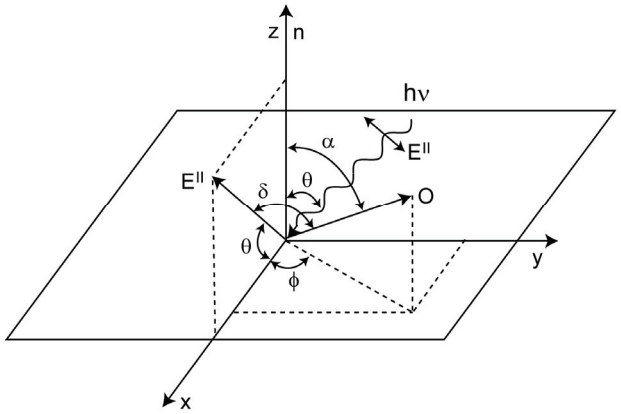

Figure 2.16. Coordinate system showing the angles of importance for determining the angular dependence of the resonances in an XAS experiment. The orientation of the final state orbital (pointing in the direction of the π^* or σ^* resonances of interest) is represented by the vector labelled **O**. The incidence angle of x-rays with respect to the surface normal is θ, which is also the angle between the $\mathbf{E}^{\|}$ component of the electric field and the surface, α is the polar angle of the final state vector orbital **O**, ϕ denotes the azimuthal orientation of the molecules relative to the substrate, and δ is the angle between the final state vector orbital **O** and the $\mathbf{E}^{\|}$ component of the electric field. The light was considered to be 100% linearly polarised, meaning that the $\mathbf{E}^{\perp}$ component of the electric field is missing. During the experiment, the light incidence angle θ is varied and XAS scans are taken for different representative angles (adapted from Ref. 93).

Changing the x-ray incidence angle produces changes in absolute intensity of the resonances. The changes in resonance intensity will be proportional to the changes in the x-ray absorption cross-section (eq. 2.13).

$$I \propto \left| \frac{\mathbf{E}}{|\mathbf{E}|} \langle f | \mathbf{p} | i \rangle \right|^2 \propto \left| \mathbf{e} \langle f | \mathbf{p} | i \rangle \right|^2, \qquad \text{(eq. 2.13)}$$

where **e** is the unit vector of the electric field.

The matrix element can also be expressed by using the dipole operator $e\mathbf{r}$ instead of the linear momentum operator **p (**eq. 2.14**)**.

$$I \propto \left| \mathbf{e} \langle f | \mathbf{r} | i \rangle \right|^2 \qquad \text{(eq. 2.14)}$$

For dipole excitations from the 1*s* core level as was the case in all the experiments conducted here, the final state orbital needs to have at least partly *p* character. The matrix element $\langle f | \mathbf{r} | i \rangle$ points then in the direction of the *p* component of the final state orbital (the final state orbital can be described by a vector O - for the examples presented in Papers I, VI and IX, the final state orbital considered for the determination of the tilt angle is a π^* orbital perpendicular to the FePc molecular plane). Based on this argument and on eq 2.14, the signal intensity can be expressed as a function of the angle δ between the electric field vector and the direction **O** of the final state orbital (eq. 2.15).

$$I \propto \left| \mathbf{e} \cdot \langle f | \mathbf{r} | i \rangle \right|^2 \propto \left| \mathbf{e} \cdot \mathbf{O} \right|^2 \propto \cos^2 \delta \,. \qquad \text{(eq 2.15)}$$

Relation 2.15 assumes 100% linearly polarised light (in the plane of the x-ray light oscillation). In reality, the degree of plane polarisation is not 100% and then both components of the electric field, namely the dominant in-plane $\mathbf{E}^{\parallel}$ component as well as the $\mathbf{E}^{\perp}$ component perpendicular to the plane of the x-ray light play a role in the absolute resonance intensity (eq. 2.16 and 2.17).

$$I \propto P \left| \langle f | \mathbf{e}^{\parallel} \cdot \mathbf{p} | i \rangle \right|^2 + (1-P) \left| \langle f | \mathbf{e}^{\perp} \cdot \mathbf{p} | i \rangle \right|^2 . \qquad \text{(eq. 2.16)}$$

$$I = A \left[P I^{\parallel} + (1-P) I^{\perp} \right]. \qquad \text{(eq. 2.17)}$$

where *P* is the degree of linear polarisation, also called polarisation factor (P=1 for 100% linearly polarised light, and for the examples presented in Papers I, VI and IX P=97%, meaning that the remaining 3% is given the out-of-plane $\mathbf{E}^{\perp}$ component) and the *A* parameter represents the absolute resonance intensity for a specific geometry.

For a three fold substrate symmetry, the angle δ between the $\mathbf{E}^{\parallel}$ component of the electric field and the final state vector **O** can be expressed in terms of the polar angle α and the angle θ according to:

$$I^{\parallel} = \cos^2(90-\theta)\cos^2\alpha + \frac{1}{2}\sin^2(90-\theta)\sin^2\alpha \,. \qquad \text{(eq. 2.18)}$$

$$I^{\perp} = \frac{1}{2}\sin^2\alpha \,. \qquad \text{(eq. 2.19)}$$

By inserting the values of $I^{\parallel}$ and $I^{\perp}$ in eq. 2.17, the absolute resonance intensity dependence on the angle θ is obtained (eq 2.20).

$$I(\theta) = A\left[P\left(\cos^2(90-\theta)\cos^2\alpha + \frac{1}{2}\sin^2(90-\theta)\sin^2\alpha\right) + (1-P)\frac{1}{2}\sin^2\alpha\right] \text{(eq 2.20)}$$

The angular dependence of the resonance intensitiy in eq. 2.20 basically shows that it is possible to determine the exact orientation of the final state orbital by determining how the absolute intensity of a particular resonance varies as a function of the angle θ. The α angle is the unknown parameter, while the value of the angle θ is chosen by the user, the A parameter can be determined for each particular θ angle from the XAS plot, and the polarisation factor is in the present case 97%. Figure 2.17 shows an example on molecular tilt angle determination from Paper I. The example refers to a monolayer of iron phthalocyanine molecules on HOPG. Here, the representation of the LUMO π^* intensity *I* as a function of the angle θ between the $\mathbf{E}^{\parallel}$ component of the electric field and the HOPG surface resulted in 0˚ tilt of the π^* resonances with respect to the surface normal. Based on the knowledge that the π^* resonances are perpendicular to the plane of the FePc macrocycle, it is possible to determine that the molecular tilt angle with respect to the surface is 0˚, indicating a perfectly flat geometry of the monolayers on the HOPG surface.

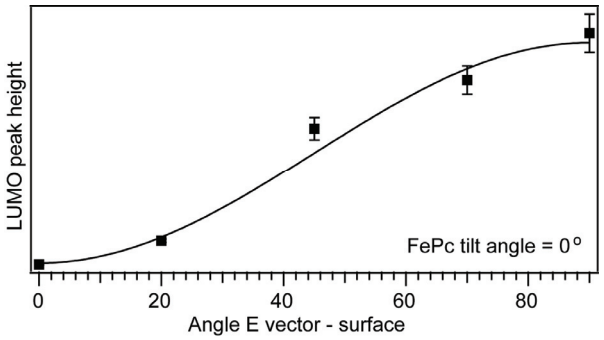

Figure 2.17. LUMO resonance intensity as a function of the angle θ between the E field and the surface. The fit shows that the π^* resonances are oriented along the surface normal (0˚±1.7˚), indicating a perfectly flat geometry of the FePc adsorbates. The degree of in-plane polarisation of the light was 97%.

2.3. Resonant Photoemission Spectroscopy

2.3.1. Principle

Resonant photoemission spectroscopy (RPES) is a technique used for studying charge transfer (CT) dynamics. Charge transfer processes at interfaces, such as those of the adsorbates with substrates, play an immensely important role in a wide range of applications, such as solar cells, molecular electronics, photochemistry, and dynamics of surface reactions [95]. More precisely, for adsorbate/surface interfaces, resonant photoemission can be used to determine whether an electron that was photoexcited into unoccupied states of the adsorbate is still localized on the adsorbate itself or if it is delocalized into the substrate levels [55,58,95,96]. Also, the timescale of delocalisation and the charge transfer time can be quantified [50,97,98,99]. Since core electrons are involved in the process, atom specificity is ensured.

RPES is based on the identification of the decay channels following the photoexcitation of core electrons into unoccupied states of the adsorbate. For the core excitations in low-Z atoms (as N 1*s* RPES considered in the present study), the decays are dominated by Auger-type transitions. The schematics of the electronic excitation and de-excitation processes are illustrated in Figure 2.18.

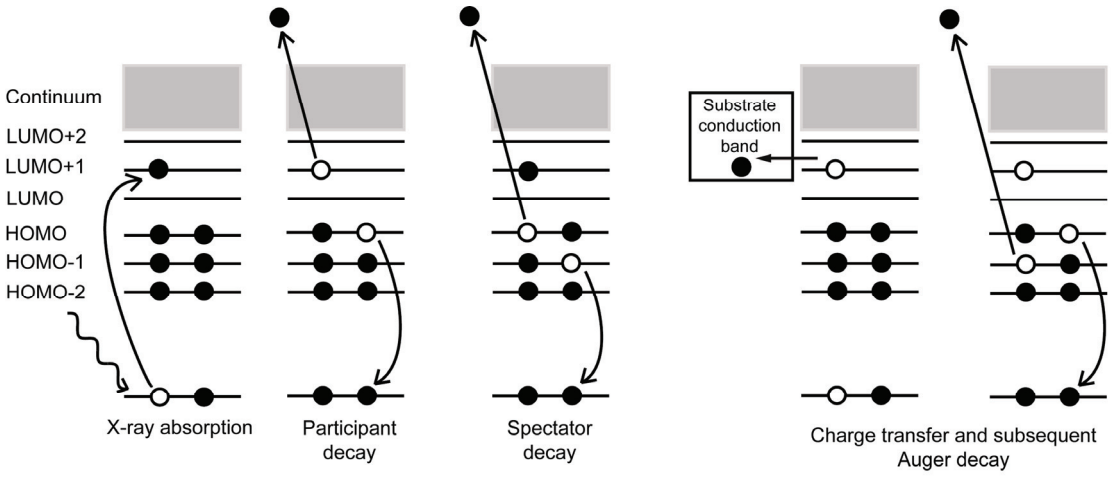

Figure 2.18. Schematics of the electron excitation and de-excitation processes involved in a RPES experiment: core level excitation into unoccupied bound states, participant decay upon resonant excitation, spectator decay following resonant excitation, and charge transfer of the excited electron into the substrate conduction band, followed by normal Auger decay.

Different decay channels might follow the excitation, some of them involving the photoexcited electron, and others not [95]. If the photoexcited electron takes part in the Auger-like decay, the process is known as *participant decay* or *resonant photoemission*. If instead the decay does not involve the photoexcited electron, the process is called *spectator*

decay or *resonant Auger*. Both participant and spectator decay channels leave the system with a +1 final state charge, as opposed to regular Auger decays following photoemission into the vacuum, which leave the system in a +2 charged state. When the adsorbed molecule is coupled to the substrate, the participant and spectator decay channels compete with the charge transfer of the excited electron into the conduction band of the sample followed by normal Auger decay.

Participant and spectator de-excitation channels can be identified by their energy dispersion behaviour. Participant channels leave the system in a final state identical to the valence band photoemission process, so they are constant in binding energy. Spectator channels leave the system in a final state similar to the normal Auger-process, meaning that they are constant in kinetic energy. In addition to normal Auger channels, spectator channels are independent of the photon energy, involving always the same occupied valence states in the decay, irrespective of the unoccupied orbital where the electron was initially excited into. The resonant photoemission experiment is conducted outside the Auger Resonant Raman (ARR) regime [55,85,99], implying that the photon bandwidth is much larger than the natural bandwidth of the core excited state. In ARR all the spectator channels are also constant in binding energy as long as the photon energy is varied within a single resonance only.

2.3.2. Conditions for Measuring Charge Transfer

The two fundamental conditions required for the study of charge transfer at interfaces are related to the energetics of the system and to the time scale of the charge transfer process. First, the adsorbate unoccupied states into which the electron is excited need to energetically overlap with unoccupied states of the substrate for the charge transfer to be energetically allowed. This overlap between the adsorbate and substrate valence states can be investigated by the alignment on a common binding energy scale of the valence band photoemission spectra (which provide information on the core-excited occupied states) with the XAS spectra (which give information on the core-excited unoccupied states) [99].

The second crucial condition is the time-scale of the charge transfer. The CT process is in competition with the decay processes that happen within the core-hole lifetime, which for the particular case of the N 1*s* is around 6 femtoseconds [71]. RPES can be used to probe charge transfer times only if the CT and the decay processes are on the same time-scale. If the CT is too slow it will obviously not take place, while too fast CT will result in complete quench of the participant (RPES) channels, which will not allow the quantification of the CT time. So in principle RPES can be used to determine CT in the fs range. The range that can be probed varies approximately from 0.1 to 10 times the lifetime of the core-excited system [99].

2.3.3. Monitoring RPES, Data Treatment and Estimation of Charge Transfer Time

Measuring RPES is similar to measuring XAS in Auger yield; the electron is photoexcited into the same unoccupied states, but in RPES the interest is directed towards the participant signal, which is constant in binding energy and has the same final state as the valence photoemission. The detection of electrons involves then measuring valence band photoemission at the photon energies of interest (around the adsorption edge, same photon energies as in XAS). The raw data as obtained from the measurement is illustrated in Figure 2.19(a).

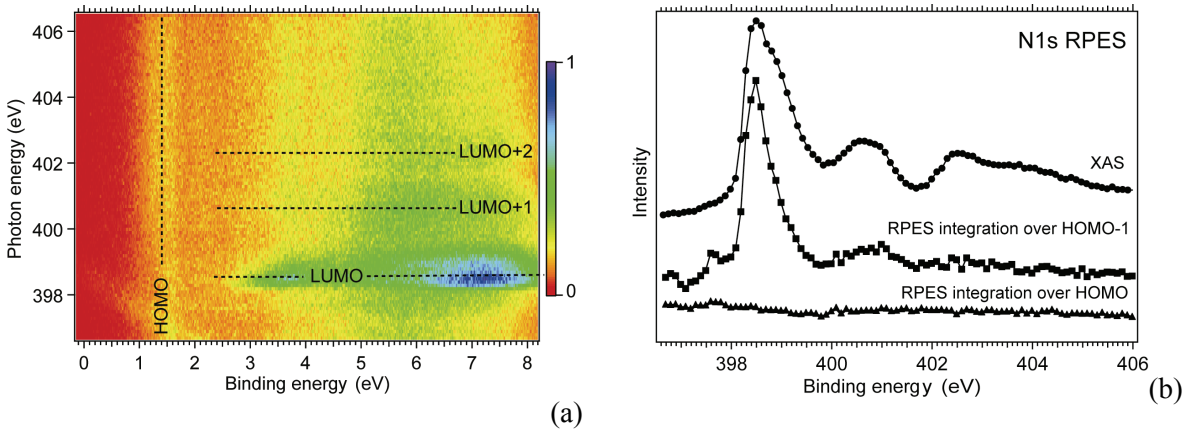

Figure 2.19. The results of an N 1*s* RPES experiment performed on a thin layer of FePc on HOPG. (a) The raw data, as obtained from the experiment displaying the valence photoemission spectra for each of the photon energies of interest (the photon energies around the N 1*s* absorption edge) and (b) the integrated RPES signal over the HOMO and HOMO-1 compared to the XAS spectrum. The quenching of the RPES intensity when integrating over the HOMO state might be an indication of ultrafast charge transfer, but, in this case it is not, because the HOMO state (as proven by calculations) does not have contribution from the nitrogen atom, so there is no overlap between the HOMO and the unoccupied states with weight on the nitrogen atom. The relative intensity of the RPES signal obtained when integrating over the HOMO-1 compared to the XAS instead indicates that no charge transfer from the LUMO and LUMO+1 of the FePc and the HOPG substrate takes place (the signal reduction corresponds to what is reported in literature [55] for isolated systems, being due to matrix element effects only).

The measurement window includes several contributions, the participant signal, the spectator and normal Auger processes, and valence band photoemission features. The possibility of separating the resonant from the non-resonant channels in the spectra makes it possible to get information about the possibility of charge transfer. Participant channels are characterized by a higher kinetic energy and thus lower binding energy compared to the spectator and normal Auger channels. The participant-spectator energy separation corresponds to the effective HOMO-LUMO gap (the highest occupied orbital and the lowest unoccupied molecular orbital with contribution from the nitrogen atom). The spectator contribution can also be separated from the normal Auger by the so-called “spectator-shift” towards higher kinetic energies due to the additional screening provided by the excited

electron [55]. The RPES spectrum is obtained by integration over the binding energy range where only participant contribution is expected (Figure 2.19(b)).

For the estimation of CT times, it is necessary to measure XAS and RPES spectra for both the system of interest (the system with potential charge transfer) and for the isolated system. The multilayer is normally used as an indicator of isolated molecules, assuming that charge transfer is not likely to occur in the multilayer [55,58,95]. First, for a qualitative indication on whether or not any CT takes place, the RPES signal of interest is compared to the multilayer RPES. Any reduction in the intensity of the participant signal compared to the isolated multilayer molecules is an indication of ultrafast charge transfer at the adsorbate-substrate interface. This procedure implies that the RPES signal of interest is scaled with respect to the signal of the isolated system, which is normally achieved by normalisation with respect to the LUMO resonance of the multilayer.

Second, for more quantitative charge transfer information, in particular for estimation of charge transfer times, comparison of the RPES and XAS intensities is needed [50] (the RPES contains part of the XAS signal). Crucial for these procedures is that the spectra need to be scaled with each other. If proven that charge transfer from the LUMO is not allowed (energetically, for example), then the RPES LUMO intensity is normalised to the intensity of the XAS LUMO resonance [50,55]. However, even in the absence of charge transfer, for example in the multilayer case the RPES signal is typically less intense than the XAS signal, but in this case it is due to matrix element effects only [55]. When CT takes place, the RPES signal intensity relative to XAS is further decreased compared to the multilayer. This further decrease with respect to the isolated system happens because the participant channels will be partly quenched in favour of the normal Auger process following the delocalisation of the excited electron into the substrate. According to Ref. 50, 55, 58, the charge transfer time can be estimated by equation 2.21.

$$\tau_{CT} = \frac{I_{RPES} / I_{XAS}}{\left(I_{RPES} / I_{XAS}\right)_{isolated} - \left(I_{RPES} / I_{XAS}\right)} \cdot \tau_C \,. \qquad \text{(eq. 2.21)}$$

In the equation above, τ_{CT} represents the charge transfer time, τ_C is the N 1*s* core hole lifetime, I_{RPES} / I_{XAS} represents the intensity ratio between the RPES and XAS signal intensity for the resonance of interest (eg. LUMO+1, LUMO+2) on the system with CT, and $\left(I_{RPES} / I_{XAS}\right)_{isolated}$ is the corresponding ratio for the isolated system (multilayer).

2.4. Equipment for Spectroscopy

The x-ray photoemission, x-ray absorption and resonant photoemission spectroscopy experiments were conducted at beam lines I311 [100] and I511 [101] at the national synchrotron facility MAX-lab in Lund, Sweden. Such experiments require the existence of an x-ray source, an electron energy analyzer, a monochromator and ultra high vacuum conditions (10^{-9}-10^{-12} mbar).

The idea behind the synchrotron radiation generation is based on acceleration of charged particles, resulting in the creation of relativistic electrons. Deflection of the electrons trajectory by magnetic fields determines the emission of synchrotron radiation. The electron beam [102] is generated in an electron gun by thermal emission. The electrons are extracted by applying alternating high voltages which results in creation of electron bunches. The electron bunches are accelerated in two linear accelerators (so-called Linacs) in the presence of high electric fields. After being recirculated twice through the Linacs, the electrons reach the energy of 500 MeV, the energy at which they are injected into the MAX II storage ring. MAX II has a circumference of 90 m. Inside MAX II, the electrons are further accelerated up to relativistic speeds and energy of 1.5 GeV. This acceleration is accomplished by an accelerating radio frequency cavity (also called RF cavity) that operates at a frequency of 100 MHz. The electrons pass this cavity once at every cycle inside the ring. The RF cavity is also important because it compensates for the energy loss due to synchrotron radiation emission. MAX II consists of a series of different magnets that direct and focus the electron beam. The synchrotron radiation is emitted in pulses of 300 ps, into a narrow cone in the forward direction, at every point where the electron follows a curved path. The energy range of the photons at the used beam lines varies from about 30 to 1500 eV. In normal operating conditions, the lifetime of the electron beam is around 24 h.

To improve the characteristics of the synchrotron radiation, insertion devices, namely undulators and wigglers are placed along the electron beam path inside the storage ring. Undulators are used for generating the synchrotron light at beam lines I311 and I511. The main advantage of using undulators compared to bending magnets is that undulators produce more intense radiation due to interference effects. The undulator radiation spectrum is not continuous, but rather consists of a series of sharp peaks, called harmonics. An undulator (Figure 2.20) is a periodic array of alternating magnetic poles that direct the beam onto a sinusoidal path [103,104]. The electron beam emits light every time the trajectory is deflected inside the undulator and there is interference of the light emitted at different points, which creates a more intense x-ray beam.

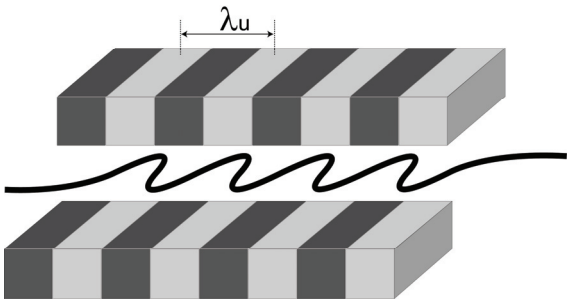

Figure 2.20.Schematic illustration of an undulator magnet.

Two important parameters related to undulators [105] are the period length (λ_u which corresponds to the wave length of the alternating magnetic field) and the dimensionless K parameter, also called undulator strength ($K=eB_0\lambda_u/2\pi m_0 c$, where e is the electron charge, B_0 the magnetic field, m_0 the electron rest mass and c the speed of light). The undulator magnet at the beam line I311 has a period length of 66 mm and 77 magnetic poles. The maximum value of the magnetic field (B_{max}) is 0.73 T, and the maximum value of the undulator strength parameter K is 4.5 [100]. The position of maximum intensity for a particular harmonic can be changed by adjusting the undulator gap [104]. Changing the undulator gap affects the size of the magnetic field, and through the magnetic field the undulator strength parameter K and, as a result, the photon energy at which one gets the maximum intensity. For a planar undulator, the resulting synchrotron radiation is linearly polarized in the plane of light oscillation, which is very important, for example in performing x-ray absorption spectroscopy experiments. For the particular case of XAS experiments, because the photon energy is scanned during the measurement, a taper is applied to the undulator to reduce intensity variations of radiation with the photon energy. This basically implies that the gap size is different at the two ends of the undulator, resulting in non constant K values along the undulator length, and creating a more continuous spectrum of radiation, with the intensity more evenly distributed with photon energy.

At the exit from the storage ring there are the beam lines, whose endpoints are the experimental stations. Figure 2.21 shows a schematic view of the I311 beam line, as given in reference [100]. The main components of the beam line are mirrors, the monochromator, and the monochromator exit slit. The monochromator [106] is used to extract a single wavelength from the continuous spectrum resulting x-rays, which is essential for the experiments. This wavelength selection is achieved through the help of diffraction gratings and mirrors. The grating divides the light over different angles according to the wavelength and the mirrors are the used to focus the desired wavelength onto the exit slit. The monochromator exit slit is extremely important because it improves the photon energy resolution by selecting only a part of the photon bandwidth. According to the experimental requirements, the size of the

monochromator exit slit can be changed to either maximize the photon energy resolution or the photon flux.

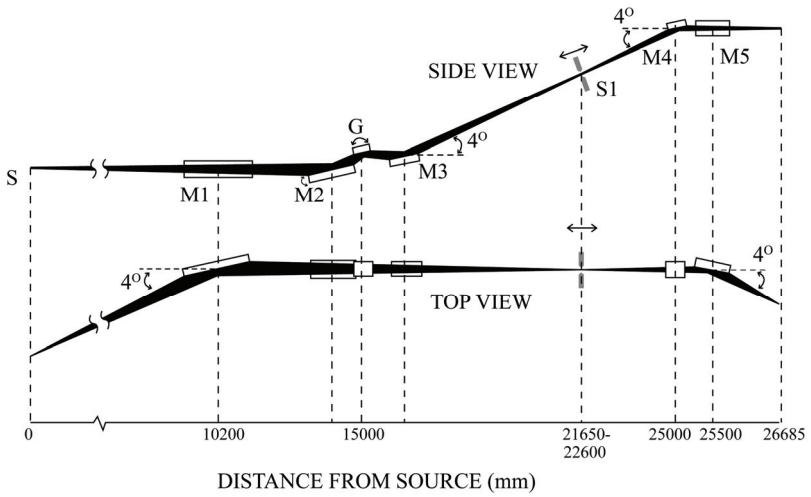

Figure 2.21. Schematic layout of I311 beam line, as given in reference [100]. The electron source S is placed at 0 mm. G is the monochromator plane grating, S1 is the adjustable monochromator exit slit, and M1-M5 are mirrors (M1 is a horizontally focusing pre-mirror; M2 is a rotatable plane mirror, M3 is a spherical focusing mirror; M4 and M5 are spherical horizontal and vertical re-focusing mirrors placed in the close vicinity of the experimental chamber).

The I311 beam line has two end stations, the spectroscopy station and the PEEM (photoemission electron microscopy) end station. The spectroscopy end stations of beam lines I311 and I511 consist of two chambers each, the preparation chamber where the sample cleaning and deposition procedures are carried out, and the analysis chamber, where the actual spectroscopic experiments are performed. The base pressure in the preparation and analysis chambers of beam line I311 is in the high 10^{-11} mbar range, while at the I511 end station the base pressure is in the mid 10^{-10} mbar range in the preparation chamber and low 10^{-10} mbar range in the analysis chamber. An electron gun, a LEED (low energy electron diffraction) setup, and a mass spectrometer are attached to the preparation chamber. There is also the possibility of hosting molecule evaporators. Attached to the preparation chamber is the gas-inlet system which allows dosing well defined amounts of gases onto the sample. A manipulator with possibility of cooling down to liquid nitrogen or liquid helium temperature is used to hold and transfer the sample between the preparation and analysis chamber. The analysis chamber hosts the SCIENTA hemispherical electron energy analyzer (SCIENTA SES200 at beam line I311 and SCIENTA R4000 at beam line I511).

The hemispherical electron energy analyzer (Figure 2.22) is used to measure the kinetic energy distribution of the photoelectrons [107-110]. Inside the analyzer the electrons are dispersed according to their kinetic energy, each particular kinetic energy is focused on a different channel on the detector. The main constituents of the analyzer are the electrostatic

lens system, the two concentric hemispheres, the micro channel plate detector (MCP), a phosphorus screen and a charge-coupled device (CCD) camera. The photoemitted electrons enter the analyzer through the electrostatic lens system, which collects a fraction of the photoemitted electrons, focuses them onto the entrance slit, and very important, it acts to accelerate or retard the electrons to a specific kinetic energy value called pass energy (E_p). Next, the electrons pass through the concentric hemispheres, in between which a constant potential difference is applied (+V on the inner sphere and –V on the outer sphere). The electric field in between the hemispheres bends the electron trajectory differently as a function of their kinetic energy. Electrons with too high or low energy will hit the outer and inner hemisphere, respectively, and be lost. Electrons with well defined energy ($E_p \pm \Delta E$) will pass through the hemispheres, be focused onto the analyzer exit slit and reach the MCP detector. Inside the detector channels, the signal is multiplied by a factor of approximately 10^7 [106] by the creation of secondary electrons. The secondaries are accelerated towards a phosphorus screen where the signal is converted into visible light and subsequently recorded by the CCD camera. The signal intensity is proportional to the number of electrons at a particular kinetic energy.

During a particular experiment, the value of the pass energy is kept constant and it is the acceleration-retardation voltage (V_{ar}) in the lens system that is swept over the desired range, which allows electrons of different kinetic energies to reach the MCP detector at different times and be counted. The MCP detector [111-113] consists of a 2D array of channels. One dimension corresponds to the energy dispersive direction, while the second corresponds to the angular distribution of the photoelectrons (when performing angular mode experiments, electrons with angular distribution of ±10˚ for SCIENTA SES200 and ±15˚ for SCIENTA R4000 can be resolved [114]). For a regular photoemission experiment (non-angle resolved) the signal from the channels in the non energy dispersive direction is integrated. Each kinetic energy is counted by each channel in the energy dispersive direction and the final signal is a sum over all the channels. This procedure eliminates the difference in sensitivity between the detector channels.

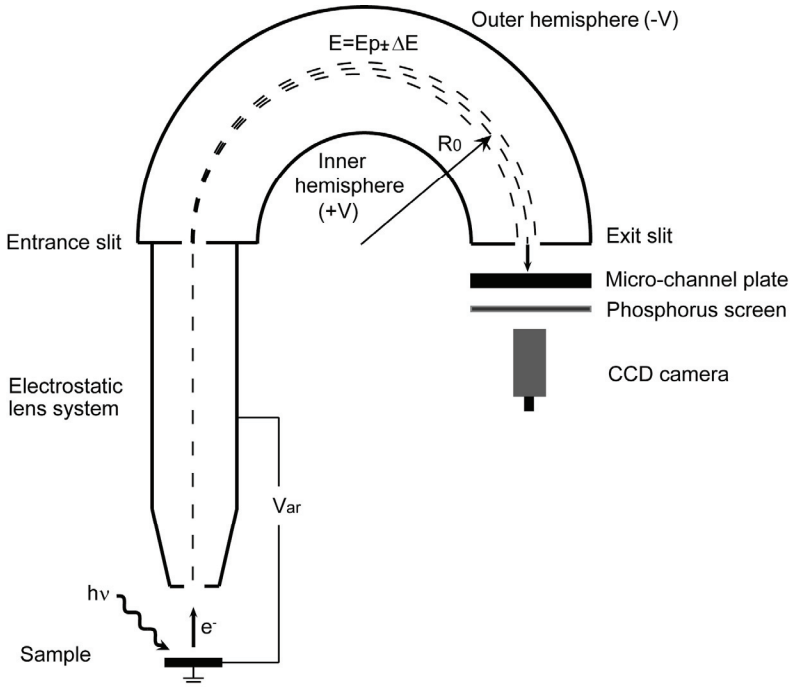

Figure 2.22. Schematic view of the hemispherical electron energy analyzer. The photoelectrons are retarded to the pass energy (E_p) and focused onto the entrance slit by means of the electrostatic lens system. Only electrons with energy $E_p \pm \Delta E$ are focused onto the exit slit and reach the MCP detector. The signal intensity is measured by the help of a phosphorus screen and a CCD camera. The signal is further recorded by a computer.

In reality, the photoemission signal is broadened due to the fact that not only electrons with energy equal to E_p, but rather $E_p \pm \Delta E$ are focused onto the exit, and also because the of the finite size of the entrance slit width. Electrons with energy slightly higher or lower with respect to the pass energy ($E_p \pm \Delta E$) will also pass through the hemispheres and because of their different energies they will reach different channels on the MCP detector in the energy dispersive direction. The value of ΔE changes with the pass energy; the lower the pass energy, the narrower the ΔE interval. In consequence lower pass energy leads to narrower electron energy range that reaches the MCP detector and thus better resolution. The finite size of the analyzer slit allows collecting a beam of electrons with some specific angular distribution and possibly slightly different energies. This creates the possibility that different energies reach a particular channel in the detector in the same time, inducing additional broadening. The analyzer resolution [109,115] can be expressed as $(E_p \times s)/2R_0$, where E_p is the pass energy, s is the analyzer slit width, and R_0 is the curvature radius of the analyzer. Improving the resolution implies loosing some of signal intensity, but it is always the case that a compromise needs to be achieved between signal intensity and resolution.

CHAPTER 3

Scanning Tunnelling Microscopy

3.1. Principle

The invention of the scanning tunnelling microscope by Gerd Binning and Heinrich Rohrer (1982) was awarded the Nobel Prize in 1986. Scanning tunnelling microscopy (STM) is a technique capable of direct imaging of the surface structure with atomic resolution [116,117]. The lateral resolution height resolution are in the sub-Ångström range [94,117]. The principle is based on the quantum mechanical phenomenon of tunnelling (the flow of electrons between two conductors separated by a sufficiently small potential barrier). In the ideal case, an atomically sharp tip is brought very close to a conductive sample (within a couple of Ångströms), most often in ultra-high vacuum conditions, and a small potential difference is applied between the tip and the sample (smaller than the work function). A net electron flow will be established from the sample to the tip or from the tip to the sample, depending on the polarity of the voltage. The electron flow produces a small, detectable current, called tunnelling current, which can be amplified and subsequently recorded by a computer.

The tunnelling current (I) decays exponentially on the tip-sample gap width and height, and can be approximated by the following equation (eq. 3.1) [118]:

$$I \propto \exp\left(-2d\frac{\sqrt{2m\Phi}}{\hbar}\right). \qquad \text{(eq. 3.1)}$$

where d represents the tip-sample separation (gap width), m is the electron mass, Φ the height of the vacuum barrier (related to the work functions of the tip and sample) and $\hbar$ is the reduced Planck's constant. The current drops by nearly one order of magnitude per 1 Å change in the tip-sample distance [116,117,119], making it possible to obtain atomically resolved STM images. Basically, due to the corrugation individual atoms on the surface create variations of the tunnelling current as the tip is scanned across the surface. The tip-sample separation is normally within the 0.1-10 Å range and the magnitude of the tunnelling current is in the pA-nA range [94,120,117].

3.2. STM Theory

In 1983, Tersoff and Hamann [121,122] developed a quantitative description of the tunnelling current by making use of Bardeen's approach for estimating the matrix element [123] for tunnelling between two metals separated by a thin oxide layer. Their analysis showed that the tunnelling current is proportional to the constant local density-of-states of the surface at the Fermi level, as will be discussed. The tunnelling current can be written as:

$$I = \frac{2\pi e}{\hbar}\sum_{t,s} f\left(E_t\right)\left[1 - f\left(E_s + eV\right)\right]\left|M_{ts}\right|^2 \delta(E_t - E_s), \qquad \text{(eq. 3.2)}$$

where *t* and *s* refer to the tip and sample, respectively, *f(E)* represents the Fermi function, *V* is the applied voltage, M_{ts} represents the tunnelling matrix element between the states of the tip and the states of the sample, E_t and E_s represent the energy of the tip and sample states.

One crucial point in estimating the tunnelling current is to evaluate the matrix element. This can be done based on Bardeen's approach which showed that the tunnelling matrix element is given by the overlap between the tip and sample wave functions and can be calculated by a surface integral over any surface located entirely within the vacuum region separating the two conductors (the tip and sample in this particular case) (eq. 3.3).

$$M_{ts} = -\frac{\hbar^2}{2m}\int\left(\Psi_t^* \vec{\nabla}\Psi_s - \Psi_s \vec{\nabla}\Psi_t^*\right) d\vec{S} \qquad \text{(eq. 3.3)}$$

In the equation above *m* is the electron mass, Ψ_t and Ψ_s are the wave functions of the tip and sample respectively. The matrix element is independent of the energy of the states involved in the tunnelling process but requires that the wave functions of the tip and sample are known. In general, the exact atomic structure of the tip is unknown. In their approach, Tersoff and Hamann assumed an ideal case, where the tip is approximated by an *s*-like wave function point probe with the radius of curvature r_0. In addition, one has to consider the experimental conditions of small voltages (around 10 meV for metallic samples) and temperatures (room temperature or below). The tunnelling current is then given by the local density-of-states (LDOS) of the sample at the Fermi level (eq. 3.4)

$$I \propto \sum_s \left|\psi_s(r_0)\right|^2 \delta(E_s - E_F) \equiv \rho(r_0, E_F), \qquad \text{(eq. 3.4)}$$

where $\rho(r_0, E_F)$ is the LDOS at the Fermi level at the position of the tip. The STM image then represents a contour of constant LDOS of the sample.

With a negative bias applied to the sample, the electron flow is directed from the occupied states of the sample to the unoccupied states of the tip, and the resulting STM image will be a contour of the occupied states of the sample. If the polarity of the voltage is changed, the electron flow is reversed, allowing in this case the mapping of the unoccupied states of

the sample. A schematic of the energy levels involved in tunnelling [119,124] is shown in Figure 3.1.

Some more advanced theories calculate the tunnelling current by considering bias voltages in the order of eV [125-127] and some also take into account more realistic tip shapes [128,129], but such descriptions are beyond the scope of the present thesis.

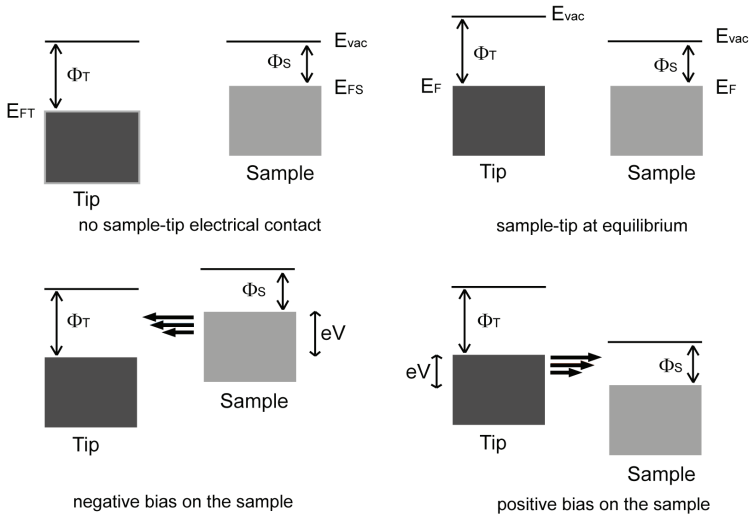

Figure 3.1. Schematic illustration of the sample and tip energetic levels in the absence of any electrical contact, in electrical contact at equilibrium in vacuum, and in tunnelling conditions when a small negative or positive bias are applied to the sample.

3.3. Imaging Modes

There are two basic scanning modes that can be used in STM, the constant current and constant height modes [94,118]. The constant current mode is the most commonly used imaging mode. Figure 3.2 shows the schematics of an STM experiment performed in constant current mode. The tunnelling current is kept constant by the help of the feed back loop while the tip is scanning the surface. This is achieved by adjusting the tip-sample distance by changing the voltage on the piezo element. A topographic image of the surface is obtained in this mode by plotting the piezo feedback voltage as a function of the lateral tip position. In reality, the situation is more complicated. Most often, an STM image represents a superposition of topographic and electronic structure effects. Large-scale images can often be considered to contain pure topographic effects, while atomic-scale images contain combined geometric and electronic structure effects. In constant height mode, the tip position in the z–direction is kept constant while the tip is scanning the surface in the xy- direction. The tunnelling current is then adjusted at every point in such a way to maintain the z- position of the tip constant. The image is represented by plotting the tunnelling current as a function of lateral tip position.

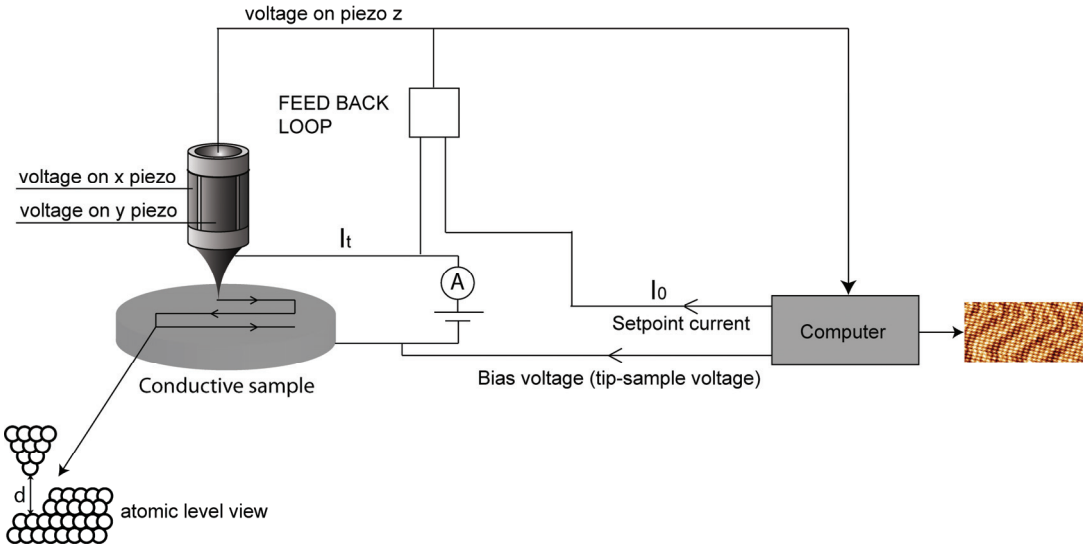

Figure 3.2. Schematic representation of the STM experiment. The tunnelling current and the bias voltage are set by the user. The tip scans the surface in x- and y- directions and, by the help of the electronic feed-back loop, the position of the tip is continuously adjusted while the tip is scanning the surface in such a way to maintain the tunnelling current (I_t) constant with respect to a preset value (I_0 or setpoint current). The tip is scanned line by line across the surface and the computer displays the overall STM image containing all the line-scans.

Figure 3.3 is an example of constant current mode imaging of an FePc submonolayer and monolayer on a Au(111) surface. The molecules have a four lobe star appearance with a bright protrusion in the centre. Each lobe corresponds to the benzene rings situated at the edge of the FePc molecule and the bright spot is due to the tunnelling mediated by the partly filled *d* states of the Fe atom situated close to Fermi level [130]. At very low coverages, when only the step edges are decorated, the molecules seem to adopt a standing geometry. The molecules on the terraces instead are oriented with the molecular plane parallel to the Au(111) surface, so at monolayer coverage the molecules appear flat on the surface.

(a) (b)

Figure 3.3. An example of constant current STM images of FePc on Au(111) at the initial stages of growth (a), and at monolayer coverage (b). The images were taken with a low temperature SPECS Århus STM instrument. (a) 300Å×150Å, 0.24nA, 1.27V and (b) 70Å×70Å, 0.3nA, 1.25V.

3.4. Equipment for STM

For the STM experiments, the low temperature SPECS Århus STM [120] at the Surface Science Laboratory, Department of Condensed Matter Physics at the Universidad Autónoma de Madrid, was used. The STM instrument in Madrid is capable of liquid nitrogen cooling; the lowest temperature that can be achieved is around 113 K. The scanning is done by a tungsten tip supported by a cylindrical piezoelectric element. The instrument consists of an analysis chamber and a preparation chamber. The cleaning and deposition procedures are carried out in the preparation chamber and the actual STM experiments in the analysis chamber. The preparation chamber is equipped with a sputter gun, LEED equipment and an electrically controlled manipulator. The manipulator allows heating the sample by electron bombardment and facilitates the sample transfer in between the main chambers. The temperature reading is done by a thermocouple attached in proximity of the sample. The instrument also offers the possibility of *in-situ* dosing molecules in the analysis chamber. Vibrational damping of the instrument is of extreme importance because of the need of sub-Ångström precision in both lateral and vertical tip positioning. Spring systems are normally used for such purpose [116].

The key part of the STM instrument is the STM stage setup, used for the actual recording of the STM images. In order to record the STM images, an atomically sharp electrochemically etched tungsten tip (or, alternatively a Pt/Ir tip mechanically cut) controlled by a piezoelectric scanner is scanned over an atomically flat surface. Piezoelectric materials have the ability to contract or expand in the presence of electric fields. The STM piezoelectric element has the ability of contracting or expanding by 1 Å/mV which gives ultrahigh position precision when scanning the tip along the surface. Either tripod scanners or tubular scanners are used [120,131]. The tripod scanner consists of three orthogonal piezoelectric rods, responsible for the movement of the tip in the x-, y-, and z- directions. The SPECS Århus STM uses instead a tubular piezoelectric scanner, with the advantage of having higher resonant frequency (due to more compact design) with respect to the tripod scanner. The higher resonant frequency implies that the sensitivity of STM to external vibrations is significantly reduced, allowing significantly lower acquisition times for the images. The tubular piezo scanner is composed of different electrodes, an internal electrode which has a continuous structure and an external electrode which is divided into four sections. For movement in the z- direction, a voltage is applied on the inner electrode with respect to the external ones, causing the length of the tube to be expanded or contracted. For movement in the x- and y- directions, different polarity voltages are applied on opposite sides of the external electrode.

CHAPTER 4

Adsorbates, Substrates, and Intermolecular Interactions

4.1. Adsorbates

4.1.1. Phthalocyanines

Phthalocyanines are synthetic organic macrocyclic compounds consisting of four isoindole units linked together by four bridging nitrogen atoms. Phthalocyanine complexes were first synthetised in the period 1907-1927, and in 1928 they were first produced at industrial scale [1,2]. Phthalocyanines can be metal-free (H_2Pc) or a metal atom (MePc), most often one of the first-row transition metals, can be bound to the four pyrrole nitrogen atoms (Figure 4.1).

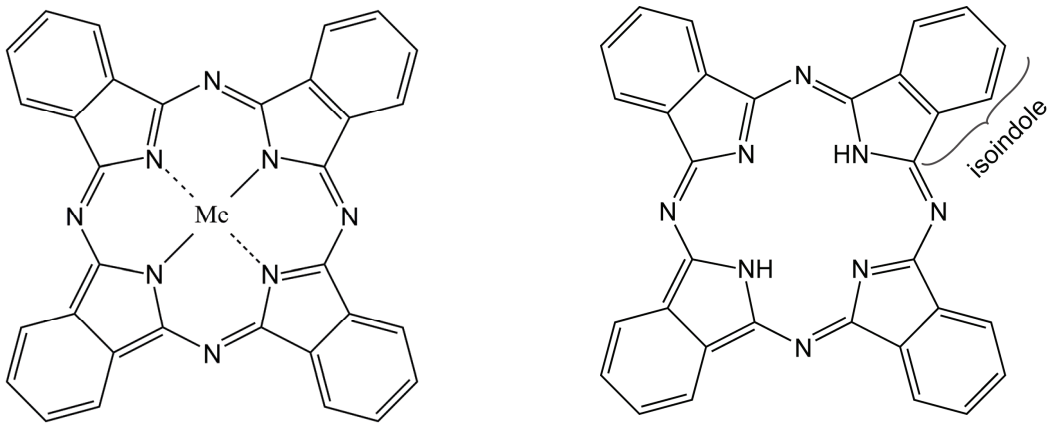

Figure 4.1. The molecular structure of the metal phthalocyanine (MePc, $C_{32}H_{16}N_8Me$) and metal-free phthalocyanine (H_2Pc, $C_{32}H_{16}N_8H_2$) molecules. The molecules have aromatic character due to delocalized π bonds.

Phthalocyanines are planar molecules, except for a few cases such as the tin and lead phthalocyanines (SnPc and PbPc) [132-136], where the central metal ion is too large to be accommodated into the cavity and it lies outside the macrocycle ring. The macrocycles

contain delocalized π bonds and have aromatic character. As a consequence of the aromaticity, phthalocyanines exhibit promising electronic and optical properties, high thermal and chemical stability, and stability upon exposure to intense electromagnetic radiation. Their stability is enhanced with respect to the related porphyrin molecules, because of the presence of benzene rings and bridging nitrogen atoms [2]. For example, phthalocyanines remain intact up to around 500^{o}C and the metal cannot be removed even with concentrated sulphuric acid [1,38]. In some cases (such as CuPc, CoPc and FePc which is the main focus of this paper), the metal is so strongly bound that it can only be removed when breaking the macrocycle [137]. The most commonly used phthalocyanines contain one of the first row transition metals in the centre, but in total there are around 70 elements that can form phthalocyanine compounds [2].

The iron phthalocyanine (FePc) molecule, which is the main focus of the research work presented here, contains an iron ion in the +2 oxidation state and is a paramagnetic compound, both when free or adsorbed on Au(111) [130,138-141]. It has a d^6 electron configuration on the iron atom (Figure 4.2) with two unpaired electrons (S=1). The Fe is involved in two covalent and two coordinate bonds with the nitrogen atoms of the pyrrole rings. The ligand field splitting in the square planar FePc complex results in the dx^2-y^2 orbital being higher in energy with respect to the *d*xy, *d*yx, *d*xz and dz^2 orbitals which are very close in energy. In consequence the electrons are distributed among the lower energy orbitals.

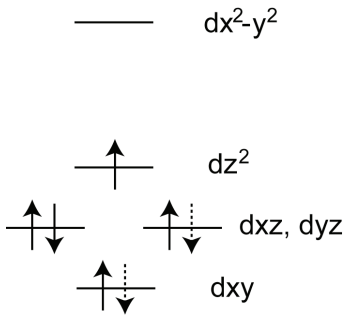

Figure 4.2. A schematic representation of the *d* orbital energy diagram of the FePc molecule [130,138]. A single configuration cannot be used to describe the ground state electron distribution and for this reason the dashed arrows show partial occupancy of the indicated orbitals by one electron.

The properties of phthalocyanines are closely related to their electronic structure. In particular, phthalocyanines containing certain transition metals (such as Cr, Mn, Fe, Co) have a quite complex electronic structure, with unpaired spins in the *d* valence band. The electronic and magnetic properties of phthalocyanines and phthalocyanines on surfaces can be modified by changing the metal atom in the centre [130,139,142-144], by attaching different functional groups [145,146], by atom by atom manipulation [147,148], or as discussed in this thesis by changes in the structure of the support surface [Papers II,III, Ref. 149-155] or adsorption of ligands on the macrocycle [Papers II-VII, Ref. 156-158]. All the above mentioned aspects emphasize the interesting idea of tailoring the electronic structure of phthalocyanines towards desired purposes. However, while different experimental and

theoretical studies indicate the possibility of tailoring the molecular properties, a precise control towards well defined, specific properties is still a subject that needs further research.

In the following, a couple of illustrative examples from the literature on how the electronic structure of phthalocyanianes can be influenced by the different parameters mentioned above will be given. First, the importance of the metal atom in the centre will be emphasised. For example, by using DFT calculations, Liao *et al.*. [139] were able to show that the valence electronic structure of FePc and CoPc is significantly different from that of NiPc, ZnPc and MgPc. They found that in FePc and CoPc the highest occupied molecular oribital[4] (HOMO) has predominantly metal-*d* character, while in NiPc, ZnPc and MgPc, the HOMO is localised on the phthalocyanine ring, with no contribution from the metal-*d* states. The influence of different metals with different filling of the *d* states is also nicely illustrated by the experimental STM work of Lu *et al.* [130,143], who studied d^6 to d^9 metal phthalocyanine configurations on Au(111). Their results show that in the case of FePc and CoPc that have significant *d*-metal orbital contribution near the Fermi level the metal atom appears as a bright protrusion, while NiPc and CuPc that do not have significant *d* orbital character at the Fermi level the metal appears as a hole in the centre of the four lobe star represented by the hydrocarbon ring. Some valence-band photoemission studies show that the presence of different metals with different *d* orbital filling significantly affects the MePc-substrate interaction [144,159,160]. In this respect, FePc and CoPc were found to have strong coupling with the Au(111) surface, compared to NiPc and ZnPc.

As expected, the substrate plays an important role as well. The same molecule on different substrates exhibits different coupling strengths. In Paper I and III, we found that FePc only very weakly couples to the HOPG substrate (van der Waals interactions), while the FePc-Au(111) coupling has covalent character, with significant hybridisation between the Au(111) states and the *d* states of the Fe. Another example is the study by Takami *et al.* [155], who concluded that the FePc-Ag(111) interaction is stronger than the FePc-Au(111) interaction.

Some examples on how the magnetic properties of phthalocyanines can be influenced by certain parameters are briefly discussed in the following. Zhao *et al.* [147] were able to show by STM and STS the possibility of controlling the Kondo effect[5] arising from coupling magnetic Co^{+2} ions in CoPc with a nonmagnetic Au(111) surface by changing the chemical surroundings. They managed to perform single atom manipulation and dehydrogenate the CoPc molecule with the help of voltage pulses. After dehydrogenation, the interaction between the molecule and the substrate becomes stronger and coupling of CoPc and Au spins occurs, resulting in a Kondo effect. Another example by Tsukahara *et al.* [161] shows how

[4] Highest occupied molecular orbital - represents the level which is last filled with electrons in a molecule.
[5] Kondo effect [147] refers to coupling between localised spins on magnetic impurities and the sea of conduction electrons on a nonmagnetic material

the molecule-substrate coupling might influence the total spin of the adsorbate molecules. They found that the spin of the FePc molecule is preserved when adsorbed on a Cu(110)(2×1)-O surface, while on Cu(111) the FePc spin is quenched because of stronger electronic coupling with the substrate. Gao *et al.* [162] discovered that the particular adsorption site on the surface may influence the magnetic properties of phthalocyanines. In the light of this discovery, they claim that, on-top configurations of FePc on Au(111) exhibit coupling between the FePc spin and the Au(111) electrons at the Fermi level and, as a consequence, a substantial increase of the Kondo temperature with respect to the bridge configuration is observed. The magnetic properties of the substrate also can have an impact on the magnetic properties of the molecular adsorbates. For porphyrin molecules (which are closely related to phthalocyanines) magnetic ordering was reported on ferromagnetic Co or Ni thin films substrates. The spin of iron and manganese porphyrins was found to couple ferromagnetically[6] with the Co and Ni substrates [163,164], while antiferromagnetic coupling[7] was reported [165] for the same system, but in the presence of half a monolayer of atomic oxygen in between the substrate and the porphyrin layer.

Axial ligand attachment to phthalocyanines is also an important parameter to be considered when trying to control the molecule-substrate coupling or the local spin on the central metal of phthalocyanines. An important part of the studies presented in this thesis deals with magnetic properties changes in phthalocyanine molecules as a consequence of increasing the coordination on the metal by ligand adsorption. The first to claim by spectroscopic techniques that ligand attachment to the metallic centre of a phthalocyanine might influence the spin state on the metal were Kawai *et al.* in 1976. Quedraogo et. al [158] also published a study in 1980 showing, among other findings, that the type of ligand and the coordination number on the metal atom can influence the magnetic properties of the complex. We were able to provide a detailed study on this issue [Papers II-VII], and have shown how the spin state of FePc, as well as the FePc/substrate coupling can be tuned by adsorption of different ligand molecules.

4.1.2. Ligands Used for Adsorption on FePc Films

For studying the adsorption of molecules on FePc films, two different categories of ligands were chosen based on the type of bonds they are expected to from with metals. The first category includes ammonia and pyridine which function as electron donors, and the second category includes carbon monoxide and nitric oxide known to form synergic bonds with metals in which they function both as electron donors and acceptors. In the following,

[6] Ferromagnetic ordering refers to parallel alignment of the spins (in this particular case the spin on the adsorbate with respect to the spins of the ferromagnetic substrate).
[7] Antiferromagnetic ordering instead refers to antiparallel alignment of the spins.

some representative aspects related to the ligands structure, chemical reactivity, and properties will be discussed.

Ammonia

Ammonia (NH_3) (Figure 4.3(a)) is a molecule with a trigonal pyramidal shape. The N atom is in the centre and the corners are occupied by H atoms. The N-H bonds are formed between sp^3 hybridised[8] valence orbitals of N and 1*s* orbitals of H. The HNH angle is 107.8º.

A molecular orbital picture[9] of the NH_3 molecule is shown in Figure 4.3(b). The molecular orbitals result from a combination of the 2*s* and 2*p* atomic orbitals of N and 1*s* atomic orbitals of the three H atoms [79,90]. The highest occupied molecular orbital (HOMO) is a lone pair orbital[10] localised on the nitrogen atom (it is formed by a combination of 2*s* and 2*p* orbitals on the N). The lone pair is a non bonding orbital[11]. The other occupied orbitals are bonding orbitals[12], each of them having a corresponding antibonding orbital[13]. All antibonding orbitals of NH_3 are unoccupied.

[8] Hybridisation is a qualitative description of chemical bonding in the frame of the valence band theory. The concept refers to mixing of the valence atomic orbitals on the same atom to form hybrid orbitals. The hybrid orbitals on each individual atom are then used to build localised molecular orbitals. The theory is very useful for describing the geometry of the molecules and the bond angles. In particular sp^3 hybridisation involves mixing of one *s* and three *p* orbitals resulting in sp^3 hybrid orbitals. In an analogous way *sp* and sp^2 hybridisation can be described [90].
It has to be mentioned that in electron spectroscopy literature the term "hybridisation" is sometimes used for describing mixing of the orbitals between different atoms.

[9] Molecular orbital theory is an alternative model for describing the chemical bonding in a molecule by interaction between the atomic orbitals in a delocalized way. In this picture, the molecular orbitals are delocalised over the whole molecule and are pictured as linear combinations of atomic orbitals. It gives a more quantitative and accurate description of the bonding as opposed to the hybridization theory. However, no single theory can be used to explain all the molecular properties [90]. Molecular orbital theory is very useful for explaining the reactivity of molecules.

[10] A lone pair orbital is defined as an unshared pair of valence electrons that does not contribute directly to the chemical bonding [90].

[11] Non bonding molecular orbital - is an orbital that does not participate in the chemical bonds. Its occupation by electrons, in consequence does not affect the bond order. The term is equivalent with lone pair orbital.

[12] Bonding molecular orbital - is an orbital directly involved in the chemical bond and formed by constructive interference between atomic orbitals. When occupied with electrons, it lowers the energy of a molecule compared to the free atoms [90].

[13] Antibonding molecular orbital - is an orbital which, when occupied with electrons, increases the energy of the molecule compared to the free atoms, leading to destabilisation of the molecule.

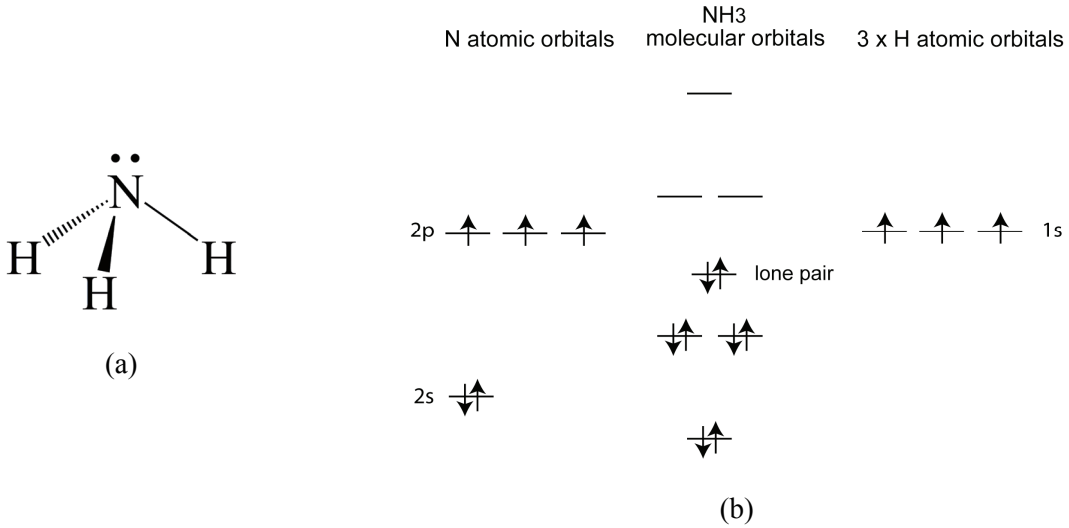

Figure 4.3. (a) Molecular structure of the NH_3 molecule and (b) a schematic representation of the molecular orbital energy levels of the NH_3 molecule [79,90] (not to scale).

Ammonia is a common reagent and ligand in organic chemistry. Because of the lone pair orbital, it acts as an electron donor molecule in transition metal complexes (see Paper III), where it coordinates to the metal atom. Ammonia contributes to the nutritional needs of plants and is commonly used as precursor in fertilizers and pharmaceuticals [166]. Ammonia is also a molecule that quite commonly forms strong hydrogen bonds [90,167]. It can function as either hydrogen bond acceptor through the lone pair orbital or hydrogen bond donor through the hydrogen atoms. This property of ammonia to form hydrogen bonds is also enlightened in Paper III of this thesis dealing with the study of ammonia adsorption on FePc. There, the possibility of intermolecular hydrogen bond formation between the ammonia molecules adsorbed on the FePc macrocycle and resulting in the formation of small ammonia clusters is discussed.

Pyridine

Pyridine (Py) (Figure 4.4(a)) is an aromatic molecule. The carbon and nitrogen atoms in Py are sp^2 hybridised. The sp^2 orbitals combine to form the σ C-C, C-N and C-H bonds that lie in the plane of the ring. The remaining single occupied *p* orbitals, which are perpendicular to the plane of the ring (Figure 4.4(b)), overlap to form the delocalised π electron cloud (double bonds C=C and C=N). Like the NH_3 molecule, the N atom in Py has a lone pair orbital. The lone pair is not involved in the delocalized π system [168,169] and lies in the plane of the aromatic ring, perpendicular to the π system.

In a molecular orbital picture Figure 4.4(c) the highest occupied electronic states in pyridine [170] are composed of the six aromatic π electrons localised in bonding molecular

orbitals and the two lone pair electrons in the non bonding highest occupied molecular orbital.

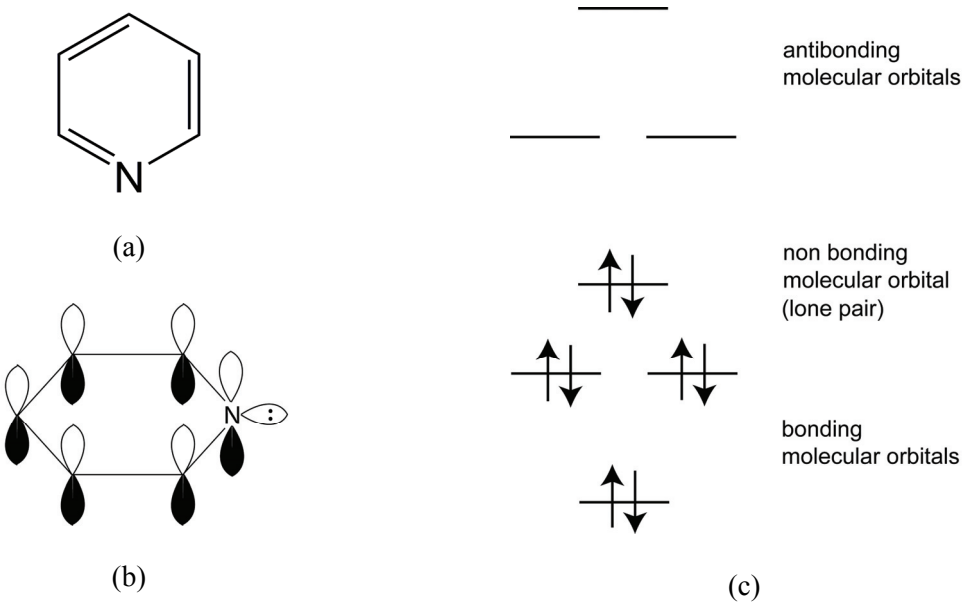

Figure 4.4. (a) Molecular structure of pyridine (C_5H_5N), (b) illustration of the geometry of the molecule, with the nitrogen lone pair orbital in the plane of the aromatic ring and the *p* orbitals perpendicular to the ring, and (c) schematic representation of the distribution π electrons in pyridine [170] (not to scale).

Pyridine is an important chemical reagent (a common ligand in coordination chemistry) and solvent, and is also used as precursor to agrochemicals and pharmaceuticals. The nitrogen atom represents the rich electron density side of the pyridine molecule because of its increased electronegativity with respect to the carbon atoms and because of the lone pair orbital localised on the nitrogen. This makes the nitrogen and in consequence the Py molecule atom a good electron donor.

Carbon Monoxide

Carbon monoxide (CO) (Figure 4.5(a)) is a linear compound, formed by a triple bond between the carbon and oxygen atoms. The 2*s* and 2*p* orbitals on the C combine with the 2*s* and 2*p* orbitals on the oxygen (Figure 4.5(b)) to give the σ and π molecular orbitals[14] of the CO molecule. Two of the bonds have π character and one has σ character. In total, ten valence electrons combine to give rise to the CO molecule.

[14] A bond is σ in nature when the electronic density lies along the internuclear axis of the atoms involved [171]. The orbitals involved have some degree of *s* character. They are the strongest covalent bonds. In π bonds instead, the electronic density lies off the internuclear axis of the atoms involved in the bond. π bonds are more delocalised than the σ bonds and because of less orbital overlap they are weaker than σ bonds. They most commomly have *p* character, but also *d* character can be encountered.

The HOMO of the CO molecule is a lone pair orbital with σ symmetry, localised on the C atom [79,90]. The antibonding lowest unoccupied molecular orbital[15] (LUMO) with π symmetry, has also predominantly C character (C 2*p*). The HOMO and LUMO orbitals in CO are important because both are usually involved in chemical bonds when CO is adsorbed on metal surfaces [172-174] or when it functions as a ligand in transition metal complexes [171,175]. Although oxygen is more electronegative than carbon, in the special case of the CO molecule the negative side of the dipole is at the carbon atom, mostly because the HOMO lone pair orbital is localised on the C atom [90]. For this reason, it is the carbon atom that is commonly the reactive part of the CO molecule.

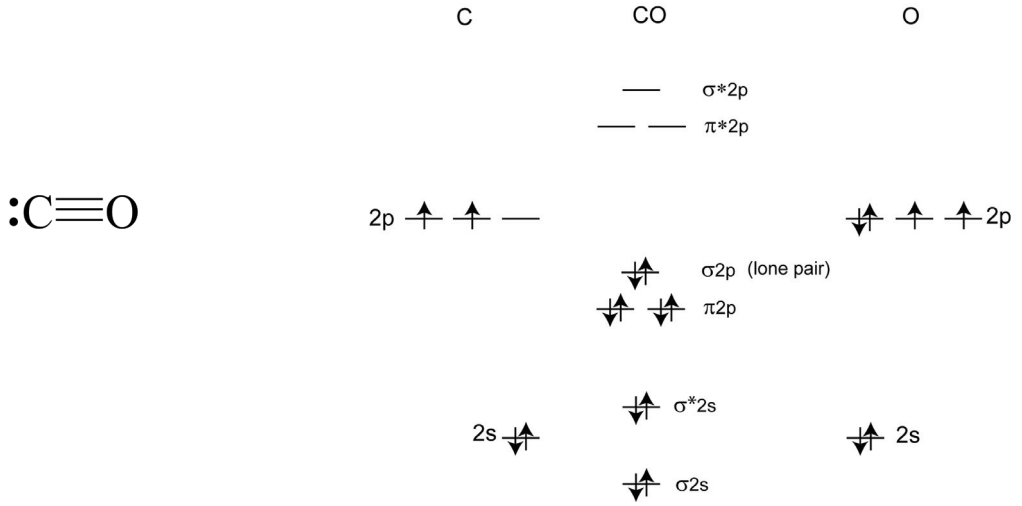

Figure 4.5. (a) Molecular structure of the CO molecule and (b) schematic representation of the molecular orbital energy levels for the CO molecule [79] (not to scale). The σ and π notations refer to bonding and nonbonding orbitals, while σ^* and π^* notations are used to denote the antibonding molecular orbitals.

Carbon monoxide is a highly toxic gas, produced from partial oxidation of carbon containing compounds, such as fuels, for example. It is a major pollution agent in the atmosphere. Its acute toxicity stems from the fact that it irreversibly binds to the iron contained in the heme cofactor of the red blood cells [175], making the haemoglobin loose its oxygen carrying capacity. At laboratory scale, it is a common ligand in coordination complexes.

Going back to the type of bonds that CO forms with metals, it can be said that this is a unique type of bond, first explained by Blyholder [172]. The bond involves direct electron donation of the lone pair electrons from the HOMO σ orbital of CO to the metal, together with back-donation from the metal *d* states with appropriate symmetry into the antibonding π^* orbitals of CO [171,172,175] (Figure 4.6). The CO-Metal bond has σ character and the

[15] The lowest unoccupied molecular orbital is the first orbital after HOMO, and, as the name suggests it is the lowest energy orbital which is not populated by electrons [90].

Metal-CO back donation is a π bond. For this reason the CO molecule is called σ donor and π acceptor molecule. Apart from symmetry considerations, in order for back-donation to occur, it is also necessary that the energy of the LUMO orbital of CO is lower than the metal *d* orbital energy from which the back-donation takes place.

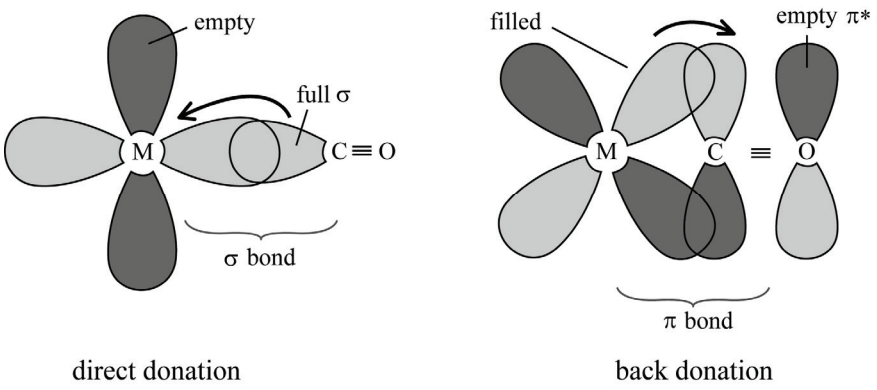

Figure 4.6. Schematics of the Metal-CO bond formation in metal-carbonyl complexes; both direct electron donation from the CO to the metal and back-donation from the metal to the CO molecule are involved.

Nitric Oxide

Nitric oxide (NO) (Figure 4.7(a)) is a very reactive molecule due to the fact that it is a free radical species. As in the CO molecule, the N and O atoms are held together by a triple bond. The molecule contains 11 valence electrons. The molecular orbital structure [176,177] (Figure 4.7(b)) is very similar to that of CO, with the difference that the NO molecule contains an extra electron in the LUMO antibonding orbital. This unpaired electron is localized on the N atom, making it the most reactive part of the molecule.

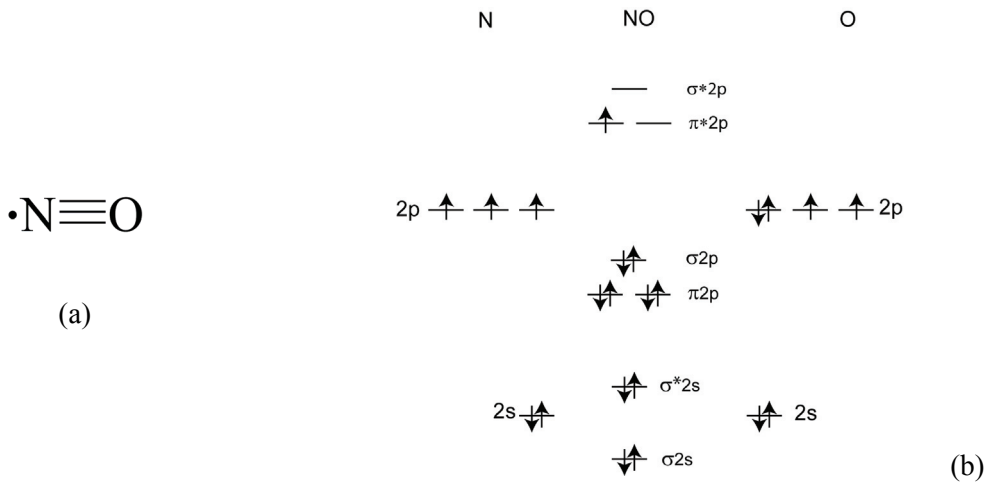

Figure 4.7. (a) Molecular structure of the NO molecule and (b) the schematic representation of the molecular orbital energy levels for the NO molecule [172,177] (not to scale). The σ and π notations refer to bonding and nonbonding orbitals, while σ^* and π^* notations are used to denote the antibonding molecular orbitals.

NO is one of the most common biologically active molecules in mammals. It is a very important signalling molecule [177] in many physiological processes in the human body. It functions as neurotransmitter, cytoprotective molecule, regulator of cardiovascular function among others, and is one of the smallest biologically active molecules. Many of the common biological reactions of NO involve haem-containing proteins, where NO reacts with the metal to form nitrosyl complexes. In the atmosphere NO is an air pollutant produced in car engines, cigarette smoke and power plants.

The NO-Metal bond in nitrosyl complexes has covalent character and is similar to the CO-Metal bond, with direct donation from the single occupied LUMO π^* orbital of the NO to the metal and back-donation from the metal to the NO LUMO orbitals with π symmetry [90,177,178]. Since both the direct and back-donation involve orbitals of π symmetry, NO functions as π donor and π acceptor molecule. Two geometries are commonly encountered in metal-nitrosyl complexes, a linear geometry characterised by a Me-N-O angle of 180° and a bent geometry characterized by angles usually in between 120-145° [177-181]. The Me-N-O angle of specific orbital interactions is a function of the total number of electrons (n), which is the sum of d metal electrons and π^* electrons from the NO molecule. It was found [177,178] that when $n \leq 6$ linear complexes are formed, while $n \geq 7$ favours the bent geometry. It seems that for complexes with $n \leq 6$ the valence electrons occupy bonding and non-bonding molecular orbitals of the newly formed complex, allowing maximum overlap between the metal and NO states, resulting in the linear geometry. For electron configurations with $n \geq 7$, the electrons start populating antibonding states of the complex, inducing destabilization of the system. The bending occurs to weaken the metal-NO overlap and thereby to minimize the destabilisation effects. Such is the case presented in Paper V for NO adsorption on FePc (n=7 in this case) where DFT calculations show that the bent NO geometry is favoured.

4.1.3. Ligands Used for Adsorption on Surfaces

Oxalic Acid

Oxalic acid (HOOC-COOH or $C_2H_2O_4$) (see Figure 4.8 for the molecular structure) is a dicarboxylic acid. In its anhydrous solid state form (in the absence of water, because it usually exists as $C_2H_2O_4$*$2H_2O$) hydrogen bonds are formed between the oxalic acid molecules, resulting in two different polymorph forms, one where the hydrogen bonding assembly results in 2D sheet-like structures and the second characterized by 1D chain-like structures [182]. Since it has acidic character, oxalic acid can be deprotonated resulting in the oxalate ions ($C_2O_4^{-2}$). When adsorbed on metal surfaces, carboxylic acids are known to deprotonate at room temperature [183,184-187]. This is the case for oxalic acid on Cu(111) studied in Paper VIII. Depending on the particular acid and surface, there is always a threshold temperature below which the deprotonation does not take place anymore.

(a) (b)

Figure 4.8. The molecular structure of (a) the oxalic acid molecule and (b) the oxalate ion.

Concerning the present research, the oxalate dianion is of particular importance because it can function as a ligand in transition metal complexes and, as discussed in Paper VIII, on a Cu(111) surface it self-assembles into 2D oxalate networks that have the ability to coordinate iron atoms.

Bi-isonicotinic Acid

Bi-isonicotinic acid (2,2′-bipyridine-4,4′-dicarboxylic acid) (Figure 4.9) is an aromatic molecule, a dicarboxilic acid derived from pyridine. It is formed by connecting two isonicotinic acid molecules through C-C bonds involving the carbon atoms that are closest neighbours to the nitrogen atoms.

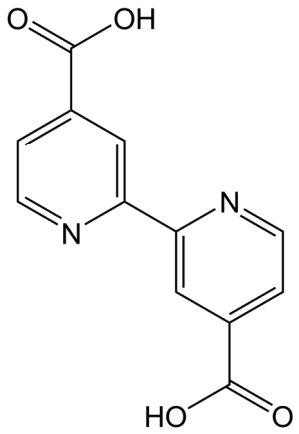

Figure 4.9. The molecular structure of bi-isonicotinic acid molecule.

Bi-isonicotinic acid is a common ligand in organometallic complexes where it can function either as monodentate[16] or bidentate[17] ligand. It is also a ligand of the "N_3" dye used in the construction of DSSCs. The adsorption of bi-isonicotinic acid on surfaces is strongly dependent on the chosen surface. For example on TiO_2(110) bi-isonicotinic acid binds in a deprotonated bidentate fashion through its carboxylic groups[49], which favours the ultrafast

[16] Monodentate ligand is a ligand that binds to a metal by one of its functional groups.
[17] Bidentate ligand is a ligand that binds to a metal by two functional groups. Since the bi-isonicotinic acid molecule has two functional carboxylic groups, it can in principle participate in bonding by both or only one of the groups.

charge transfer from the ligand to the TiO_2 surface [50]. On Au(111) instead [Paper IX], bi-isonicotinic acid binds in its protonated form and no charge transfer is observed from the molecular adsorbate to the Au(111) surface.

4.1.4. Molecular Growth Modes

Understanding the molecular growth of adsorbates on surfaces and the factors influencing it is important, because the growth affects the electrical properties of the films and in consequence affects the possible devices based on such films. The growth of molecular films in general and of phthalocyanine films in particular is a complex process, influenced by a number of factors such as the nature, morphology, and temperature of the substrate, the metallic centre of the phthalocyanine molecule, possible additional side groups on the molecule, and the size of the adsorbate unit cell compared to that of the substrate. All these factors combined will determine the relative strength of the molecule-substrate *vs.* molecule-molecule interaction, which directly affects the growth mode. According to Bauer [188] the growth of molecular thin films obtained by sublimation can follow three different paths (Figure 4.10): the Volmer-Weber growth mode (VW, 3D clusters), Frank-van der Merwe growth mode (FM, layer-by-layer growth), and Stranski-Krastanov growth mode (SK, one or a couple of complete layers followed by 3D clusters).

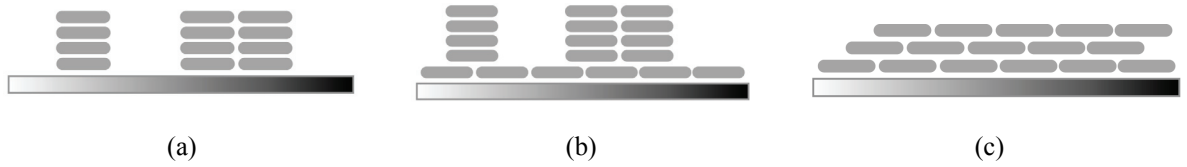

(a) (b) (c)

Figure 4.10. Schematics of the molecular growth modes for thin films deposited by sublimation [188]; (a) Volmer-Weber, (b) Stranski-Krastanov, and (c) Frank-van der Merwe growth.

According to Bauer and Argile [188,189], the different growth modes can be explained thermodynamically by making use of surface energy considerations. According to thermodynamic criteria, a high free energy of the surface compared to that of the adsorbate leads to wetting layer-by-layer (FM) or one-layer plus 3D clusters (SK) growth, while a low free energy of the surface compared to that of the adsorbate results in the 3D cluster growth. It is not straightforward to predict an exact border between the FM or SK growth modes. The SK mode is characterised by a higher mobility of the adsorbates on the surface than on the adsorbate itself and this leads to the formation of a complete first layer.

Graphite is a substrate known to have a low surface free energy. As demonstrated by previous STM work [190] the growth of FePc on graphite follows the 3D cluster growth

pattern. For Au(111), in contrast, our STM experiments show that the first layer is completed before further growth.

In the solid state, phthalocyanines predominantly adopt one of two crystal structures: the so-called α- and β-forms [191-194]. The main difference between the two structures is the angle φ between the normal to the molecular axis and the stacking direction of the central metal atoms (Figure 4.11). The φ angle is 26.5° for the α-form and 45.8° for the β-form. The β-form is more stable. The α-form can be transformed into the β-form by annealing [192]. Also, the growth is influenced by the size of the crystallites [194]; below a certain size α-form growth is favoured and above that size the α-form transforms into β-like crystallites.

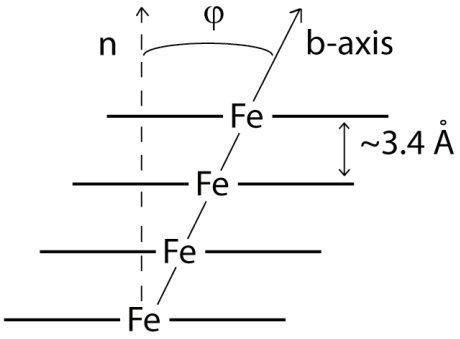

α-form: φ=26.5°, $dist_{Fe-Fe}$=3.79Å

β-form: φ=45.8°, $dist_{Fe-Fe}$=4.79Å

Figure 4.11. Schematic illustration of the polymorphic behaviour of FePc (which holds for phthalocyanines in general). The difference between the α- and β- forms [192] mainly consists in a different angle between the normal to the molecular plane (n) and the molecular stacking direction (b-axis).

4.2. Substrates

4.2.1. Highly Oriented Pyrolitic Graphite

The graphite structure consists of planar graphene layers, weakly bound to each other through van der Waals forces. In the graphene layers the carbon atoms form a hexagonal lattice [90,195]. Each atom in the lattice has three neighbours and forms three σ bonds through sp^2 hybridised orbitals and one π bond through overlapping of the remaining *p* orbitals. The π bonds are delocalized over the graphene planes, and they are responsible for the in-plane conductivity of graphite.

Highly oriented pyrolitic graphite (HOPG) is obtained by heating hydrocarbons close to their decomposition temperature (around 3300K) [196]. It is characterized by a higher degree of ordering than ordinary graphite, with an angular spread between the graphene sheets of less than 1°. The graphene layers are perfectly planar in HOPG, while in graphite they can

form microscopic randomly oriented domains, making HOPG a better in-plane electric conductor than ordinary graphite.

The side and on top view of the graphite structure are shown in Figure 4.12. The distance between the nearest carbon atoms is 1.42 Å and the distance between the graphene planes is 3.35 Å. Half of the carbon atoms in each plane is situated directly on top of an atom in the layer below, while the other half is located in the position of the centre of the hexagon from the layer below [90,197,198].

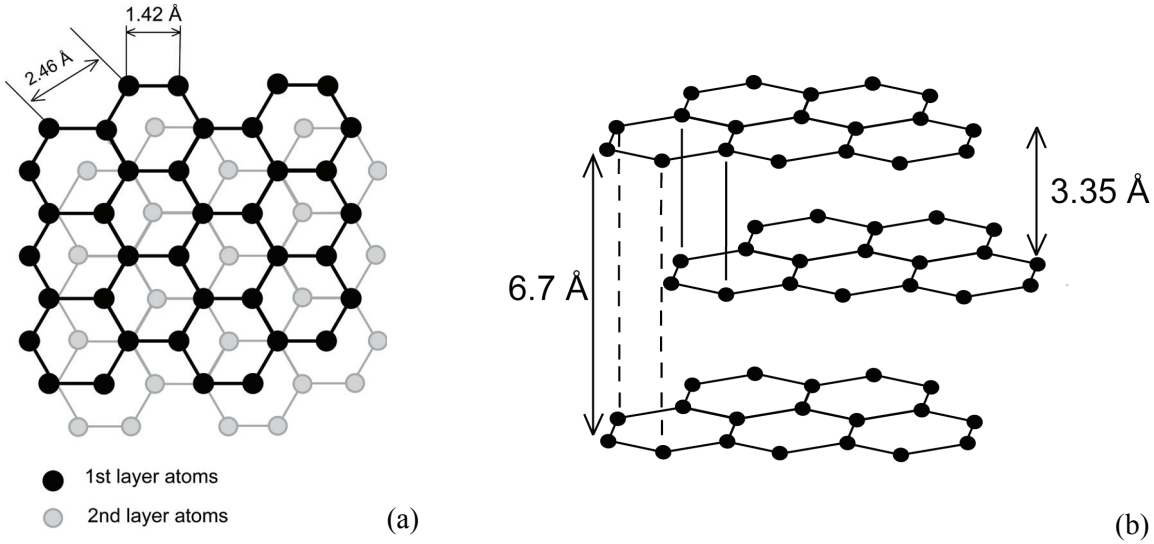

Figure 4.12. Top and side view of the graphite structure [90].

4.2.2. Au(111)

Au(111) has an fcc bulk crystal structure with a lattice constant of 4.08 Å [74]. In vacuum, because of the loss of coordination of the surface atoms, the ideal Au(111) surface undergoes a very particular type of reconstruction in order to minimise the surface free energy. It is the so-called "herringbone" reconstruction. Under the influence of surface stress, the topmost layer of gold atoms contracts along the $\langle 1\bar{1}0 \rangle$ direction, which results in a $(22\times\sqrt{3})$ unit cell (23 gold surface atoms fit on 22 bulk lattice sites) [199]. The reconstructed surface contains 4% more atoms than the bulk planes. Because of the reconstruction, the Au(111) surface structure consists of alternating fcc (ABC) and hcp (ABA) domains (Figure 4.13) separated by corrugation lines (so-called soliton walls) which appear as brighter regions in STM images [200,201]. The size of the corrugation is 0.15-0.2 Å [199]. The dark rows between the corrugation lines are the fcc and hcp regions. Since the fcc stacking is more energetically favourable, the fcc domains are larger than the hcp regions. The "herringbone" reconstruction has a zig-zag structure, each corner being called an elbow

site. The elbows form 120^{o} angles, the length between two consecutive elbows is around 120-150 Å [200].

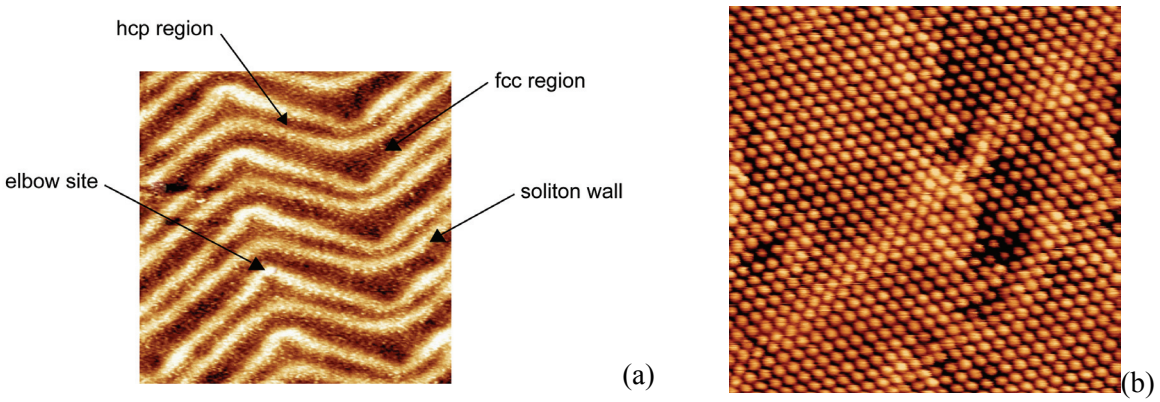

Figure 4.13. (a) STM image of the surface "herringbone" reconstruction of Au(111) and (b) atomic resolution image of the Au(111) surface. The images were taken with the room temperature Omicron STM instrument at the Division of Synchrotron Radiation Research. (a) 300Å×300Å, 0.22 nA, 1.48 V and (b) 100Å×100Å, 0.25 nA, -0.013 V.

4.2.3. Cu(111)

Cu(111) has an fcc bulk crystal structure with a lattice constant of 3.62 Å [74]. Unlike Au(111), the surface of the Cu(111) single crystal does not reconstruct. An atomically resolved STM image of the surface is shown in Figure 4.14.

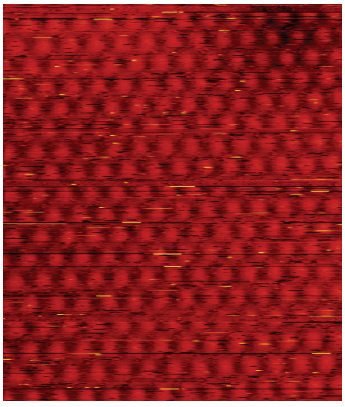

Figure 4.14. Atomically resolved STM imaging of the Cu(111) surface. The image was taken with a low temperature SPECS Århus STM. 33Å×39Å, 0.2 nA, 1 V.

4.3. Interactions Involved in the Systems in Study

The following subchapter aims at giving a brief insight into the types of intramolecular and intermolecular interactions of major importance for the systems involved in the research work presented in this thesis, namely van der Waals, hydrogen bonds and covalent interactions.

4.3.1. Van der Waals Interaction

When two atoms or molecules approach each other, attractions and repulsions between their electrons and nuclei create temporary induced dipoles that lead to intermolecular attractions [74,90,175], called van der Waals interactions or dispersion forces. The name comes from the Dutch physicist Johannes Diederik van der Waals, who postulated the interaction in 1873, and who later, in 1910, was awarded the Nobel Prize in Physics [176]. Van der Waals interactions are weak interactions (1-4 kcal/mol), characterized by bond distances usually >3 Å [203], being the only attractive intermolecular interaction at large distances. Even if van der Waals forces are weak interactions, they are important in condensed matter physics, surface science, nanotechnology, biology, supramolecular chemistry. For example, van der Waals interactions are the main attractive force between non-polar molecules such as N_2, O_2, CH_4, C_6H_6, I_2, Br_2, and they are also present in noble gas molecules, as the force that keeps them together in liquid form [175]. One specific example of van der Waals interactions from the field of surface science is discussed in detail in Paper I of this thesis, where it was shown that the growth of FePc mono- and multilayers on the HOPG surface is characterized by van der Waals molecule-substrate and interlayer FePc-FePc interactions.

4.3.2. Hydrogen Bond

According to the international union of pure and applied chemistry (IUPAC) [204], the hydrogen bond is a "form of association between an electronegative atom and a hydrogen atom attached to a second, relatively electronegative atom" (A-H···B type interactions). More precisely, it is an interaction between the proton of the A-H molecule and a lone pair orbital on the B molecule. The molecule containing the H atom (A-H molecule) is called hydrogen bond donor and the electronegative atom (B) is called hydrogen bond acceptor. Hydrogen bonds are essential and ubiquitous interactions in living organisms. For example, it is hydrogen bonds that keep together the double helix structure of DNA [167]. Also, the water molecules, so essential for life, are held together by hydrogen bonds. Hydrogen bonds are also often encountered in surface science, for example as the driving force of molecular self-assembly at surfaces [205-210]. Paper I of the thesis presents a very likely possibility of FePc molecules being connected through weak hydrogen bonds on a HOPG surface. Also in Paper III, adsorption of NH_3 on FePc most likely leads to hydrogen bond formation between the ammonia molecules, but also possibly between NH_3 and the isoindole units or the bridging nitrogens on the FePc.

Hydrogen bonds are characterized by energies in the range 1-40 kcal/mol and can be subdivided according to their strength. Strong hydrogen bonds usually have 15-40 kcal/mol, moderate bonds have 4-15 kcal/mol, and weak bonds have 1-4 kcal/mol. Typical H···B

lengths are in the range of 1.2-3.2 Å [167], with the shortest distances characteristic for the strongest bonds. The electronegative atoms most often encountered in hydrogen bonds include O, S, N, F, Cl, F [167,211]. Recent research indicates that C-H groups [211] and π electrons [212-217] (in compounds such as acethylene, benzene, pyridine, pyrrole, phenol among many others) can also be involved in weak hydrogen bonds. Hydrogen bonding is a complex interaction, with mixed contribution from electrostatic interactions, dispersion forces and covalent type interactions [211]. Strong hydrogen bonds have mainly covalent character, while weak hydrogen bonds mainly consist of dispersion interactions. It is not straightforward to distinguish between weak hydrogen bonds and van der Waals interactions, because they have similar strengths, so the separation between then comes mainly from theoretical considerations.

4.3.3. Covalent Bond

The covalent bond is a chemical interaction characterized by sharing of an electron pair between the atoms involved in the chemical bond [90,204]. One condition for covalent bond formation is that the atoms involved have relatively similar electronegativity. In a covalent bond, the electronic density can be homogeneously distributed between the atoms if they have the same electronegativity (H_2, O_2, Cl_2, N_2), or, alternatively, when there is a difference in electronegativity, the electron cloud is delocalized towards the more electronegative atom. Typical covalent bond strengths are >40 kcal/mol and bond lengths are commonly between 0.74-2 Å, with the shortest [90] distance characteristic for the hydrogen molecule. Most organic compounds (alkanes, alkenes, ketones, aromatics, amines, alcohols), as well as many gases that are be present in the atmosphere (H_2O, CO, CO_2, NO_2, CH_4, SO_2) and many vital compounds in the human body (proteins, DNA) contain covalent bonds.

The coordinate bond (or dative bond) is a particular type of covalent interaction, where the shared electron pair originates from only one of the species involved in the bond, which serves as a donor, while the other species purely functions as acceptor [204]. Compared to conventional covalent bonds, coordinate bonds are weaker interactions and the bond lengths are longer.

In FePc, for example, all C-N, C-H and C-C bonds are covalent, two of the Fe-N bonds are covalent and two are coordinate. Also, as described in Paper III, adsorption of FePc on Au(111) results in covalent type interactions between Au surface atoms and the Fe atom of FePc. Adsorption of NH3 and Py (Papers III, IV, VI) on FePc results in coordinate Fe-Ligand bonds with the ligand sharing its lone pair electrons with the Fe atom, while NO adsorption on the other hand leads to covalent Fe-NO bonds (Papers V, VII).

CHAPTER 5

Results

5.1. Iron Phthalocyanine on HOPG and Au(111). Electronic Structure and Adsorbate-Substrate Interactions

The following chapter provides an overview of the adsorption behaviour of FePc on HOPG and Au(111) surfaces. It will be shown that the FePc molecules are weakly bound to the HOPG surface (van der Waals interactions), while on Au(111) the molecule-substrate coupling is stronger and the interaction has covalent character. The characteristic C 1*s*, N 1*s*, and Fe 2*p* photoemission lines will also be discussed, together with a very brief comparison to literature data of significance for the work included in the present thesis.

On both substrates and at both mono- and multilayer coverage, FePc forms well-ordered structures, with the FePc plane oriented parallel with respect to the surface (Papers I, III, VI). The C 1*s* and N 1*s* photoemission lines esentially show the same peak components on both substrates and when increasing the coverage from mono- to thick multilayers. These results are also consistent with data reported in literature [150,218-223].

The C 1*s* spectra of the FePc adsorbates show four peak components (Figure 5.1). The lowest binding energy and most intense peak (labelled C=C) results from photoemission from the 24 carbon atoms forming the benzene rings. On the high binding energy side of the C 1*s* benzene peak, the peak labelled C=N represents the contribution from the eight pyrrole carbon atoms. Irrespective of the substrate and coverage, at approximately +1.8 eV from the main C=C line and +2 eV from the C=N line, shake-up satellites are seen (labelled $S_{C=C}$ and $S_{C=N}$, respectively) [219,224,225]. The shake-ups are created as a consequence of multiple final state π-π^* excitations associated with the photoemission from the chemically inequivalent benzene and pyrrole carbon atoms. The spectrum taken on HOPG contains an extra contribution hidden under the low binding energy peak (Paper I) which is due to photoemission from the substrate carbon atoms. Table 5.1 reports a number of representative peak positions and peak separations for FePc on HOPG and Au(111). The peak separations fit with previously reported literature data for phthalocyanines on surfaces

[150,219,220,222,226], as well as gas phase phthalocyanines [227]. The main peak – satellite separation is essentially the same at monolayer and multilayer coverage and also very close in value on both substrates. The intensity ratio between the C=C and C=N peaks, as given by the results of the fits varies between 3:1 and 3.17:1 for the cases discussed here, which fits with the 3:1 value expected from the stoichiometry of the compound.

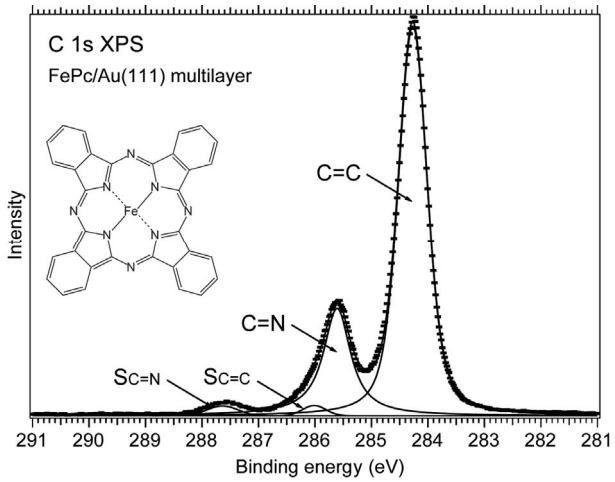

Figure 5.1. C 1*s* photoemission spectrum (experimental data and fit) for multilayer FePc on Au(111). The spectrum contains four peak components. The peaks labelled C=C and C=N correspond to photoemission from the chemically inequivalent benzene and pyrrole carbon atoms, and the peaks labelled $S_{C=C}$ and $S_{C=N}$ are shake-up satellites associated with the photoemission from the main C=C and C=N lines.

Table 5.1. Binding energies in eV characteristic for the C 1*s* and N 1*s* photoemission lines of mono- and multilayers of FePc on HOPG and Au(111), as well as the corresponding binding energy shifts between the main lines and the shake-up satellites. The binding energy uncertainty is ±50 meV.

		Monolayer		**Multilayer**	
		HOPG	**Au(111)**	**HOPG**	**Au(111)**
C 1*s*	C=C peak (eV)	284.49	283.82	284.54	284.26
	C=N peak (eV)	285.67	285.12	285.85	285.6
	C=C C=N separation (eV)	1.18	1.30	1.31	1.34
	C=C $S_{C=C}$ separation (eV)	1.80	1.73	1.80	1.74
	C=N $S_{C=N}$ separation (eV)	2.05	2.00	2.11	2.03
N 1*s*	Main peak (eV)	398.73	398.17	398.9	398.62
	Satellite (eV)	1.79	1.64	1.82	1.65

In some studies on PbPc and CuPc reported in literature [133,226-228], the C 1*s* spectra could only be fitted with five peak components. The fifth component is hidden below the C=C peak, 380 meV shifted higher in binding energy. The consensus in this case is that the fifth component is a vibrational C-H peak, also supported by gas phase experiments of Evangelista *et al.* [227]. However, in the present case of FePc on HOPG and Au(111) optimum results were only obtained by using four C 1*s* peak components.

The FePc molecule contains two chemically inequivalent nitrogen species: the pyrrole nitrogens and the nitrogen atoms that bridge together the isoindole units. Their binding energy is separated by only ~0.3 eV [222,226], which makes it impossible to resolve them experimentally. The N 1*s* spectrum (Figure 5.2) therefore contains then one main line only and a corresponding shake-up satellite.

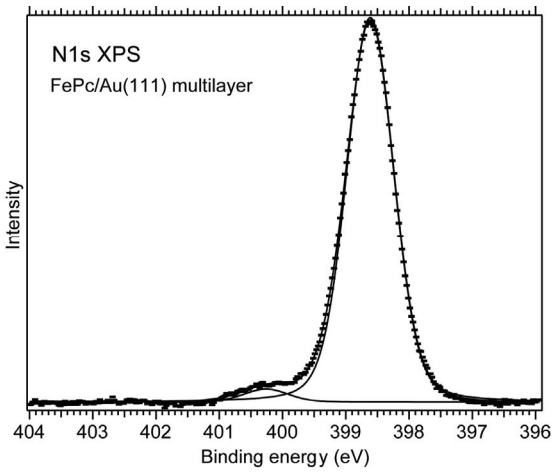

Figure 5.2. N 1*s* photoemission spectrum for a multilayer of FePc on Au(111). The main peak at 398.62 eV is accompanied by a corresponding shake-up satellite on the high binding energy side.

One notable difference between the C 1*s* and N 1*s* photoemission lines on the two substrates is that they show up at lower binding energies on Au(111) surface. Such behaviour is not surprising, since the metallic character of the Au(111) substrate leads to an improved final-state screening of the core hole compared to HOPG.

Figure 5.3 illustrates Fe $2p_{3/2}$ core level spectra for mono- and multilayer preparations of FePc on the two substrates. The Fe 2*p* photoemission line shape gives indirect information on the spin state of the Fe atom in the FePc molecule. In the particular case discussed here, in addition to spin state information, it is possible to obtain important information related to the adsorbate-substrate interaction through a comparison of the Fe 2*p* spectra for the indicated preparations. In all cases, the peaks are very broad. As discussed in section 2.1.6 this broad, multiplet structure of the photoemission Fe 2*p* line is a final state effect, common for elements with unpaired electrons in the *d* valence band. Photoemission spectra of multilayers should be comparable to those of isolated molecules, and indeed both the line shape and the FWHM (~2.7 eV) of multilayer spectra on Au(111) and HOPG are similar, indicating that the substrate plays very little or no influence at all in the photoemission from the multilayers. The monolayer Fe 2*p* spectrum on HOPG has a FWHM of ~1.45 eV. As shown in Paper I this also corresponds to a weakly interacting system where basically the FePc-HOPG coupling is van der Waals type. The monolayer spectrum on Au(111) instead shows the widest Fe $2p_{3/2}$ line of ~3.7 eV FWHM. This is an indication that on Au(111) in addition to multiplet

splitting effects, the Fe 2*p* spectrum is also broadened by the interaction between the FePc adsorbates and the surface. Clearly, the interaction with Au(111) is stronger than the corresponding interaction in weakly interacting systems of FePc such as multi- and monolayers on HOPG and multilayers on Au(111).

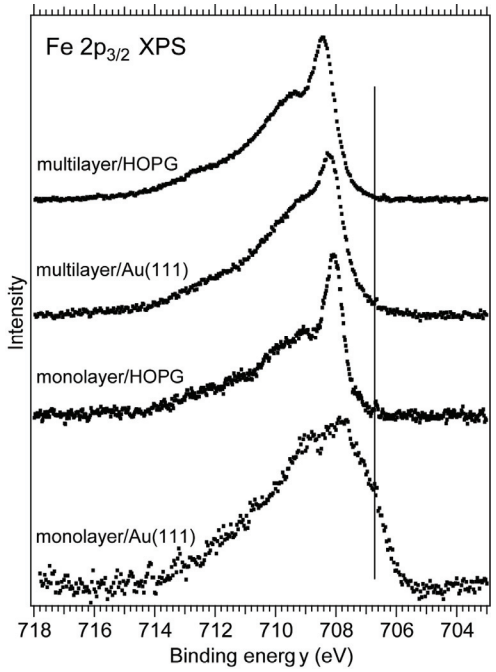

Figure 5.3. Fe $2p_{3/2}$ photoemission spectra for mono- and multilayer preparations of FePc on Au(111) and HOPG. The multilayer spectra are very similar in both cases, while the spectrum of the monolayer/Au(111) is significantly broader compared to monolayer/HOPG and both mono- and multilayer/Au(111). The multilayer/HOPG binding energy scale is not calibrated due to the lack of data, but the rest of the spectra display the correct binding energy scale.

The broadened structure of the monolayer spectrum on Au(111) is mostly evident on the low binding energy side, where an additional shoulder is present at around 706.8 eV (position marked by the continuous line in Figure 5.3). To gain more insight into the origin of the states giving rise to the Fe $2p_{3/2}$ photoemission signal on of the monolayer FePc Au(111), the results of a least square fit performed on the Fe $2p_{3/2}$ spin-orbit component are shown in Figure 5.4. Two main multiplet states (P1 and P2) and a satellite (S) were assigned to the spectrum. The satellite is the broad feature at 710.28 eV. Each multiplet state should be a sum of four different m_j components. The low binding energy state P1 was modelled by one peak (at 706.89 eV), as opposed to the middle state P2 that was modelled by two peaks (at 707.85 and 708.94 eV). These P1 and P2 states are attributed to differently charged components. This would then imply that the low binding energy state is most likely due to charge transfer from the Au(111) surface to the iron atom of FePc. This could be caused by either initial or final state effects. Alternatively, combined initial and final state effects could play a role. The reason for modelling the middle state with two peaks and the low binding energy state with one peak is based on the fact that the charge transfer from the substrate giving rise to the low binding energy state is expected to reduce the valence spin for this particular state, which would imply a reduced splitting between the corresponding m_j components and the thus reduce its representation to a single peak. It has to be mentioned that the above mentioned

high binding energy satellite structure S could in principle also contain contribution from a third differently charged state.

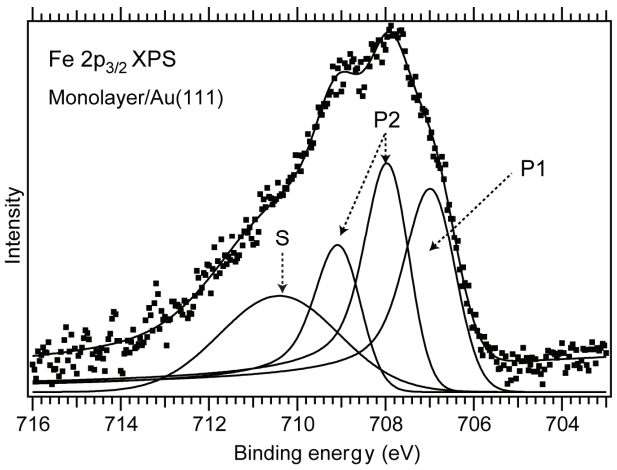

Figure 5.4. Fe $2p_{3/2}$ photoemission spectrum (experimental data and fit) for monolayer FePc on Au(111).

Even if the adsorbate-substrate coupling is stronger on Au(111), the interaction is localised on the iron site and does not affect the delocalised π system containing the carbon and nitrogen atoms, as shown by the C 1*s* and N 1*s* photoelectron spectra (Paper III). There are some studies reported in literature on FePc/TiO_2 [153], CuPc/Al(100) [151], and MgPc/polycristaline Au [229] when the coupling with the substrate was found to be so strong that it affects the whole macrocycle. In those particular cases the C 1*s* and N 1*s* core-levels were also significantly affected by the adsorption. Just to give an example, Palmgren et. al [153] who studied FePc molecules on TiO_2 found a strong coupling of the first layer molecules with the substrate, involving charge transfer from the FePc to TiO_2, which affects the whole molecule. The C 1*s* and N 1*s* show completely different photoemission lines for the first layer compared to subsequent layers and the shake-up structures are completely quenched for photoemission arising from the first layer molecules, which is not the case here.

5.2. Ligand Attachment to FePc Molecules on Au(111)

The experimental work on gas adsorption includes NH_3, Py, CO, NO adsorption on monolayer FePc/Au(111) and NH_3 and NO adsorption on multilayer FePc/Au(111). The adsorption leads to significant changes in the electronic structure of the FePc organometallic network, as will be discussed in the following. First, the adsorption results in the formation of bonds between the iron atom and the ligand molecules (Fe-L bonds). Second, the formation of Fe-L bonds decouples the adsorbates from the substrate and it substantially changes the spin state of the iron atom. Both a lowering of the spin state or a complete spin quench can be obtained, depending on the ligand that is used. The same holds for the strength of the FePc-substrate interaction, which is again strongly dependent on the ligand molecule. The NH_3 and

Py adsorption on FePc monolayer were carried out at around 83 K, while the other experiments were performed at around 20 K.

5.2.1. Tuning the Spin State and the Adsorbate-Substrate Coupling by Ligand Adsorption on Single Layer FePc Molecules

The evolution of the Fe $2p_{3/2}$ photoemission signal with the amount and type of adsorbed gas nicely illustrates the above mentioned changes in spin. In all cases the Fe 2*p* spectra become significantly narrower after gas adsorption. The width decreases with coverage up to a saturation point called "iron saturation coverage". Above saturation any increase in the amount of gas does not affect the Fe 2*p* photoemission signal anymore (see Figure 5.5 for the evolution of Fe $2p_{3/2}$ FWHM with coverage), even if corresponding N 1*s*, O 1*s* and/or C 1*s* spectra clearly show continuous adsorption of gas even beyond this point. The decrease in width of the spectra indicates that at least to a high degree the changes should be due to lowering of the spin as a consequence of ligand adsorption, which would then lead to a decrease of the energy splitting between the m_j components and thus narrower lines.

The "iron saturation coverage" corresponds to the situation where all the iron centres are bound to ligand molecules. Since there are no more available iron centres for bonding above the saturation point, the gas molecules will adsorb at different sites.

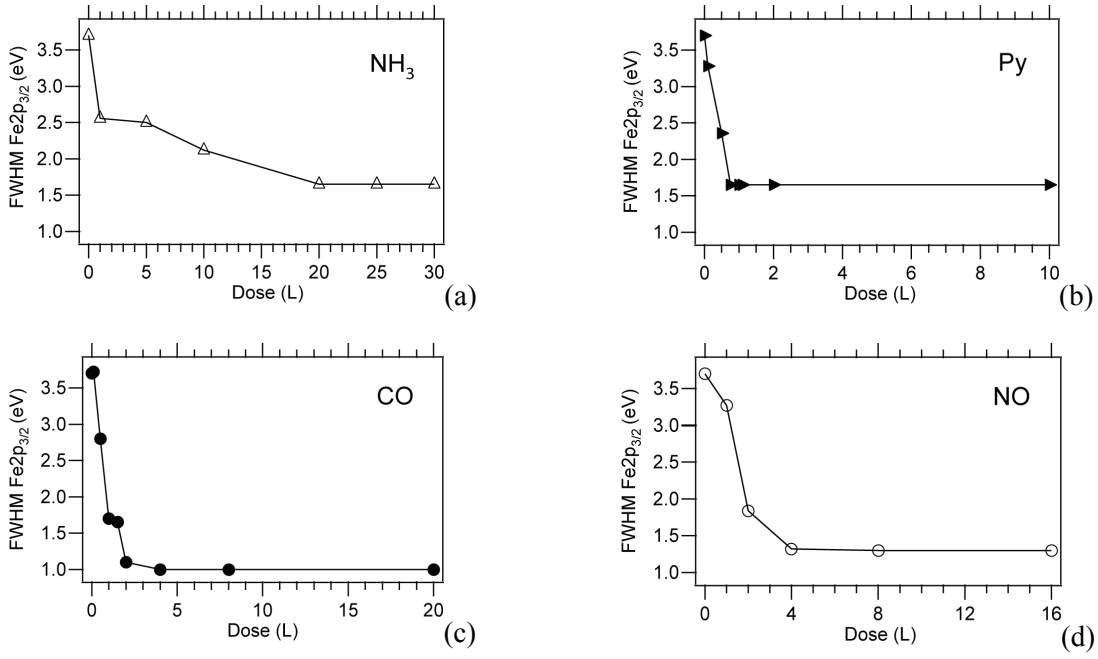

Figure 5.5. Evolution of the FWHM of the Fe $2p_{3/2}$ line as a function of the amount of (a) NH_3, (b) Py, (c) CO and (d) NO dosed on the monolayer FePc/Au(111) sample. A saturation point is reached in all cases and above that point the FWHM remains constant. At saturation all the Fe sites are bound to ligand molecules.

To obtain a more quantitative description of the changes involved in the Fe 2*p* line, the results of the least square fits for the spectra at the saturation coverage are shown in Figure 5.6. Some representative peak parameters are given in Table 5.2. For comparison, the table also contains the values obtained by fitting the monolayer spectrum shown in Chapter 5.1. The spectra contain three peak components for NH_3, Py and CO adsorption, while NO adsorption gives two peaks. In line with the assignments that were made for the Fe 2*p* spectrum of monolayer FePc/Au(111) in Chapter 5.1, the highest binding energy peak (labelled S) at ~710-711 eV is attributed to a satellite and the middle peak (P2) and the lowest binding energy peak (P1) are due to differently charged species. P1 is the peak caused by the adsorbate-substrate coupling and it has the largest intensity for FePc/Au(111). Its intensity is most significantly reduced after CO and NO adsorption, being almost quenched after CO adsorption and completely quenched after NO adsorption. Such behaviour shows that FePc-Au(111) coupling is significantly weakened by the adsorption of gases. The intensity evolution of P1 reveals that NO has the strongest effect on the FePc-Au(111) decoupling, resulting in a complete decoupling of the FePc adsorbates from the substrate. DFT calculations (Paper II, III, IV, V) also support the idea of adsorbate-substrate decoupling as a consequence of the formation of Fe-L bonds with the NH_3, Py, CO and NO molecules.

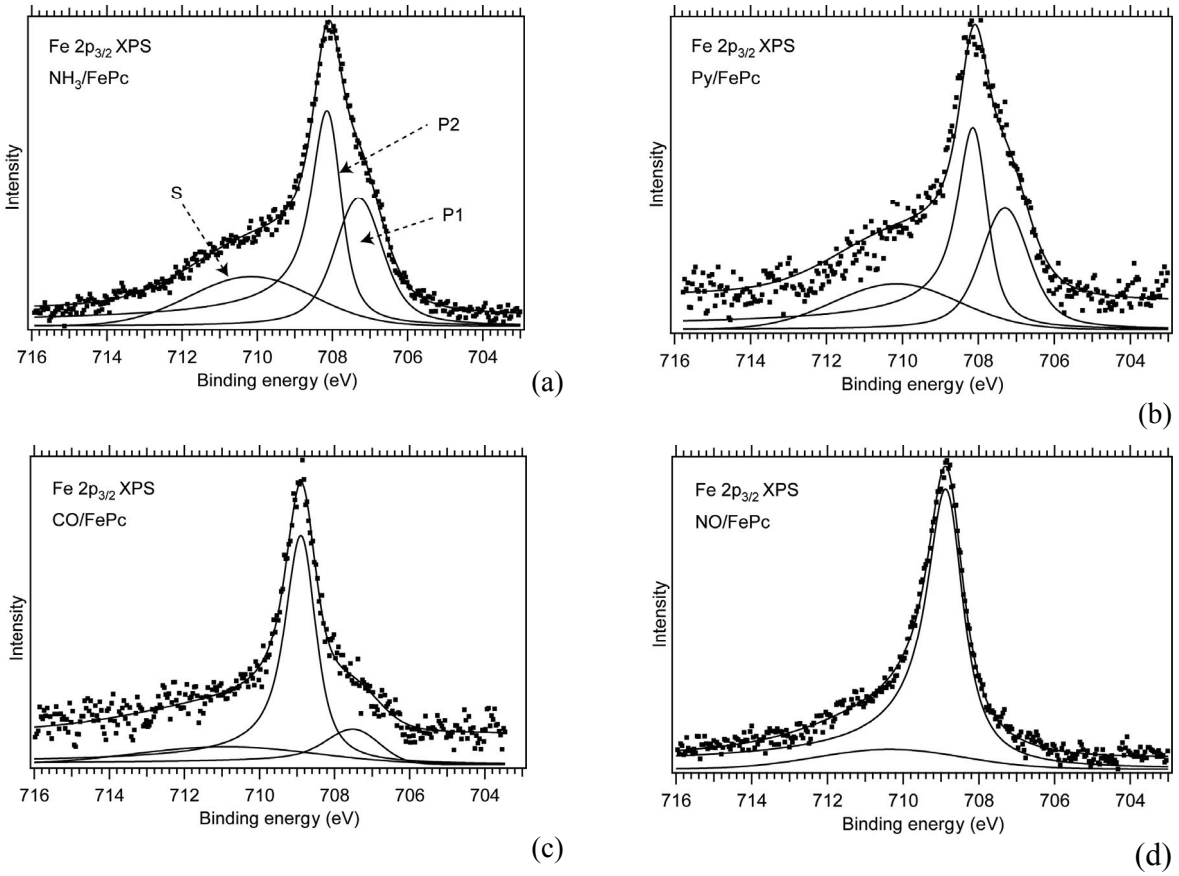

Figure 5.6. Fe $2p_{3/2}$ photoemission spectra (experimental data and fit) at the iron saturation coverage, after adsorbing (a) NH_3, (b) Py, (c) CO, and (d) NO on FePc monolayers on Au(111).

Table 5.2. Representative peak parameters for the low binding energy (P1) and the middle (P2) peaks in the Fe $2p_{3/2}$ spectra before and after adsorbing NH_3, Py, CO and NO on monolayer FePc/Au(111) in amounts corresponding to the iron saturation coverage. The calculated values for the spin magnetic moment are also shown. For the middle P2 state in the monolayer FePc spectrum, because the fit was done by modelling this particular state by 2 components, the BE and FWHM were obtained by considering the sum of the fit components. The uncertainty is ±50 meV, except for the FePc/Au(111) where due to the different procedure adopted for fitting the error is larger ±200 meV.

	P1		P2		
	BE (eV)	Area	BE (eV)	FWHM (eV)	μ_s (μ_B)
FePc/Au(111)	706.89	1.15	708.28	2.29	2.36
NH_3/FePc/Au(111)	707.30	0.80	708.07	1.02	-0.27
Py/FePc/Au(111)	707.30	0.82	708.07	1.02	0.25
CO/FePc/Au(111)	707.35	0.31	708.86	1.01	0.09
NO/FePc/Au(111)	-	-	708.81	1.26	0.84

The FWHM of the middle component (P2) narrows down from ~2.3 eV for monolayer FePc/Au(111) to ~1 eV for the NH_3/FePc/Au(111), Py/FePc/Au(111) and CO/FePc/Au(111). Its narrowing is not so pronounced for NO/FePc/Au(111), when the observed FWHM is ~1.25 eV. The effect is attributed to a partial spin quench caused by NO adsorption and a total spin quench resulted from the NH_3, Py and CO adsorption. The theoretical values for the spin magnetic moments in Table 5.2 are in agreement with the trend given by the experimental data. The spin changes take place because of the redistribution of the *d* states on the Fe in the complex formed after gas adsorption. For NO adsorption, the unpaired electron on the molecule also brings significant contribution to the spin.

Regarding the binding energy of the middle states in the Fe 2*p* spectra, no significant binding energy shift is observed when dosing NH_3 and Py (within the binding energy uncertainty) compared to monolayer FePc. This is not surprising since coordinate bonds are expected to be rather weak interactions. Instead, an ~0.5 eV shift towards higher binding energy is observed for CO/FePc/Au(111) and NO/FePc/Au(111) at saturation, indicating that the Fe-CO and Fe-NO bonds are stronger compared to Fe-NH_3 and Fe-Py bonds. The shift is in accordance to the electron withdrawing nature of the CO and NO ligands and shows that the back- donation from the Fe to the CO and NO ligands is stronger than the direct donation, resulting in decreased electron density on the iron atom compared to FePc.

5.2.2. Spin State Changes by Ligand Adsorption on Multilayer FePc Molecules

NH_3 and NO molecules were adsorbed on multilayers of FePc on Au(111). The NH_3 adsorption produces a narrowing of the Fe $2p_{3/2}$ signal from ~2.7 eV for the multilayer to ~1 eV at the saturation coverage and no binding energy shift is observed (Figure 5.7(a)). Compared to the adsorption on monolayer FePc, the Fe 2*p* spectrum is already narrower, because it does not contain the low binding energy shoulder caused by the interaction with the substrate. The decrease in width in this particular case is fully due to the spin changes

involved by the formation of the Fe-N bonds. Ammonia coordinates to the iron centre of FePc and the coordination induces redistribution of the *d* states of the FePc, resulting in quenching of the molecular spin. An important aspect related to NH_3 adsorption on multilayer FePc is that the shape of the Fe 2*p* spectrum at saturation is a good indication of the fact that the ammonia does not only bind to the topmost layer of FePc molecules, but also binds to the underlying FePc layers, at least to the ones accessible by the photoemission experiment.

NO adsorption occurs in a somewhat different way: it results in two Fe 2*p* species, one at the same binding energy compared to the low binding energy peak of the Fe 2*p* line of the multilayer (~708 eV) and the second shifted to higher binding energy (Figure 5.7(b)). The high binding energy species is assigned to a low spin complex formed by the top layer of FePc molecules interacting with NO, and the low binding energy peak is assigned to underlying layers of FePc that are not interacting with the NO molecules. Since the NH_3 molecules are diffusing in between the FePc layers, it would be expected that the NO molecules have the same behaviour, as their sizes are comparable. However, as shown in Paper VII and as will be briefly discussed in section 5.2.3, the majority of the NO molecules adsorb as dimers, which would then explain their inability to diffuse in between the FePc layers due to steric constraints. A more detailed discussion on this issue can be found in Paper VII.

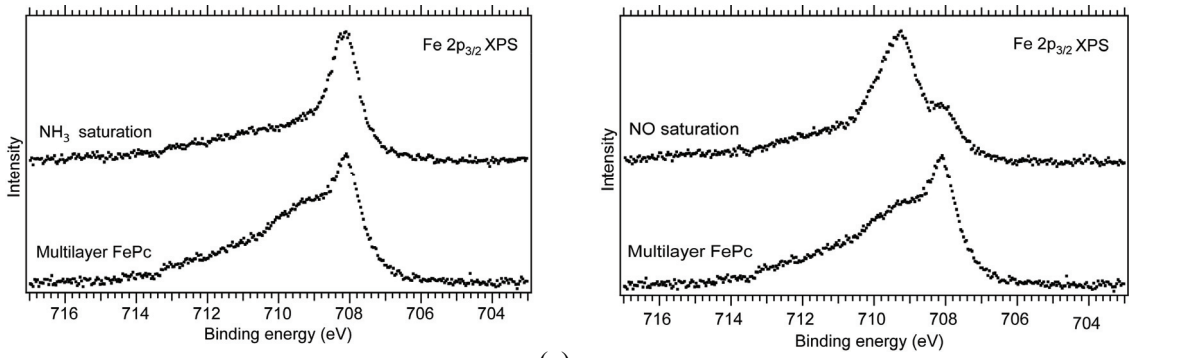

Figure 5.7. Fe $2p_{3/2}$ photoemission spectra before and after adsorbing (a) NH_3 and (b) NO on multilayer FePc/Au(111). The amount of gases adsorbed corresponds to the "iron saturation coverage".

From all the situations discussed above, it is clear that the formation of Fe-Ligand bonds has a significant influence on the spin properties of the FePc adsorbates and on the FePc-substrate coupling. Both properties strongly depend on the type of ligand chosen. This behaviour could be exploited in the future in an attempt to precisely control the spin state of the molecular networks at surfaces, but also for a precise tuning of the adsorbate-substrate coupling.

5.2.3. Adsorption Behaviour of NH_3, Py, CO and NO Ligands. Coordination to Iron and Other Adsorbed Species

Representative N 1*s* and C 1*s* photoemission spectra obtained after adsorbing gases in doses corresponding to the saturation coverage on mono- and multilayer films of FePc are shown in Figure 5.8. Different adsorbed species are present in all cases. The species that induces the spin change is the ligand coordinated to the Fe site (peaks labelled Fe-L, where L = NH_3,Py,CO,NO). Ligand molecules that adsorb either on the macrocycle on different sites than the iron (Pc-L) or on the Au(111) surface (Au-L) are also present.

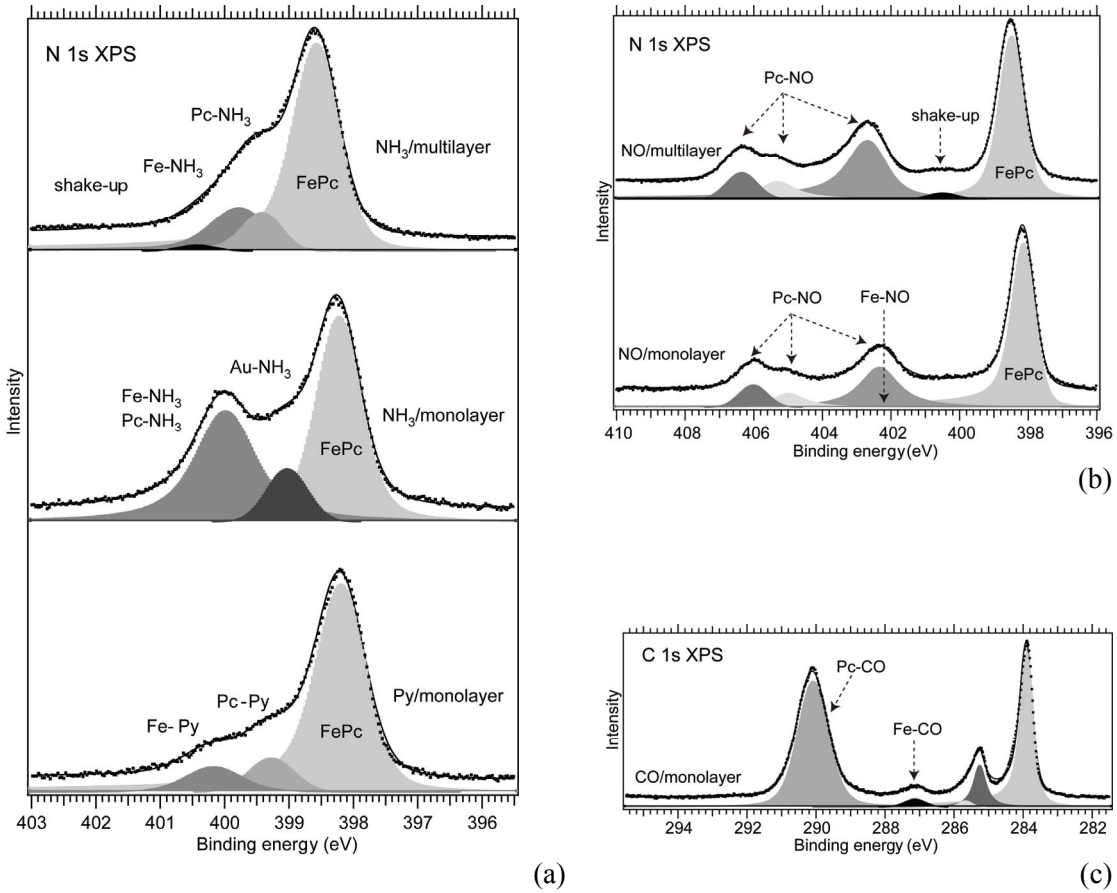

Figure 5.8. N 1*s* and C 1*s* photoemission lines obtained after dosing different gases on FePc mono- and multilayer structures in amounts corresponding to the iron saturation coverage.

Py adsorption on monolayer FePc results in two distinct N 1*s* peaks due to Fe-Py interaction (400.19 eV) and Pc-Py interaction (399.3 eV). The peak at 399.3 eV possibly contains some contribution from Py molecules interacting with the Au(111) surface also. Ammonia adsorption on monolayer FePc shows a somewhat different behaviour. It results in a single N 1*s* peak for both Fe-NH_3 and Pc-NH_3 interaction at 400.02 eV, while another distinct peak at 399.05 eV is attributed to the interaction with the bare Au(111) surface. Moreover calculations show that it is energetically favourable for ammonia to adsorb on Fe as clusters, which is not so surprising when considering the ability of ammonia molecules to

form strong hydrogen bonds. One interesting aspect that can be noted is the higher binding energy (0.17 eV) for the Fe-Py peak compared to the Fe-NH_3 peak obtained for adsorption on monolayer FePc. This could be explained by either a stronger Fe-Py bond compared to the Fe-NH_3 bond, but it could as well be an effect of the formation of hydrogen bonded ammonia clusters on the Fe site, which would increase the electron density on the NH_3 molecule directly bound to the Fe.

Ammonia adsorption on multilayer FePc gives N 1*s* peaks at 399.41 eV caused by Pc-NH_3 interactions and at 399.76 eV caused by Fe-NH_3 interactions. One important aspect that comes out from the comparison of the N 1*s* spectra for NH_3 adsorption on monolayer and multilayer FePc is that the substrate plays an important role in the adsorption process. On multilayer FePc, prior to reaching saturation, the NH_3 molecules occupy the iron sites only. A single N 1*s* species (Fe-NH_3) is present at low doses, while the peak responsible for the interaction with the macrocycle (Pc-NH_3) shows up at and beyond saturation only. NH_3 adsorption on monolayer FePc instead results in both Fe-NH_3 and Pc-NH_3 species being present already from the initial doses of NH_3 and the same holds for Py/monolayer adsorption. This behaviour shows that the Au(111) surface plays an important role in the adsorption process by possibly lowering the adsorption energy for certain sites or by changing the diffusion behaviour of the gas molecules.

If the NH_3 adsorption on monolayer FePc is to a high degree influenced by the presence of the substrate, this seems not to be the case for NO adsorption. Adsorption of NO on mono- and multilayer FePc molecules gives very similar peak shapes (Figure 5.8(b)), with the only difference that they are around 0.4 eV shifted to higher binding energy in the multilayer case, which is attributed to the improved core hole screening provided by the Au(111) substrate to the monolayer molecules. This similarity between the NO adsorption on mono- and multilayer FePc could be due to the fact that, as seen in section 5.2.1, the NO adsorption has the strongest effect on the FePc-Au(111) decoupling. When some coupling to the substrate is present, the Au atoms can be considered to act as point ligands on one side of the macrocycle. After full decoupling, however, this effect would disappear, which explains the insignificance of the substrate in the NO adsorption process.

Three N 1*s* components appear as a consequence of NO adsorption; all are present from very low doses of NO and continue to develop in intensity with increasing amounts of NO. This makes it difficult to assign the peak caused by the Fe-NO interaction. For the adsorption on monolayers it was revealed that annealing the NO/monolayer sample to 171 K results in a low intensity peak at ~402.2 eV, which is assigned to Fe-NO interaction, expected to be the strongest interaction. This basically means that the Fe-NO peak is hidden below the lowest binding energy N 1*s* NO peak. The N 1*s* NO peaks, as well as the corresponding O 1*s* peaks (Papers V, VII) are consistent with previously reported data for the NO dimer. The multiple

peak feature was assigned to different core hole screening mechanisms in the NO dimer [230,231], more precisely a combination between intra-molecular and inter-molecular screening. This clearly indicates that also in the present case at least a significant part of the NO molecules, if not all, are adsorbed as dimers. Because the Fe-NO peak is hidden below the other NO contributions it is not straight forward to say whether NO interaction with Fe takes place in monomer or dimer form. It seems however unlikely that this would happen in the dimer form, because the dimer is formed through the unpaired electrons on the N [232,233] and the bond with Fe would involve the same electrons. Moreover, DFT calculations predict unstable structures for the NO dimer on FePc.

CO adsorption on monolayer FePc gives C 1*s* peaks at 287.15 eV and 290.11 eV (Figure 5.8(c)). The peak at 287.17 eV is attributed to Fe-CO interaction. The peak position coincides with the shake-up satellite of the C 1*s* FePc pyrrole peak, but due to its enhanced intensity after CO adsorption and due to its intensity compared to C 1s FePc peaks it becomes clear that it also contains a contribution from the CO molecules bound to iron. The peak at 290.11 eV is again caused by different CO adsorption sites, but also by second layer CO molecules. Again, as was the case for NH_3, Py and NO adsorption on monolayer FePc, the CO adsorption results in different adsorption sites being occupied even from very low doses of CO.

5.3. Oxalate-Based Coordination Networks on Cu(111)

The self-assembly of oxalate ions on Cu(111) followed by deposition of iron leads to the formation of a honeycomb 2D iron-oxalate coordination network. For the experiments, first a submonolayer of oxalic acid was deposited by sublimation on a Cu(111) surface held at room temperature. The surface mediated deprotonation of the oxalic acid molecules leads to the formation of well ordered oxalate hexagonal islands (Figure 5.9(a)). The islands are formed by flat lying oxalate ions, as shown by the XPS and XAS data (Figure 5.9(b) and (c)). The O 1*s* photoelectron spectra show one peak at 531.4 eV, indicating that the two carboxylic oxygen atoms are equivalent, meaning that full deprotonation of the oxalic acid adsorbates occurs. The angular dependence of the O 1*s* XAS resonances shows a flat orientation of the oxalate network. The π^* resonances (the resonances below ~537 eV) have maximum intensity for grazing incidence (65˚) and minimum intensity for normal incidence (0˚), while the opposite is true for the σ^* resonances (above ~537 eV).

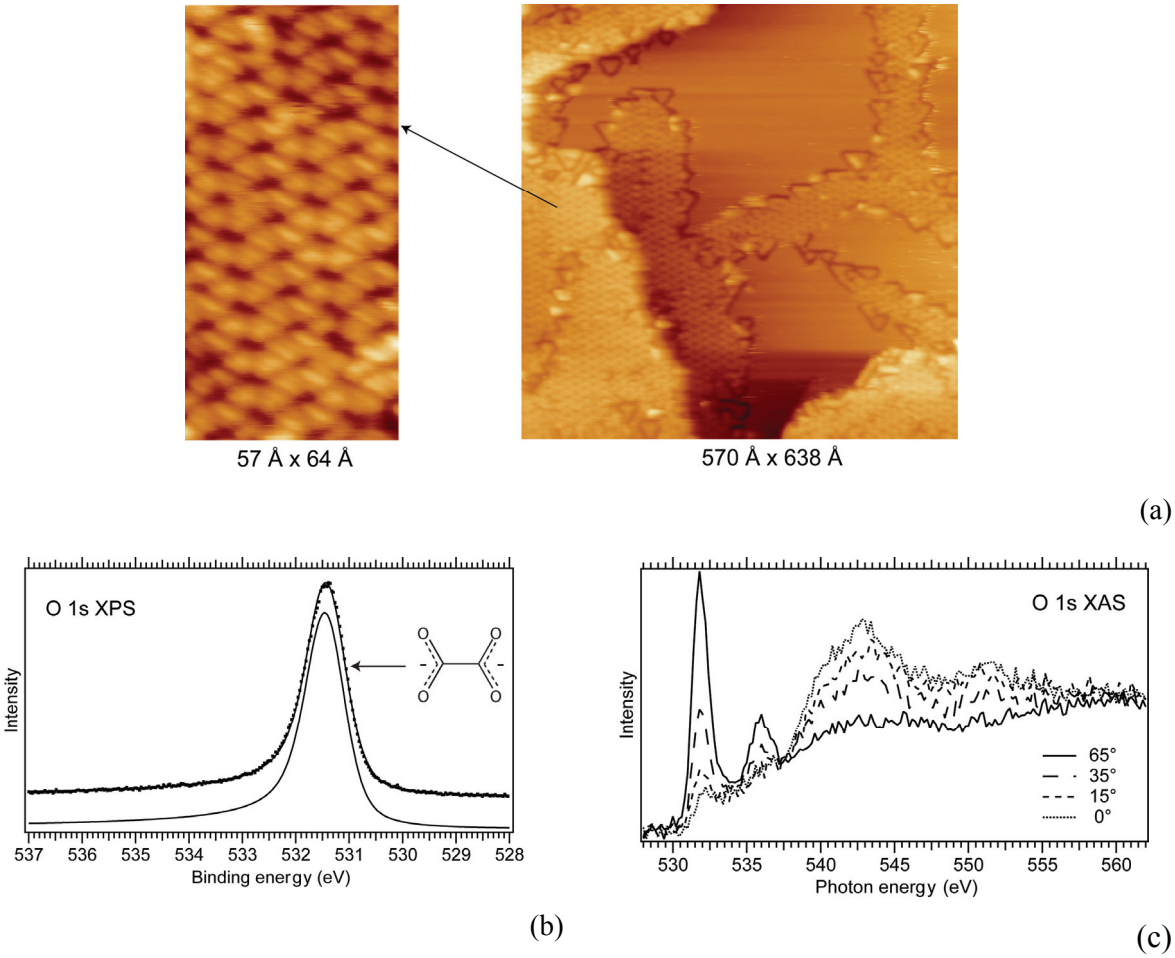

Figure 5.9. (a) Constant current STM image (I=0.2 nA, V=1.2 V) of oxalate islands on Cu(111), (b) O 1*s* XPS signal, and (c) O 1*s* XAS spectra as a function of the light incidence angle with respect to the substrate normal for submonolayer coverages of oxalate on Cu(111).

Subsequent evaporation of Fe atoms followed by annealing to around 100˚C leads to a complete reorganisation of the nanoscale network. The hexagonal islands are replaced by honeycomb like patches (Figure 5.10(a)). This reorganization is attributed to the formation of 2D iron-oxalate structures as a result of incorporation of the Fe atoms within the oxalate ions. The Fe-Fe distance is 0.5 nm, which is the shortest metal-metal distance reported so far for 2D coordination networks at surfaces. The drawback is that the obtained iron-oxalate networks are not very extended. They coexist on the surface with triangular structures that are also obtained when annealing the oxalate-only networks to 100˚C (Figure 5.10(b)). The triangular structures are most likely due to oxalate decomposition into formate ions and it is most likely this coexistence of the two structures that limits the growth of the honeycomb networks.

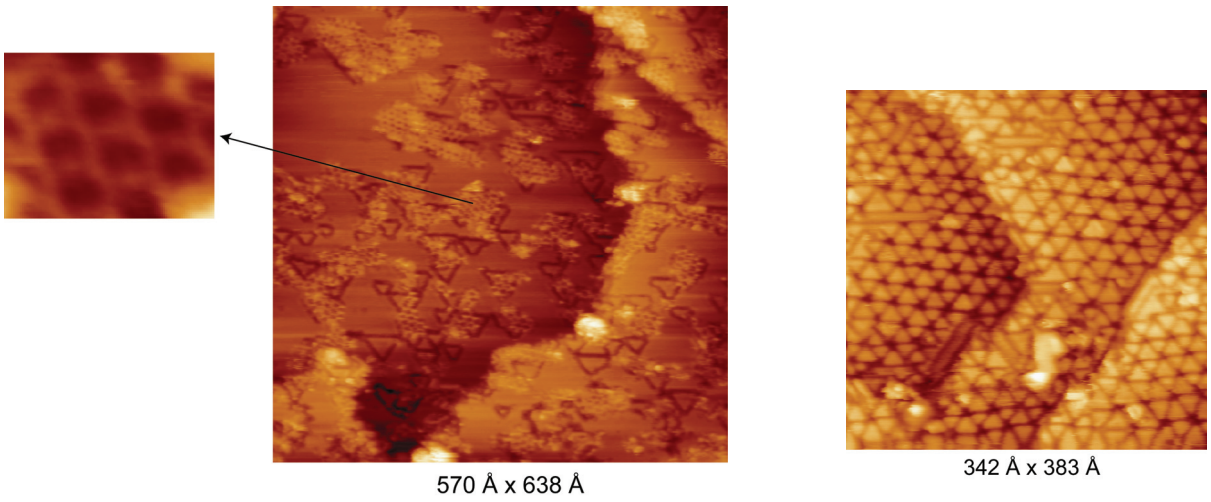

(a) (b)

Figure 5.10. (a) STM image (I=0.3 nA, V=1.4V) of the honeycomb network resulting after incorporating iron into the oxalate network and annealing to 100˚C for 10 min (b) STM image (I=0.5 nA, V=4 V) obtained after annealing only the oxalate network, without iron deposited on top, proving that the honeycomb arrangement is caused by the presence of the iron atoms that induce reorganization of the oxalate ions.

While still a lot of work needs to be done in order to obtain long range ordering of such structures, the results are an important initial step towards a fundamental understanding of the surface mediated formation of coordination networks and towards obtaining new magnetic nanostructure materials.

5.4. Bi-isonicotinic Acid on Au(111). Adsorption and Charge Transfer Dynamics

The adsorption of bi-isonicotinic acid monolayers on Au(111) and its coupling to the substrate were investigated. The molecules adsorb intact on the Au(111) surface and adopt an almost flat orientation, in contrast to what was previously observed on TiO_2 [49]. The core level photoemission spectra show two peak components for the O 1*s* signal, with a 1:1 intensity ratio (Figure 5.11), indicating that the bi-isonicotinic acid molecules do not deprotonate upon adsorption and the analysis of the angular dependence of the XAS resonances (not shown here), gives an average tilt angle of the molecules of 70˚±5˚ with respect to the surface normal.

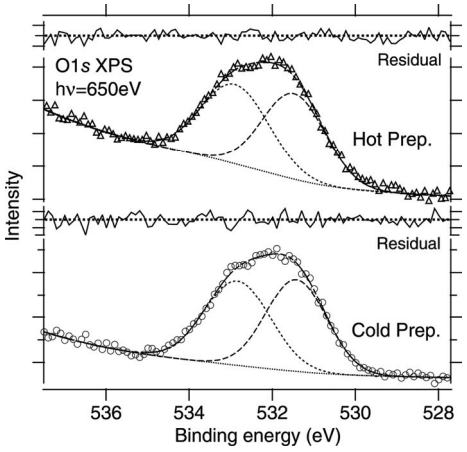

Figure 5.11. O 1*s* photoemission spectra for a monolayer of bi-isonicotinic acid on Au(111) for the indicated preparations. The low binding energy peak corresponds to the carbonyl oxygen and the high binding energy peak to the hydroxyl oxygen.

The coupling strength with the substrate was investigated by resonant photoemission spectroscopy. It was found that the adsorbate LUMO+1 and LUMO+2 overlap with unoccupied states on the substrate, which indicates that charge transfer from the LUMO+1 and LUMO+2 of the adsorbate into the substrate states is energetically allowed. The situation is more complicated for the LUMO state, which partly overlaps with the occupied levels of Au(111) (part of the LUMO resonance is pulled below the Fermi level in the final state). Charge transfer to the substrate will only be possible from those levels located on the lower binding energy side of the orbital (which on the photon energy scale of the XAS spectrum translates into the high photon energy side of the LUMO). In the same time, the partial LUMO overlap with the Au(111) states indicates that the reverse process, namely the charge transfer from the Au(111) states at the Fermi level to the bi-isonicotinic acid states located on the high binding energy side (low photon energy side on the XAS scale) is energetically allowed, which is also the case for the present research, as will be discussed. Figure 5.12(a) shows the N 1*s* RPES spectrum for the monolayer bi-isonicotinic acid on Au(111). Apart from the Auger spectator signal, the spectrum contains an additional Auger-like feature, at 8 eV binding energy for 402 eV photon energy, and at 13 eV for 407 eV photon energy. Such features were not observed on clean Au(111) or multilayer bi-isonicotinic acid RPES. It is tentatively assigned to ultrafast charge transfer from the Au(111) states at the Fermi level to the overlapping LUMO states of the core excited molecule and termed here as “superspectator”.

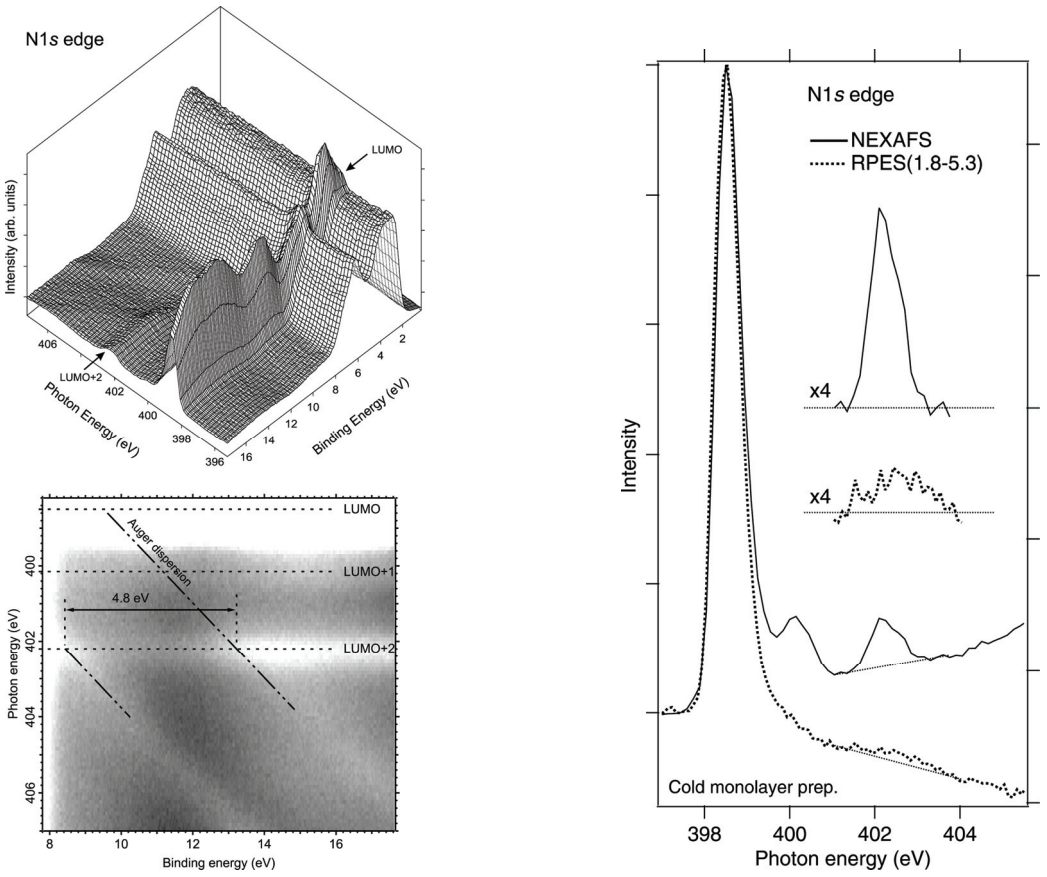

(a) (b)

Figure 5.12. (a) The result of the N 1*s* RPES measurement performed on a monolayer of bi-isonicotinic acid on Au(111) and (b) comparison between the N 1*s* RPES spectrum obtained by integration over the binding energy interval 1.8 to 5.3 eV and the XAS intensity. The spectra were normalised to the LUMO resonance.

The comparison between the RPES and XAS intensities (Figure 5.12(b)) indicates that no charge transfer takes place from the bi-isonicotinic acid LUMO+2 state into the substrate. The RPES:XAS LUMO+2 intensity ratio of 0.34:1 fits to the value of 0.33:1 reported previously for multilayer bi-isonicotinic acid on Au(111) where no CT is likely to take place. The apparent disappearance of the LUMO+1 intensity would imply that charge transfer might be allowed from this particular state, but since its intensity is already very low in the XAS spectrum, it is not reliable to be used as an indicator of charge transfer. And more than that, the LUMO+1 and LUMO+2 resonances of the monolayer do not differ from the multilayer (not shown here) supporting the conclusion that charge transfer from the bi-isonicotinic acid to Au(111) does not take place. In conclusion, the RPES data suggest the possibility of femtosecond charge transfer from the Au(111) substrate to the molecules upon resonant excitation, but no charge transfer is observed from the adsorbate as was the case in previous studies on TiO_2 [50,55]. These results are important for solar cells based on TiO_2/Au/dye interfaces.

Conclusions

The research work presented in this thesis follows a number of distinct directions, namely the study of geometry and electronic structure of iron phthalocyanine on surfaces, the adsorption of gases on iron phthalocyanine, the study of a 2D oxalate based coordination network, and the adsorption and charge transfer dynamics of bi-isonicotinic acid on Au(111).

Regarding the phthalocyanine adsorption on HOPG and Au(111) surfaces, it was found that monolayers of FePc lie flat on both HOPG and Au(111) and that the adsorbate-substrate coupling strength is significantly different on the two substrates. HOPG was found to be a weakly interacting substrate - the FePc molecular network and the HOPG surface are held together by van der Waals type interactions. With Au(111) instead, the FePc molecules form covalent-type interactions, characterised by a non-negligible electron transfer from the surface to the iron atom of FePc.

Ligand adsorption on FePc significantly affects the electronic and geometric structure at the interface through the formation of iron-ligand bonds. The formation of a bond between the iron atom and the ligand decouples the FePc molecules from the Au(111) substrate. The spin state of the iron atom is changed substantially, and both a lowering of the spin state or a complete spin quench can be obtained, depending on which ligand molecule is used. Our findings show that the molecule-substrate interaction and molecular spin on the central iron atom can be tuned by adsorption of molecular ligands. Such results indicate that a precise tuning of the bond strength and spin state of the FePc molecules by ligand attachment is within reach.

Oxalate ligands on Cu(111) self-assemby into 2D hexagonal networks that have the ability to coordinate to iron atoms. In the presence of iron, the networks transform into honeycomb iron-oxalate structures, with a metal-metal distance of 0.5 nm, which is the shortest metal-metal distance reported so far for 2D coordination networks at surfaces.

The study of bi-isonicotinic acid on Au(111) suggests the possibility of femtosecond charge transfer from the Au(111) substrate to the bi-isonicotinic acid molecules. No charge transfer is observed from the adsorbate to the substrate. The results are important for solar cells based on TiO_2/Au/dye interfaces. Charge transfer from the dye to the oxide is possible, while charge transfer to the Au would be much slower and not likely to occur. In addition, the gold could be used to refill electrons on the dye on the femtosecond scale.

Acknowledgments

There are many people who, in many ways, have contributed to the work presented in this thesis and to whom I would like to express my gratitude.

First of all, I would like to thank my supervisors, Joachim Schnadt and Jesper Andersen. Many thanks to Achim first of all for trusting me and giving me the opportunity to do this PhD in Physics, for always being available for discussions, and for scientific and moral support. I have learnt a lot from you! I am grateful to Jesper for being a great person, for valuable and wise advices in the field of science and not only. It was a pleasure to work with you both!

All the experiments presented in this thesis are the result of a team work. I would like to thank the other members of the team: Evren, Karina, Jan, John (with whom I shared my very first beam time and who, together with Evren witnessed one of the experiences I wish I have never had – me, crashing the evaporator into the HOPG sample in the preparation chamber of beam line I511 ☺), and all the colleagues from the MONET network with whom I have shared beamtimes (Tuğçe, Andrey, Anna, Graziano, Marta). Thank you for making the "long" days and nights in MAX-lab more pleasant and enjoyable. To Karina and Jan I would also like to thank for fruitful scientific discussions and for helping me when I needed. Special thanks to my colleague and friend Evren.

I want to give my thanks to our collaborators from Ecole normale supérieure de Lyon, Bin Wang and Marie-Laure Bocquet who have performed the DFT calculations for us, for always being prompt in giving us answers and, very importantly, for having the right answers for the questions we were interested in ☺.

I am very grateful to Roberto, Marta, José-Maria and David from Universidad Autónoma de Madrid, for helping and supporting me during my two research stays in their lab, where I have performed STM experiments.

I have spent a lot of time in MAX-lab during my PhD years. I would like to acknowledge all the MAX-lab Staff for technical support.

I am also grateful to all our co-authors.

I would like to thank all the members – students and supervisors of the Early Stage Researcher Training Network MONET. The project meeting were always enjoyable with you, guys.

My very special thanks go to all the former and present members of the Division of Synchrotron Radiation Research for creating a pleasant working environment.

I would also like to acknowledge the European Union for financial support through the Early Stage Researcher Training Network MONET.

I want to also thank all my friends at home.

Finally, I would like to take the opportunity to express my gratitude to my dearest people in this world: my parents, my brother, my grandparents, for their unconditioned love and support. Vasile, thank you for being patient with me, for always being there for me during these years!

Thank you all!

Lund, August 2010

References

[1] Lionel R. Milgrom, The Colours of Life – An Introduction to the Chemistry of Porpryrins and Related Compounds, Oxford University Press, New York 1997.

[2] N. B. McKeown, Phthalocyanine Materials: Synthesis, Structure and Function, Cambridge University Press, Cambridge (1998).

[3] O. L. Kaliya, E. A. Lukyanets, and G. N. Vorozhtsov, J. Porphyrins Phthalocyanines 3, (1999) 592-610.

[4] M. Toledo, Alzira M. S. Lucko, and Y. Gushikem, J. Mater. Sci. Lett. 39, (2004) 6851-6854.

[5] J. C. Obirai and T. Nyokong, J. Electroanal. Chem. 600, (2007) 251–256.

[6] Y. Lu and R. G. Reddy, Int. J. Hydrogen Energy 33, (2008) 3930-3937.

[7] J. Darwent, P. Douglas, A. Harriman, G. Porter, and M. C. Richoux, Coord. Chem. Rev. 44, (1982) 83-126.

[8] S. Baranton, C. Coutanceau, C. Roux, F. Hahn, and J. M. Leger, J. Electroanal. Chem. 577, (2005) 223–234.

[9] E. H. Yu, S. Cheng, K. Scott, and B. Logan, J. Power Sources 171, (2007) 275–281.

[10] L. T. Weng, P. Bertrand, G. Lalande, D. Guay, and J. P. Dodelet, Appl. Surf. Sci. 84, (1995) 9-21.

[11] F. Zhao, F. Harnisch, U. Schroder, F. Scholz, P. Bogdanoff, and I. Herrmann, Electrochem. Comm. 7, (2005) 1405–1410.

[12] K. Arihara, L. Mao, P. A. Liddell, E. Marino-Ochoa, A. L. Moore, T. Imase, D. Zhang, T. Sotomura, and T. Ohsaka, J. Electrochem. Soc. 151, (2004) A2047-A2052.

[13] L. Zhang, J. Zhang, D. P. Wilkinson, and H. Wang, J. Power Sources 156, (2006) 171-182.

[14] L. Zhang, C. Song, J. Zhang, H. Wang, and D. P. Wilkinson, J. Electrochem. Soc. 152, (2005) A2421-A2426.

[15] J. Ma, J. Wang, and Y. Liu, J. Power Sources 172**,** (2007) 220-224.

[16] K. Wiesener, D. Ohms, V. Neumann, and R. Franke, Mater. Chem. Phys. 22, (1989) 457-475.

[17] C. J. Liu, J.J. Shih, Y. H. Ju, Sens. Actuators B 99, (2004) 344–349.

[18] M. I. Newton, T. K. H. Starke, M. R Willis, G. McHale, Sens. Actuators B 67, (2000) 307–311.

[19] P. T. Moseley, Sens. Actuators B 3, (1991) 167-174.

[20] J. C. Buchholz, Appl. Surf. Sci. 1, (1978) 547—551.

[21] K. Morishige, S. Tomoyasu, and G. Iwano, Langmuir 13, (1997) 5184-5188.

[22] T. A. Jones and B. Bott, Sens. Actuators 9, (1986) 27–37.

[23] S. Chakane, A. Gokarna, and S. V. Bhoraskar, Sens. Actuators B 92, (2003) 1–5.

[24] A. M. Paoletti, G. Pennesi, G. Rossi, A. Generosi, B. Paci, and V. R. Albertini, Sensors 9, (2009) 5277-5297.

[25] V. Vrkoslav, I. Jelinek, M. Matocha, V. Kral, and J. Dian, Mater. Sci. Eng. C 25, (2005) 645-649.

[26] T. Nyokong and S. Vilakazi, Talanta 61, (2003) 27-35.

[27] C. G. Claessens, W. J. Blau, M. Cook, M. Hanack, R. J. M. Nolte, T. Torres, and D. Wöhrle, Monatsh. Chem. 132, (2001) 3-11.

[28] J. Spadavecchia, G. Ciccarella, and R. Rella, Sens. Actuators B 106, (2005) 212-220.

[29] S. Paul and M. Joseph, Sens. Actuators B 140, (2009) 439-444.

[30] A. Pallaniapan and S. Moochhala, F. E. H. Tay, X. Su, N. C. L. Phua, Sens. Actuators B 129, (2008) 184–187.

[31] S. Maldonado, E. Garcia-Berrios, M. D. Woodka, B. S. Brunschwig, and N. S. Lewis, Sens. Actuators B 134, (2008) 521-531.

[32] M. Dubey, S. L. Bernasek, and S. Schwartz, J. Am. Chem. Soc. 129, (2007) 6980-6981.

[33] L. Alagna, A. Capobianchi, A. M. Paoletti, G. Pennesi, G. Rossi, M. P. Casaletto, A. Generosi, B. Paci, and V. R. Albertini, Thin Solid Films 515, (2006) 2748-2753.

[34] K.C. Ho and Y.-Ham Tsou, Sens. Actuators 77, (2001) 253-259.

[35] S. Riad, Thin Solid Films 370, (2000) 253-257.

[36] T. Abe, K. Nagai, K. Sekimoto, A. Tajiri, and T. Norimatsu, Electrochem. Comm. 7, (2005) 1129–1132.

[37] C. C. Claessens, U. Hahn, and T. Torres, The Chemical Record 8, (2008) 75-97.

[38] G. de la Torre, C. G. Claessens, and T. Torres, Chem. Comm. 20, (2007) 2000-2015.

[39] G. Gu, G. Parthasarathy, and S. R. Forrest, Appl. Phys. Lett. 74, (1999) 305-307.

[40] L. S. Hung and C. W. Tang, Appl. Phys. Lett 74, (1999) 3209-3211.

[41] D. Hohnholz, S. Steinbrecher, and M. Hanack, J. Mol. Struct. 521, (2000) 231-237.

[42] N. R. Armstrong, W. Wang, D. M. Alloway, D. Placencia, E. Ratcliff, and M. Brumbach, Macromol. Rapid Commun. 30, (2009) 717-731.

[43] J. Yuan, J. Zhang, J. Wang, X. Yan, D. Yan, and W. Xu, Appl. Phys. Lett. 82, (2003) 3967-3969.

[44] J. P. Taquet, C. Frochot, V. Manneville, and M. B. Heyob, Curr. Med. Chem. 14, (2007) 1673-1687.

[45] C. N. Lunardi and A. C. Tedesco, Curr. Org. Chem. 9, (2005) 813-821.

[46] B. O'Regan and M. Grätzel, Nature 353, (1991) 737-739.

[47] A. Hagfeldt and M. Grätzel, Acc. Chem. Res. 33, (2000) 269-277.

[48] E. W. McFarland and J. Tang, Nature 421, (2001) 616-618.

[49] L. Patthey, H. Rensmo, P. Persson, K. Westemark, L. Vayssieres, A. Stashans, Å. Petersson, P. A. Brühwiler, H. Siegbahn, S. Lunell, and N. Mårtensson, J. Chem. Phys. 110, (1999) 5913-5918.

[50] J. Schnadt, P. A. Brühwiler, L. Patthey, J. N. O'Shea, S. Södergren, M. Odelius, R. Ahuja, O. Karis, M. Bässler, P. Persson, H. Siegbahn, S. Lunell, and N. Mårtensson, Nature 418, (2002) 620-623.

[51] J. N. O'Shea, J. Schnadt, P. A. Brühwiller, H. Hillesheimer, N. Mårtensson, L. Patthey, J. Krempasky, C. K. Wang, Y. Luo, and H. Ågren, J. Phys. Chem. B 105, (2001) 1917-1920.

[52] J. N. O'Shea, J. Schnadt, L. Patthey, H. Hillesheimer, J. Krempasky, D. Nordlund, D. Nagasono, P. A. Brühwiller, and N. Mårtensson, Surf. Sci. 486, (2001) 157-166.

[53] P. Persson, S. Lunell, Sol. Energy Mat. Sol. Cells 63, (2000) 139-148.

[54] P. Persson, S. Lunell, P. A. Brühwiller, J. Schnadt, S. Södergren, J. N. O'Shea, O. Karis, H. Siegbahn, and N. Mårtensson, J. Chem. Phys. 112, (2000) 3945-3948.

[55] J. Schnadt, J. N. O'Shea, L. Patthey, L. Kjeldgaard, J. Åhlund, K. Nilson, J. Schiessling, J. Krempaský, M. Shi, O. Karis, C. Glover, H. Siegbahn, N. Mårtensson, and P. A. Brühwiler, J. Chem. Phys. 119, (2003) 12462-12472.

[56] J. Schnadt, J. N. O-Shea, L. Patthey, J. Schiessling, J. Krempaský, M. Shi, N. Mårtensson, and P. A. Brühwiler, Surf. Sci. 544, (2003) 74-86.

[57] J. Schnadt, J. Schiessling, J. N. O-Shea, S. M. Gray, L. Patthey, M. K. J. Johansson, M. Shi, J. Krempaský, J. Åhlund, P. G. Karlsson, P. Persson, N. Mårtensson, and P. A. Brühwiler, Surf. Sci. 540, (2003) 39-54.

[58] J. Schnadt, A. Henningsson, M. P. Andersson, P. G. Karlsson, P. Uvdal, H. Siegbahn, P. A. Brühwiler, and A. Sandell, J. Chem. Phys. B 108, (2004) 3114-3122.

[59] H. Hertz, Annalen der Physik 31, (1887) 983-1000.

[60] A. Einstein, Annalen der Physik 17, (1905) 132-148.

[61] http://nobelprize.org.

[62] S. Hüfner, Photoelectron Spectroscopy, Springer-Verlag, Berlin Heidelberg 1995.

[63] L. C. Feldman and J. W. Mayer, Fundamentals of Surface and Thin Film Analysis, Elsevier Science Publishing, New York 1986.

[64] W. Schattke and M. A. Van Hove, Solid-State Photoemission and Related Methods – Theory and Experiment, Wiley-VCH, Weinheim 2003.

[65] N. Mårtensson, Core-level spectroscopies applied to surfaces and adsorbates, Lecture notes, Laussane1994.

[66] U. Gelius, S. Svensson, H. Siegbahn, E. Basilier, Å. Faxälv, and K. Siegbahn, Chem. Phys. Lett. 28, (1974) 1-7.

[67] R. Manne and T. Åberg, Chem. Phys. Lett. 7, (1970) 282-284.

[68] D. Briggs and M. P. Seah, Practical Surface Analysis – Second Edition, Vol.1 – Auger and X-ray Photoelectron Spectroscopy, John Wiley & Sons, Chichester 1990.

[69] www.maxlab.lu.se

[70] M. Hollas, Modern Spectroscopy – Fourth Edition, John Wiley & Sons v, Chichester 2004.

[71] J. L. Campbell and T. Papp, At. Data Nucl. Data Tables 77, (2001) 1–56.

[72] N. Andersen and C. O. Almbladh, J. Phys.: Condens. Matter. 13, (2001) 11267-11291.

[73] S. Doniach and M. Sunjic, J. Phys. C 3, (1970) 285-291.

[74] A. Kittel, Introduction to Solid State Physics, John Wiley & Sons, Danvers 2005.

[75] D. P. Wodruff and T. A. Delchar, Modern Techniques of Surface Science, 2nd edition, Cambridge University Press, Cambridge 1994.

[76] M. P. Seah and W. A. Dench, Surf. Interface Anal. 1, (1979) 2–11.

[77] A. Zangwill, Physics at Surfaces, Cambridge University Press, Cambridge 1988.

[78] A. Thorne, U. Litzén, S. Johansson, Spectrophysics: principles and applications, Springer, Berlin 1999.

[79] P. Atkins, R. Friedman, Molecular Quantum Mechanics – 4th edition, Oxford University Press, New York 2005.

[80] http://srdata.nist.gov/xps/selEnergyType.aspx

[81] C. S. Fadley and D. A. Shirley, Phys. Rev. A 2, (1970) 1109-1120.

[82] F. Sirotti, M. De Santis, and G. Rossi, Phys. Rev. B 48, (1993) 8299-8306.

[83] F. Sirotti and G. Rossi, Phys. Rev. B 49, (1994) 15682-15687.

[84] J. Weissenrieder, M. Göthelid, M. Månsson, H. Von Schenck, O. Tjernberg, and U. O. Karlsson, Surf. Sci. 527, (2003) 163-172.

[85] G. van der Laan, Phys. Rev. B 51, (1995) 240-249.

[86] C. Bethke, E. Kisker, N. B. Weber, and F. U. Hillebrecht, Phys. Rev. B. 71, (2005) 024413(1)-(7).

[87] R. D. Cowan, The Theory of Atomic Structure and Spectra, University of California Press, Berkeley–Los Angeles-London 1981.

[88] P. Wernet, J. Schultz, B. Sonntag, K. Godehusen, P. Zimmermann, A. N. Grum-Grzhimailo, N. M. Kabachnik, M. Martins, Phys. Rev. A 64, (2001) 042707(1)-(13).

[89] P. A. Cox, The Electronic Structure and Chemistry of Solids, Oxford Science Publications, New York 1987.

[90] D. F. Shriver, P. W. Atkins, C. H. Langford, Inorganic Chemistry – 2nd edition, Oxford University Press, Oxford New York 1994.

[91] G. V. Quedraogo, D. Benlian, and L. Porte, J. Chem. Phys. 73, (1980) 642-647.

[92] J.Stöhr and D. A. Outka, Phys. Rev. B 36, (1987) 7891-7905.

[93] J. Stöhr, NEXAFS Spectroscopy, Springer, Berlin, Heidelberg, New York 1992.

[94] G. Attard and C. Barnes, Surfaces, Oxford University Press, New York 1998.

[95] P. A. Brühwiler, O. Karis, and N. Mårtensson, Rev. Mod. Phys. 74, (2002) 703-740.

[96] A. Föhlisch, P. Feulner, F. Hemmies, A. Fink, D. Menzel, D. Sanchez-Portal, P. Eschenique, and W. Wurth, Nature 436, (2005) 373-376.

[97] O. Björneholm, A. Nilsson, A. Sandell, B. Hernäss, and N. Mårtensson, Phys. Rev. Lett, 68 (1992) 1892-1895.

[98] W. Eberhardt, R. Dudde, M. L. M. Rocco, E. E. Koch, and S. Bernstorff, J. Electron. Spectrosc. Relat. Phenom., 51 (1990) 373-382.

[99] W. Wurth and D. Menzel, Chem. Phys. 251, (2000) 141-149.

[99] J. Schnadt, J. N. O'Shea, L. Patthey, J. Krempaský, N. Mårtensson, and P. A. Brühwiler, Phys. Rev. B 67, (2003) 235420(1)-(7).

[100] R. Nyholm, J. N. Andersen, U. Johansson, B. N. Jensen, and I. Lindau, Nucl. Instrum. Methods Phys. Res. A 467-468, (2001) 520-524.

[101] R. Denecke, P. Väterlein, M. Bässler, N. Wassdahl, S. Butorin, A. Nilsson, J. E. Rubensson, J. Nordgren, N. Mårtensson, and R. Nyholm. J. Electron Spectrosc. Relat. Phenom. 101-103, (1999) 971.

[102] www.maxlab.lu.se

[103] S. Werin, Accelerator Technique, Lecture notes, Lund 2006.

[104] H. Wiedemann, Particle Accelerator Physics – 3rd edition, Springer, New York 2007.

[105] D. Attwood, Soft X-rays and Extreme Ultraviolet Radiation – Principles and Applications, Cambridge University Press, New York 1999.

[106] H. Winick, S. Doniach, Synchrotron Radiation Research, Plenum Press, New York 1980.

[107] D. Roy and D. Tremblay, Rep. Prog. Phys. 53, (1990) 1621-1674.

[108] N. Mårtensson, P. Baltzer, P. A. Brühwiler, J. O. Forsell, A. Nilsson, A. Stenborg, and B. Wanneberg, J. Electron. Spectrosc. Relat. Phenom. 70, (1994) 117-128.

[109] H. Bubert and H. Jenett, Surface and Thin Film Analysis: Principles, Instrumentation, Applications, Wiley-VCH, Weinheim - Germany 2002.

[110] H. R. Verma, Atomic and Nuclear Analytical Methods – XRF, Mössbauer, XPS, NAA and Ion-Beam Spectroscopic Techniques, Springer, Verlag Berlin Heidelberg 2007.

[111] http://www.sciner.com/MCP/MCP.html

[112] J. L. Wiza, Nucl. Instrum. Methods 162, (1979) 587-601.

[113] http://hea-www.harvard.edu/HRC/mcp/mcp.html

[114] http://www.vgscienta.com

[115] D. R. Vij, Handbook of Applied Solid State Spectroscopy, Springer, New York 2006.

[116] G. Binning and H: Rohrer, IBM J. Res. Develop. 44, (2000) 279-293.

[117] G. Binning and H. Rohrer, Scanning Tunneling Microscopy – From Birth to Adolescence, Nobel lecture 1986.

[118] D. A. Bonnell, Scanning Tunneling Microscopy and Spectroscopy – Theory, Techniques and Applications, Wiley-VCH, New York 2001.

[119] A. Kubby and J. J. Boland, Surf. Sci. Rep. 26, (1996) 61-204.

[120] F. Besenbacher, Rep. Prog. Phys. 59, (1996) 1737-1802.

[121] J. Tersoff and D. R. Hamann, Phys. Rev. B 31, (1985) 805-813.

[122] J. Tersoff and D. R. Hamann, Phys. Rev. B 50, (1983) 1998-2001.

[123] J. Bardeen, Phys. Rev. Lett. 6, (1961) 57-59.

[124] R. Wiesendanger, Scanning Probe Microscopy and Spectroscopy – Methods and Applications, Cambridge University Press, Cambridge 1994.

[125] A. Selloni, P. Carnevali, E. Tosatti, and C. D. Chen, Phys. Rev. B 31, (1985) 2602-2605.

[126] N. D. Lang, Phys. Rev. B 34, (1986) 5947-5950.

[127] R. M. Feenstra, J. A. Stroscio, and A. P. Fein, Surf. Sci. 181, (1988) 295-306.

[128] C. J. Chen, J. Vac. Sci. Technol. A 6, (1988) 319-322.

[129] W. A. Hofer, A. S. Foster, and A. L. Shluger, Rev. Mod. Phys. 75, (2003) 1287-1331.

[130] X. Lu and K. W. Hipps, J. Phys. Chem. B 101, (1997) 5391-5396.

[131] V. L. Mironov, Fundamentals of Scanning Probe Microscopy, The Russian Academy of Sciences, Novgorod 2004.

[132] N. Papageorgiou, J. C. Mossoyan, M. Mossoyan-Deneux, G. Terzian, E. Janin, M. Göthelid, L. Giovanelli, J. M. Layet, and G. Le Lay, Appl. Surf. Sci. 162-163, (2000) 178-183.

[133] N. Papageorgiou, Y. Ferro, E. Salomon, A. Allouche, and J. M. Layet, Phys. Rev. B 68, (2003) 235105(1)-(10).

[134] L. Ottaviano, L. Lozzi, S. Santucci, S. Di Nardo, and M. Passacantando, Surf. Sci. 392, (1997) 52-61.

[135] Y. Wang, J. Kröger, R. Berndt, and W. A. Hofer, J. Am. Chem. Soc. 131, (2009) 3639-3643.

[136] C. Stadler, S. Hansen, I. Kröger, C. Kumpf, and E. Umbach, Nat. Phys. 5, (2009) 1 53-158.

[137] K. M. Kadish, K. M. Smith, and R. Guilard, The Porphyrin Handbook – vol. 16, Phthalocyanines: Spectroscopic and Electrochemical Characterization, Elsevier Science, San Diego (2003).

[138] B. Wang, Electronic structure of monolayer graphene and biomimetic molecules on metal surfaces, Doctoral Thesis, Ecole normale supérieure de Lyon, Lyon 2010.

[139] M. S. Liao and S. Scheiner, J. Chem. Phys. 114, (2001) 9780-9791.

[140] M. S. Liao and S. Scheiner, J. Comput. Chem. 23, (2002) 1391-1403.

[141] A. M. Schaffer, M. Gouterman, and E. R. Davidson, Theoret. Chim. Acta 30, (1973) 9-30.

[142] Z. Hu, B. Li, A. Zhao, J. Yang, and J. G. Hou, J. Phys. Chem. C 112, (2008) 13650-13655.

[143] X. Lu, K. W. Hipps, X. D. Wang, and U. Mazur, J. Am. Chem. Soc. 118, (1996) 7197-7202.

[144] P. Gargiani, M. Angelucci, C. Mariani, and M. G. Betti, Phys. Rev. B 81, (2010) 085412(1)-(7).

[145] H. Peisert, M. Knupfer, and J. Fink, Surf. Sci. 515, (2002) 491–498.

[146] V. Oison, M. Koudia, M. Abel, and L. Porte, Phys. Rev. B 75, (2007) 135428(1)-(5).

[147] A. Zhao, Q. Li, L. Chen, H. Xiang, W. Wang, S. Pan, B. Wang, X. Xiao, J. Yang, J. G. Hou, and Q. Zhu, Science 309, (2005) 1542-1544.

[148] Z. Li, B. Li, J. Yang, and J. G. Hou, Acc. Chem. Res. 43, (2010) 954-962.

[149] J. J. Cox, S. M. Bayliss, and T. S. Jones, Surf. Sci. 433-435, (1999) 152-156.

[150] L. Zhang, H. Peisert, I. Biswas, M. Knupfer, D. Batchelor, and T. Chassé, Surf. Sci. 596, (2005) 98-107.

[151] A. Ruocco, F. Evangelista, R. Gotter, A. Attili, and G. Stefani, J. Phys. Chem. C 112, (2008) 2016-2025.

[152] Y. Bai, F. Buchner, M. T. Wendahl, I. Kellner, A. Bayer, H. P. Steinrück, H. Marbach, and J. M. Gottfried, J. Phys. Chem C 112, (2008) 6087-6092.

[153] P. Palmgren, K. Nilson, S. Yu, F. Hennies, T. Angot, C. I. Nlebedim, J. M. Layet, G. L. Lay, and M. Göthelid, J. Phys. Chem. C. 112, (2008) 5972-5977.

[154] P. Palmgren, T. Angot, C. I. Nlebedim, J.. M. Layet, G. L. Lay, and M. Göthelid, J. Chem. Phys. 128, (2008) 064702(1)-(6).

[155] T. Takami, C. Carrizales, and K. W. Hipps, Surf. Sci. 603, (2009) 3201-3204.

[156] K. Flechtner, A. Kretschmann, H. P. Steinrück, and J. M. Gottfried, J. Am. Chem. Soc. 129, (2007) 12110-12111.

[157] T. Kawai, M. Soma, Y. Matsumoto, T. Onishi, and K. Tamaru, Chem. Phys. Lett. 37, (1976) 378-382.

[158] C. V. Quedraogo, D. Benlian, and L. Porte, J. Chem. Phys. 73, (1980) 642-647.

[159] T. S. Ellis, K. T. Park, M. D. Ulrich, S. L. Hulbert, and J. E. Rowe, J. Appl. Phys. 100, (2006) 093515.

[160] M. Grobosch, V. Y. Aristov, O. V. Molodtsova, C. Schmidt, B. P. Doyle, S. Nannarone, and M. Knupfer, J. Phys. Chem. 113, (2009) 13219-13222.

[161] N. Tsukahara, K. Noto, M. Ohara, S. Shiraki, N. Takagi, Y. Takata, J. Miyawaki, M. Taguchi, A. Chainami, S. Shin, and M. Kawai, Phys. Rev. Lett 102, (2009) 167203(1)-(4).

[162] L. Gao, W. Ji, Y. B. Hu, Z. H. Cheng, Z. T. Deng, Q. Liu, N. Jiang, X. Lin, W. Guo, S. X. Du, W. A. Hofer, X. C. Xie, and H. J. Gao, Phys. Rev. Lett. 99, (2007) 106402(1)-(4).

[163] H. Wende, M. Bernien, J. Luo, C. Sorg, N. Popandian, J. Kurde, J. Miguel, M. Piantek, X. Xu, P. Eckhold, W. Kuch, K. Baberschke, P. M. Panchmata, B. Sanyal, P. M. Oppeneer, and O. Eriksson, Nat. Mater. 6, (2007) 516-520.

[164] A. Scheybal, T. Ramsvik, R. Bertschinger, M. Putero, F. Nolting, and T. A. Jung, Chem. Phys. Lett. 411, (2005) 214-220.

[165] M. Bernien, J. Miguel, C. Weis, M. E. Ali, J. Kurde, B. Krumme, P. M. Panchmatia, B. Sanyal, M. Piantek, P. Srivastava, K. Baberschke, P. M. Oppenner, O. Eriksson, W. Kuch, and H. Wende, Phys. Rev. Lett. 102, (2009) 047202(1)-(4).

[166] www.wikipedia.org

[167] G. A. Jeffrey, An Introduction to Hydrogen Bonding, Oxford University Press, New York 1997.

[168] P. M. Dewick, Essentials of Organic Chemistry, John Wiley & Sons. Ltd, West Sussex 2006.

[169] J. A. Joule and K. Mills, Heterocyclic Chemistry, Blackwell Publishing, Oxford, Malden, Carlton, Kurfürstendamm 2000.

[170] I. Fleming, Molecular Orbitals and Organic Chemical Reactions, John Wiley & Sons. Ltd, West Sussex 2010.

[171] M. A. Albert and J. T. Yates, The Surface Scientist's Guide to Organometallic Chemistry, American Chemical Society, Washington DC 1987.

[172] G. Blyholder, J. Phys. Chem., 68 (1964) 2772-2777.

[173] P. Bennich, T. Wiell, O. Karis, M. Weinelt, N. Wassdahl, A. Nilsson, M. Nyberg, L. G. M. Pettersson, J. Stöhr, and M. Samant, Phys. Rev. B 57, (1998) 9274-9284.

[174] A. Nilsson, and L. G. M. Pettersson, Surf. Sci. Rep. 55, (2004) 49-167.

[175] J. C. Kotz, P. M. Treichel, and J. M. Townsend, Chemistry and Chemical Reactivity, Thomson Brooks/Cole, Belmont 2009.

[176] E. M. Shustorovich, Zhurnal Strukturnoi Khimii 3, (1962) 103,105.

[177] L. J. Ignarro, Nitric Oxide Biology and Pathology, Academic Press, San Diego, San Francisco, New York, Boston, London, Sydney, Tokyo 2000.

[178] R. D. Feltham, J. H. Enemark, Top. Stereochem. 12, (1981) 155-215.

[179] M. Hoshino, L. Laverman, and P. C. Ford, Coord. Chem. Rev. 187, (1999) 75-102.

[180] A. Ghosh and T. Wondimagegn, J. Am. Chem. Soc. 122, (2000) 8101-8102.

[181] C. Rovira, K. Kunc, J. Hutter, P. Ballone, and M. Parrinello, Int. J. Quantum Chem. 69, (1998) 31-35.

[182] A. F. Wells, Structural Inorganic Chemistry, Oxford University Press, Oxford 1984.

[183] S. Stephanov, T. Strunskus, M. Lingenfelder, A. Dmitriev, H. Spillmann, N. Lin, J. V. Barth, C. Wöll, and K. Kera, J. Phys. Chem. 108, (2004) 19392-19397.

[184] M. Wühn, J. Weckesser, and C. Wöll, Langmuir 17, (2001) 7605-7612.

[185] O. Karis, J. Hasselström, N. Wassdahl, M. Weinelt, A. Nilsson, M. Nyberg, L. G. M. Pettersson, J. Stöhr, and M. G. Samant, J. Chem. Phys. 112, (2000) 8146-8155.

[186] Q. Chen, C. C. Perry, B. G. Frederick, P. W. Murray, S. Haq, and N. V. Richardson, Surf. Sci. 446, (2000) 63-75.

[187] M. R. Columbia and P. A. Thiel, J. Electroanal. Chem. 369, (1993) 1-14.

[188] E. Bauer and N. Poppa, Thin Solid Films 12, (1972) 167-185.

[189] C. Argile and G. E. Rhead, Surf. Sci. Rep. 10, (1998) 277-356.

[190] J. Åhlund, J. Schnadt, K. Nilson, E. Göthelid, J. Schiessling, F. Besenbacher, N. Mårtensson, and C. Puglia, Surf. Sci. 601, (2007) 3661-3667.

[191] R. D. Gould, Coord. Chem. Rev. 156, (1996) 237-274.

[192] M. Ashida, N. Uyeda, and E. Suito, J. Cryst. Growth 8, (1971) 45-46.

[193] M. Scrocco, C. Ercolani, and A. M. Paoletti 63, (1993) 155-166.

[194] F. Iwatsu, J. Phys. Chem. 92, (1988) 1678-1681.

[195] C. Chambers and A K. Holliday, Modern Innorganic Chemistry, Butterwoths &Co, London 1975.

[196] IUPAC Compendium of Chemical Terminology 2nd Edition (1997).

[197] P. Batra, N. Garcia, H. Rohrer, H. Salemink, E. Stoll, and S. Ciraci, Surf. Sci. 181, (1987) 126-138.

[198] R. Tatar and S. Rabii, Phys. Rev. B 25, (1982) 4126-4140.

[199] V. Barth, H. Brune, G. Ertl, and R. J. Ben, Phys. Rev. B 42, (1990) 9307-9318.

[200] B. K. Min, A. R. Alemozafar, M. M. Biener, J. Biener, and C. M. Friend, Top. Catal. 36, (2005) 77-90.

[201] N. Takeuchi, C. T. Chan, K. and M. Ho, Phys. Rev. B 43, (1991) 13899-13906.

[202] http://nobelprize.org.

[203] R. S. Rowland and R. Taylor, J. Phys. Chem. 100, (1996) 7384-7391.

[204] http://goldbook.iupac.org.

[205] D. Écija, R. Otero, L. Sánchez, J. M. Gallego, Y. Wang, M. Alcamí, F. Martín, N. Martín, and R. Miranda, Angew. Chem. Int. Ed. 46, (2007) 7874-7877.

[206] E. E. A. Kelly, W. Xu, M. Lukas, R. Otero, M. Mura, Y.-J. Lee, E. Lægsgaard, I. Stensgaard, L. N. Kantorovich, and F. Besenbacher, Small 4, (2008) 1494-1500.

[207] K. Kannappan, T. Y. Werblowsky, K. T. Rim, B. J. Berne, and J. W. Flynn, J. Phys. Chem. B 111, (2007) 6634-6642.

[208] M. Lackinger, S. Griessl, T. Markert, F. Jamitzky, and W. M. Heckl, J. Phys. Chem. B 108, (2004) 13652-13655.

[209] M. Koudia, M. Abel, C. Maurel, A. Bliek, D. Catalin, M. Mossoyan, J.-C. Mossoyan, and L. Porte, J. Phys. Chem. B 110, (2006) 10058-10062.

[210] S. Clair, S. Pons, A. P. Seitsonen, H. Brune, K. Kern, and J. V. Barth, J. Phys. Chem. B 108, (2004) 14585-14590.

[211] S. J. Grabowski, Hydrogen Bonding – New Insights (vol. 3 of the series Challenges and Advances in Computational Chemistry and Physics), Springer, Dordrecht, 2006.

[212] A. D. Buckingham, J. E. Del. Bene, and S. A. C. McDowell, Chem. Phys. Lett. 463, (2008) 1-10.

[213] M. Levitt and M. F. Perutz, J. Mol. Biol 201, (1988) 751-754.

[214] J. D. Augspurger and C. E. Dykstra, J. Phys. Chem. 96, (1992) 7252-7257.

[215] M. Piacenza and S. Grimme, ChemPhysChem 6, (2005) 1554-1558.

[216] P. Mignon, S. Loverix, F. D. Proft, and P. Geerlings, J. Phys. Chem. A 108, (2004) 6038-6044.

[217] E. G. Hihenstein and C. D. Sherrill, J. Phys. Chem. A 113, (2009) 878-886.

[218] H. Peisert, M. Knupfer, and J. Fink, Surf. Sci. 512, (2002) 491-498.

[219] B. Brena, Y. Luo, M. Nyberg, S. Carniato, K. Nilson, Y. Alfredsson, J. Åhlund, N. Mårtenson, H. Siegbahn, and C. Puglia, Phys. Rev. B 70, (2004) 195214(1)-(6).

[220] D. A. Evans, H. J. Steiner, S. Evans, R. Middleton, T. S. Jones, S. Park, T. U. Kampen, D. R. T. Zahn, G. Cabaih, and I. T. McGovern, J. Phys.: Condens. Matter 15, (2003) S2729-S2740.

[221] Y. Alfredsson, B. Brena, K. Nilson, J. Åhlund, L. Kjeldgaard, M. Nyberg, Y.Luo, N. Mårtensson, A. Sandell, C. Puglia, and H. Siegbahn, J. Chem. Phys. 122, (2005) 214723(1)-

[222] J. Åhlund, K. Nilson, J. Schiessling, L. Kjeldgaard, S. Berner, N. Mårtensson, C. Puglia, B. Brena, M. Nyberg, and Y. Luo, J. Chem. Phys. 125, (2006) 034709(1)-(7).

[223] A. Ruocco, F. Evangelista, A. Attili, M. P. Donzello, M. G. Betti, L. Giovanelli, and G. Rotter, J. Electron. Spectrosc. Relat. Phenom. 137-140, (2004) 165-169.

[224] Y. Niwa, H. Kobayashi, and T. Tsuchiya, J. Chem. Phys. 60, (1974) 799-807.

[225] B. Brena and Y. Luo, Radiat. Phys. Chem. 75, (2006) 1578-1581.

[226] N. Papageorgiou, E. Salomon, T. Angot, J. M. Layet, L. Giovanelli, and G. L. Lay, Prog. Surf. Sci. 77, (2004) 139-170.

[227] F. Evangelista, V. Carravetta, G. Stefani, B. Jansik, M. Alagia, S. Stranges, and A. Ruocco, J. Chem. Phys. 125, (2007) 124709(1)-(10).

[228] A. Cossaro, D. Cvetko, G. Bavdek, L. Floreano, R. Gotter, A. Morgante, F. Evangelista, and A. Ruocco, J. Phys. Chem. B 108, (2004) 14671-14676.

[229] H. Peisert, A. Peterhans, and T. Chassé, J. Phys. Chem. C 112, (2008) 5703-5706.

[230] B. P. Tonner, C. M. Kao, E. W. Plummer, T. C. Caves, R. P. Mesmer, and W. R. Salaneck, Phys. Rev. Lett. 51, (1983) 1378-1381.

[231] C. J. Nelin, P. S. Bagus, J. Behm, and C. R. Brundle, Chem. Phys. Lett. 105, (1984) 8-63.

[232] S. G. Kukolich, J. Am. Chem. Soc. 104, (1982) 4715-4716.

[233] N. Taguchi, Y. Mochizuki, T. Ishikawa, K. Tanaka, Chem. Phys. Lett. 451, (2008) 31-36.